Quantum Correlations and Temperature Fluctuations in Nanoscale Systems

Brange, Fredrik

2019

Document Version:
Publisher's PDF, also known as Version of record

Quantum Correlations and Temperature Fluctuations in Nanoscale Systems

FREDRIK BRANGE
FACULTY OF SCIENCE | LUND UNIVERSITY

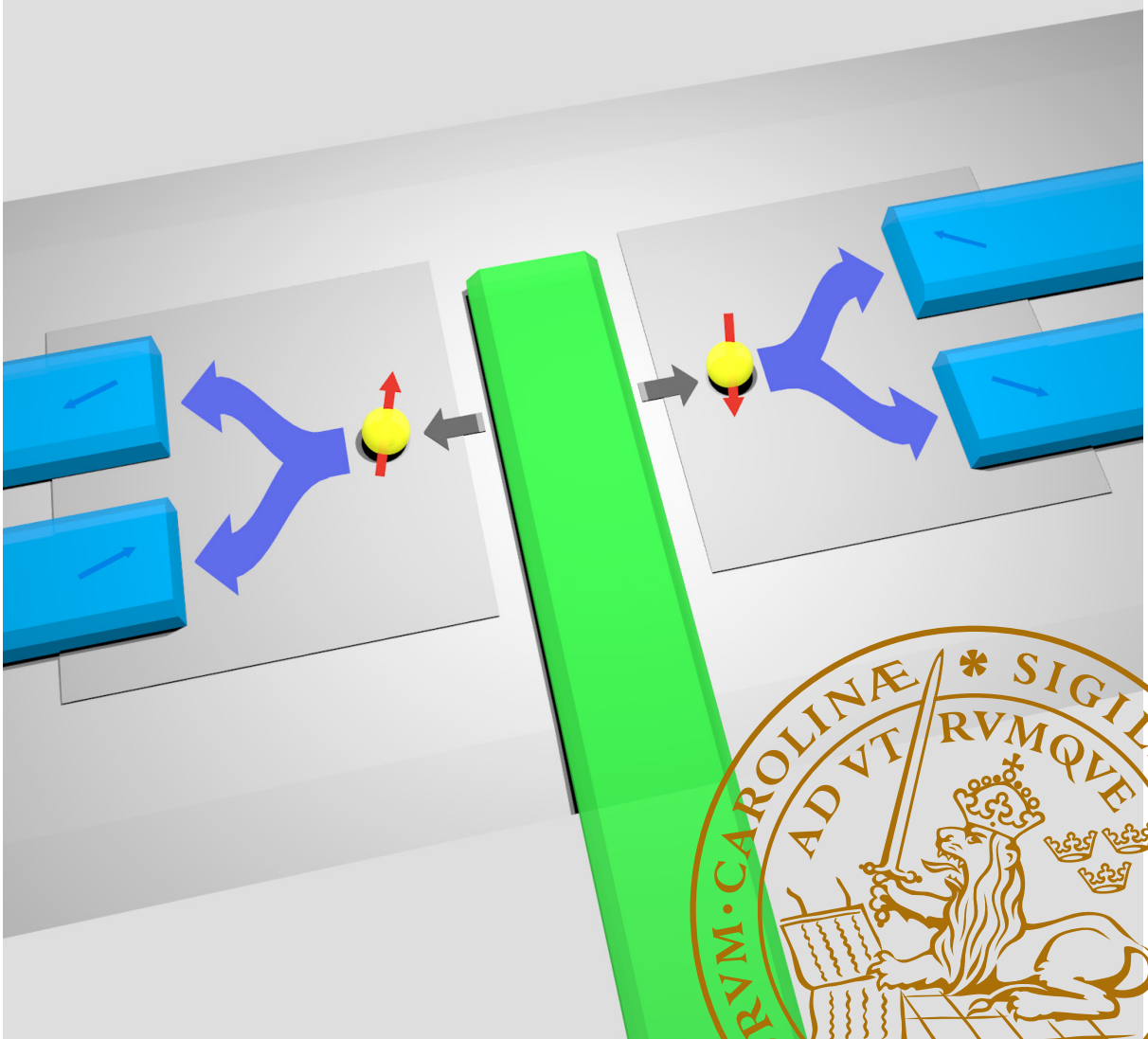

Quantum Correlations and Temperature Fluctuations in Nanoscale Systems

Quantum Correlations and Temperature Fluctuations in Nanoscale Systems

by Fredrik Brange

LUND
UNIVERSITY

Thesis for the degree of Doctor of Philosophy in Engineering
Thesis advisors: Assoc. Prof. Peter Samuelsson, Prof. Andreas Wacker
Faculty opponent: Prof. Henning Schomerus

To be presented, with the permission of the Faculty of Science of Lund University, for public criticism in the Rydberg lecture hall (Rydbergsalen) at the Department of Physics on Friday, the 26th of April 2019 at 09:00.

Organization
LUND UNIVERSITY
Department of Physics
Box 118
SE–221 00 LUND
Sweden

Document name
DOCTORAL DISSERTATION

Date of disputation
2019-04-26

Sponsoring organization

Author(s)
Fredrik Brange

Title and subtitle
Quantum Correlations and Temperature Fluctuations in Nanoscale Systems

Abstract
This thesis addresses two different topics related to the physics of nanoscale systems. The first topic concerns quantum correlations and entanglement between electrons in solid-state systems, with a focus on how to generate electronic orbital entanglement on a sub-decoherence time scale and how to achieve experimentally more feasible entanglement detection schemes. The second topic concerns heat transport and temperature fluctuations in nanoscale systems, with a focus on how to utilize temperature fluctuations for calorimetric detection of single particles. The thesis comprises five papers.

In Paper I, we propose a quantum dot system to generate and detect, using cotunneling processes, orbitally entangled pairs of electrons on a sub-decoherence time scale.

In Paper II, we investigate, by applying an entanglement witness, the minimal number of zero-frequency current cross-correlation measurements needed to detect bipartite entanglement between two flying qubits.

In Paper III, we consider energy and temperature fluctuations, and the influence of charging effects, in a metallic island tunnel coupled to a normal metallic lead, the so-called single electron box.

In Paper IV, we investigate nanoscale quantum calorimetry and propose a setup consisting of a metallic island and a superconducting lead to realize a nanoscale calorimeter that may probe the energies of tunneling electrons.

In Paper V, we investigate photon transport statistics of a microwave cavity, including the short-time statistics of single photon emissions and the long-time statistics of heat transport through the cavity.

Key words
Quantum transport, electronic entanglement, nanoscale thermodynamics, quantum calorimetry

Classification system and/or index terms (if any)

Supplementary bibliographical information

Language
English

ISSN and key title

ISBN
978-91-7895-046-1 (print)
978-91-7895-047-8 (pdf)

Recipient's notes

Number of pages
183

Price

Security classification

Quantum Correlations and Temperature Fluctuations in Nanoscale Systems

by Fredrik Brange

LUND
UNIVERSITY

A doctoral thesis at a university in Sweden takes either the form of a single, cohesive research study (monograph) or a summary of research papers (compilation thesis), which the doctoral student has written alone or together with one or several other author(s).

In the latter case the thesis consists of two parts. An introductory text puts the research work into context and summarizes the main points of the papers. Then, the research publications themselves are reproduced, together with a description of the individual contributions of the authors. The research papers may either have been already published or are manuscripts at various stages (in press, submitted, or in draft).

Cover illustration front: An illustration of a generic entangler–detector system for generating and detecting entangled electrons in nanoscale systems.

Funding information: The thesis work was financially supported by the Swedish Research Council.

Faculty of Science, Department of Physics

ISBN: 978-91-7895-046-1 (print)
ISBN: 978-91-7895-047-8 (pdf)

Printed in Sweden by Media-Tryck, Lund University, Lund 2019

Contents

List of publications and contributions of the author

This thesis is based on the following publications, referred to by their Roman numerals:

I **Subdecoherence Time Generation and Detection of Orbital Entanglement in Quantum Dots**
F. Brange, O. Malkoc, and P. Samuelsson
Phys. Rev. Lett. **114**, 176803 (2015)

We propose a setup consisting of six quantum dots to generate and detect orbitally entangled pairs of electrons. The entanglement is generated via two-particle interference of cotunneling electrons. The cotunneling processes take place on a time scale much shorter than the decoherence time, making the scheme insensitive to charge noise. We show that the entanglement may be detected with a Bell test based on either low-frequency current cross-correlation measurements or real-time detection of single electrons.

Contribution: I did all the calculations and drew all the figures. I also wrote the first draft of the manuscript in collaboration with the co-authors and contributed to its final writing.

II **Minimal Entanglement Witness from Electrical Current Correlations**
F. Brange, O. Malkoc, and P. Samuelsson
Phys. Rev. Lett. **118**, 036804 (2017)

We investigate the minimal number of low-frequency current cross-correlation measurements needed to witness entanglement between two flying qubits. We show that entanglement may be detected using only two cross-correlation measurements, for any finite detector efficiencies and noncollinear polarization vectors. Quite surprisingly, we find that any entangled pure state may be detected with only two measurements, except the maximally entangled, which require three. We present the symmetric detector settings that optimize the entanglement detection margin with respect to the separable states.

Contribution: I developed the idea of using symmetries and eigenvalues to formulate the witness conditions in a simple way. I also did most of the calculations, including the optimization of the detector settings, and drew all the figures. I wrote the first draft of the manuscript and contributed to its final writing.

III **Energy and temperature fluctuations in the single electron box**
T. L. van den Berg, F. Brange, and P. Samuelsson
New J. Phys. **17**, 075012 (2015)

We investigate energy and temperature fluctuations in the single electron box. For small systems, such as the single electron box, fluctuations may play an important role, even in equilibrium. Electrons tunneling in or out of the box cause the energy of the box as well as its effective temperature to fluctuate. We analyze these induced fluctuations in terms of full counting statistics. In particular, we use stochastic path integrals to extract the temperature statistics from the heat transfer statistics.

Contribution: I participated in the formulation of the stochastic path integral approach, and did many of the calculations on the energy and temperature statistics. I drew Figs. 2 and 3, and contributed to the final writing of the manuscript.

IV **Nanoscale quantum calorimetry with electronic temperature fluctuations**
F. Brange, P. Samuelsson, B. Karimi, and J. P. Pekola
Phys. Rev. B **98**, 205414 (2018)

We propose a setup for nanoscale quantum calorimetry based on electronic temperature fluctuations. A tunnel-coupled superconductor injects electrons into an absorber consisting of a rapidly thermalizing electron gas, with a well-defined effective temperature. Monitoring the fluctuations of this effective temperature, the energies of the injected electrons may be inferred. In particular, we investigate under what conditions single-particle calorimetry is attainable.

Contribution: I did most of the calculations and drew all the figures. I also wrote the first draft of the manuscript and contributed to its final writing.

V **Photon counting statistics of a microwave cavity**
F. Brange, P. Menczel, and C. Flindt
Phys. Rev. B **99**, 085418 (2019)

We investigate the photon statistics of a microwave cavity weakly coupled to one or several heat baths. We derive the moment generating function of the photon statistics for both short and long times. From this, we obtain the waiting time distribution, the correlation functions and the factorial cumulants of photon emissions. We also investigate the long-time statistics of heat currents flowing through a cavity coupled to two heat baths with different temperatures.

Contribution: I calculated the waiting time distributions, the correlation functions and the long-time statistics. I drew all the figures. I wrote most of the first draft of the manuscript and contributed to its final writing.

Acknowledgements

This thesis would not have been possible without the help and support of a number of people to whom I am indebted.

First of all, I want to thank my supervisor, Peter Samuelsson. I am very thankful for having got the opportunity to do a PhD in your research group. In particular, I want to thank you for giving me such a freedom in choosing what research projects I could work with. It has been very exciting and stimulating to work together with you, and I have learnt a lot about both physics and how to conduct research during these five years. Thank you.

I want to thank all of the people that I have been collaborating with during my time as a PhD student in Lund. It has been a great pleasure to work together with Ognjen Malkoc, Tineke van den Berg, Sara Kheradsoud, Patrick Potts, Timo Kerremans and Bahareh Goldozian. I have really enjoyed the many interesting discussions at seminars and group meetings. I would also like to say a big thank you to my office mates over the years, David Winge, Martin Franckié, Martin Albertsson, Alex Kalaee, Betül Atalay and Mattias Bertolino. I have very much enjoyed your company and our interesting discussions about everything between heaven and earth, sometimes even physics... I also want to thank Josef Josefi, Gunnar Eriksson, Jakob Bengtsson and all the other PhD students and postdocs at the Division of Mathematical Physics. A special thanks to Katarina Lindqvist, Cecilia Jarlskog, Gunnar Ohlén and Sven Åberg for all our interesting (and often quite political) discussions in the lunch room. Without you, working at the Division of Mathematical Physics would not have been the same. I want to especially thank you, Katarina, for all the help with practical and administrative matters during my PhD.

I am very grateful to my collaborators at Aalto University, Christian Flindt and Paul Menczel as well as Jukka Pekola and Bayan Karimi. I have really enjoyed collaborating with all of you! I am particularly thankful to you, Christian, for giving me the opportunity to spend three months in your research group during my PhD. For me the stay was very interesting, exciting and fruitful, and I am looking forward to continuing our collaboration in the future. I also want to thank the other people that I met during my time at Aalto, including Elina Potanina, Aydın Deger and Pablo Burset, for making my stay at Aalto so enjoyable.

Last, but not least, I want to acknowledge my family, in particular my parents, for always supporting and encouraging me throughout my whole life. Without you, I would not have been where I am today. And most importantly, I want to thank you, Thomas, for your endless love and support. Your constant advice and words of encouragement helped me to endure the struggles of writing this thesis. Thank you.

Popular summary in English

Over the last century, mankind has experienced an unparalleled technological revolution. This revolution has been particularly noticable in the fields of electronics and information technology, where we today take computers, mobile phones, the internet and other telecommunications for granted in our daily lives. Much of the technological development has been made possible thanks to basic research in the fields of physics and electronics during the 19th and 20th centuries, which has given us an increased understanding of fundamental phenomena such as electromagnetism as well as new inventions, such as the transistor. But as much as basic research has paved the way for new technology, the technological evolution has also paved the way for new research possibilities. Thanks to new technology, it is today possible to control and manipulate components on increasingly smaller length scales in a way that yesterday's physicists could only dream of. This allows us to explore completely new regimes with exciting, novel physics in so-called nanoscale systems, small components where the dimensions may be as small as a millionth of a millimeter.

The physics of nanoscale systems differs significantly from our daily, macroscopic world. Single particles, such as electrons and photons, typically play a crucial role for the functionality of these systems, whether it is a nanoscale transistor or a nanoscale engine. New phenomena arise that we normally do not observe in our daily lives. This includes, among other things, so-called quantum effects and the increasing importance of fluctuations and surface physics as the dimensions are scaled down. In this thesis, we treat two particular phenomena which are both present in nanosystems: quantum correlations and temperature fluctuations.

Quantum correlations are correlations that arise between particles which are quantum entangled, i.e., their states (e.g., position, momentum or spin) cannot be described independently of each other, despite full knowledge about the system as a whole. The prime example of an entangled state is the singlet state of two spins. In that case, the total spin is zero, i.e., the spins must be pointing in opposite directions. However, which spin is pointing in which direction is undefined; they are both in a quantum mechanical superposition between up and down along any arbitrary measurement axis, at least until a measurement is performed.

The presence of quantum correlations between entangled particles in quantum physics was first highlighted in the mid-1930s. Their actual existence was first questioned since they violate a fundamental physical principle called local realism in classical physics. But during the second half of the 20th century, experiments confirmed their existence and with the advent of quantum information theory during the 1980s, quantum correlations and quantum entanglement came to emerge as indispensable resources for quantum computers. Quantum computers are computers taking advantage of quantum effects to perform more

efficient algorithms than classical computers. Many algorithms which are meant to be used in quantum computers are based on the access to quantum entangled particles which display quantum correlations. It is therefore a neccessity to be able to generate and detect quantum entanglement to build quantum computers.

In principle any particles may be entangled. The main problem, though, is that entanglement is a very fragile resource, that is easily lost as the entangled particles interact with other particles in their surrounding, a process called decoherence. Electrons, which would be the natural choice given their role in conventional electronics, are unfortunately particularly exposed to decoherence. The main reason is that they are charged, making them interact strongly with their environment. In this thesis, we propose a way of generating and detecting electrons on a time scale much shorter than the time scale on which the interaction with the environment destroys the entanglement. The idea is to use so-called cotunneling processes to both generate and detect the entanglement between pairs of electrons. These processes take place on the picosecond time scale, much shorter than the nanosecond time scale on which the decoherence destroys the entanglement. We also investigate how the detection of entanglement can be made simpler in nanoscale systems. Conventional methods require many complicated measurements, but it turns out that by using so-called entanglement witnesses it is actually possible to detect entanglement with much fewer measurements.

The second topic treated in this thesis concerns temperature fluctuations. Fluctuations, i.e., deviations from the mean value of a certain quantity, become more and more important as the system size of a physical system decreases. In small systems, such as nanoscale systems, it is therefore crucial to take into account the noise in, for instance, temperature and heat to describe the physics correctly. Quantum thermodynamics is the field of physics describing heat transport in small, quantum mechanical systems where those fluctuations play an important role. There are many promising applications within this field, such as heat engines which may generate electricity out of heat with high efficiencies.

In this thesis, we specifically consider the possibilities of utilizing temperature fluctuations to detect single particles, such as photons or electrons, in nanoscale systems. By coupling a superconductor to a small piece of metal, we may detect electrons that are transferred between the superconductor and the metal piece using the temperature fluctuations induced in the metal. This method, called quantum calorimetry, would, hopefully, in the future facilitate new investigations of quantum thermodynamical phenomena in nanoscale systems. A concrete example of such a phenomenon is emissions of photons from a microwave cavity, which is discussed in the fifth paper of this thesis.

Overall this thesis aims at contributing to an increasing understanding for quantum correlations and temperature fluctuations in nanoscale systems.

Populärvetenskaplig sammanfattning på svenska

Det senaste århundradet har mänskligheten upplevt en teknologisk revolution som saknar motstycke i historien. Denna utveckling har varit särskilt tydlig på elektronik- och informationsteknik-området, där vi idag tar datorer, mobiler, internet och annan telekommunikation för givet i våra dagliga liv. Mycket av den tekniska utvecklingen har möjliggjorts tack vare grundforskning på fysik- och elektronikområdet under 1800- och 1900-talet, vilket har gett oss bland annat ökad förståelse för grundläggande fenomen såsom elektromagnetism och uppfinningar som till exempel transistorn. Men lika mycket som grundforskning har banat vägen för ny teknologi, har den teknologiska utvecklingen också banat vägen för ny grundforskning. Tack vare ny teknik är det idag möjligt att kontrollera och manipulera komponenter på allt mindre längdskalor på ett sätt som gårdagens fysiker bara kunde drömma om. Detta tillåter oss att utforska helt nya fysikaliska regimer med ny spännande fysik i så kallade nanosystem, som består av komponenter där dimensionerna kan vara så små som en miljondels av en millimeter.

Fysiken i nanosystem skiljer sig markant från vår vardagliga, makroskopiska värld. Enskilda partiklar, såsom elektroner och fotoner, spelar typiskt sett en avgörande roll för funktionaliteten hos nanosystem, oavsett om det handlar om en transistor eller en liten motor på nanoskala. Nya fenomen uppkommer också som vi normalt inte märker av i vår vardagliga värld. Det handlar bland annat om så kallade kvanteffekter och den ökade betydelsen av fluktuationer och ytfysik i takt med att dimensionerna skalas ner. I den här avhandlingen behandlar vi särskilt två fenomen som båda är förekommande i nanosystem: kvantkorrelationer och temperaturfluktuationer.

Kvantkorrelationer är korrelationer som uppkommer mellan partiklar som är kvantsammanflätade, vilket innebär att deras tillstånd (t.ex. position, rörelsemängd eller spinn) inte kan beskrivas oberoende av varandra, trots full kunskap om systemet i sin helhet. Ett typexempel på ett sammanflätat tillstånd är singlett-tillståndet för två spinn. Det totala spinnet är i det fallet noll, vilket innebär att spinnen måste vara motriktade. Exakt vilket spinn som pekar åt vilket håll är däremot inte väldefinierat; de befinner sig båda i en kvantmekanisk superposition mellan de två möjliga riktningarna längs med en godtycklig mätaxel, åtminstone tills en mätning utförs.

Förekomsten av kvantkorrelationer mellan sammanflätade partiklar inom kvantfysiken uppmärksammades för första gången i mitten av 1930-talet. Deras faktiska existens ifrågasattes eftersom de bryter mot en grundläggande fysikalisk princip som inom klassisk fysik kallas lokal realism. Men under 1900-talets senare del påvisades deras existens genom experiment och sedan uppkomsten av kvantinformationsområdet på 1980-talet har kvantkorrelationer och kvantsammanflätning kommit att utvecklas till en oumbärlig resurs för kvantdatorer. Kvantdatorer är datorer som drar nytta av kvanteffekter för att kunna utföra mer effektiva

algoritmer än klassiska datorer. Många algoritmer som är tänkta att köras på kvantdatorer bygger på tillgången av just kvantsammanflätade partiklar som kan uppvisa kvantkorrelationer. Det är därför helt avgörande att kunna generera och detektera kvantsammanflätning för att kunna bygga fungerande kvantdatorer.

I princip kan vilka partiklar som helst sammanflätas. Huvudproblemet är dock att kvantsammanflätning är en mycket skör resurs, som lätt förloras om de sammanflätade partiklarna interagerar med andra partiklar i sin omgivning, en process som kallas för dekoherens. Elektroner, som vore det naturliga valet att använda med tanke på deras roll i konventionell elektronik, är dessvärre särskilt utsatta för dekoherens. Detta beror främst på deras laddning, som gör att de interagerar starkt med sin omgivning. I den här avhandlingen föreslår vi ett sätt att generera och detektera sammanflätade elektroner på en tidsskala mycket kortare än den tidsskala på vilken omgivningen förstör sammanflätningen. Idén är att använda så kallade kotunnlingsprocesser för att både generera och detektera sammanflätning mellan par av elektroner. Eftersom dessa processer äger rum på pikosekundskalan så är de tillräckligt snabba för att inte utsättas för dekoherens från omgivningen. I avhandlingen undersöker vi även hur man kan underlätta detektionen av sammanflätning i kvantsystem. Konventionella metoder kräver många komplicerade mätningar, men det visar sig att genom att använda sig av så kallade sammanflätningsvittnen kan man detektera sammanflätning med betydligt färre mätningar.

Det andra ämnet som behandlas i den här avhandlingen rör temperaturfluktuationer. Fluktuationer, det vill säga avvikelser från medelvärdet för en viss storhet, får i allmänhet en större och större betydelse ju mindre ett system är. I små system, såsom nanosystem, måste man därför ta hänsyn till brus i till exempel temperatur och värme för att erhålla en korrekt fysikalisk beskrivning. Kvanttermodynamik är det område inom fysiken som beskriver värmetransport i små, kvantmekaniska system där just fluktuationer spelar en viktig roll. Det finns många lovande tillämpningar inom detta område, exempelvis nya värmemotorer som kan alstra el från värme med en hög verkningsgrad.

I den här avhandlingen tittar vi särskilt på möjligheterna att använda temperaturfluktuationer till att detektera enstaka partiklar, till exempel fotoner eller elektroner, i nanosystem. Genom att koppla en supraledare till en liten metallbit, kan vi detektera elektroner som överförs mellan supraledaren och metallbiten med hjälp av de temperaturfluktuationer som uppkommer i metallbiten. Denna metod, som kallas kvantkalorimetri, banar också vägen för att studera andra kvanttermodynamiska fenomen. Exempelvis undersöker vi emissionen av fotoner från en mikrovågskavitet i det femte pappret i avhandlingen.

Allt som allt syftar denna avhandling till att bidra med ökad förståelse och ökade kunskaper om kvantkorrelationer och temperaturfluktuationer i nanosystem.

Part I

Background and Theory

Chapter 1

Introduction

This thesis takes its starting point in nanoscale systems, objects with at least one dimension in the nanometer range ($1 - 100$ nm) [1]. Being somewhere on the borderland between the macroscopic world and the domain of single atoms, these systems may display physical phenomena that are drastically different from the ones we are used to in our daily lives. The perhaps most astonishing ones are quantum effects, non-classical features originating from the wave properties of single particles, e.g., electrons and photons. Other key phenomena include the increasing importance of fluctuations and surface effects as physical dimensions are scaled down.

Besides fundamental aspects, the prospects of utilizing nanoscale phenomena for novel applications, such as quantum computers [2] or quantum heat engines [3], have stimulated a tremendous amount of research in the field of nanophysics over the last few decades, including the work of this thesis. Here we address two topics both related to nanoscale transport of either particles or heat. The first topic concerns quantum entanglement and quantum correlations, or more specifically, how to generate, separate and detect entangled electrons in solid-state systems. The second topic concerns quantum thermodynamics and temperature fluctuations, in particular single-particle heat transport and how to utilize temperature fluctuations for nanoscale quantum calorimetry.

Common for all the systems considered in this thesis is that they are weakly coupled to their environment (consisting of one or several reservoirs). This allows us to employ a formalism based on density matrices and master equations, important concepts of this thesis which are to be introduced in Ch. 2. Master equations may incorporate both quantum effects, such as coherences, and interactions with the environment, such as decoherence and relaxation.

Below we give a brief overview of the two main topics of this thesis; a more extensive introduction is found in the following chapters.

1.1 Quantum entanglement and quantum correlations

The first topic of this thesis deals with entanglement and quantum correlations. Entanglement is a phenomenon that arises when two or more particles are correlated in such a way that their individual quantum states cannot be described independently. Displaying so-called quantum correlations that classical physics cannot account for, entanglement was originally highlighted in 1935 for its violation of the classical notion of local realism [4, 5]. Einstein, Podolsky and Rosen questioned [4] whether entanglement was a real physical effect, sparking a decades-long debate on the matter only to be settled by Bell [5] in the 1960s. By contrast, Schrödinger described it as not just one – but *the* – characteristic trait of quantum mechanics [6]. Even so, it was not until the 1980s and 1990s, with the advent of quantum information theory, that the real power of entanglement was fully understood. Entanglement then came to emerge as an indispensable resource for many quantum information and quantum computing applications [2]. For instance, several quantum information protocols, such as superdense coding [7], quantum teleportation [8] and quantum cryptography [9], were developed entirely relying on the properties of entangled states. Furthermore, it was realized that entanglement allows for any quantum gate to be implemented using only single qubit gates [10]. In other words, entanglement is today considered as not only a peculiar quantum phenomenon, but an indispensable resource for quantum information processing. It is thus highly desirable to be able to generate, manipulate and detect entangled states in a controllable way.

Despite an enormous amount of research over the last decades, the development of quantum computing is yet in its infancy. In particular, there is still no concensus about what degree(s) of freedom to use for encoding quantum information in quantum computers. Polarized entangled photons have been widely used in quantum optics to demonstrate various quantum information protocols [2]. They are easy to separate coherently over long distances, making them particularly suitable for quantum communication [11, 12]. However, they are difficult to entangle and do not provide scalable qubits. For quantum computing, other kinds of degrees of freedom have therefore been developed or proposed, including ion traps [13], superconducting qubits [14] and topological qubits [15]. A single electron is in many regards the ultimate qubit due to its smallness and the prospects of scalability and compatibility with conventional electronics. Today's electronics already provides good ways of controlling, manipulating and detecting electrons [2]. The electronic degree of freedom includes both the spin degree of freedom [16, 17] – a natural two-level system – and orbital degrees of freedom [18, 19], for instance charge states in quantum dots [20–23] and edge channels [24–26] in quantum Hall systems.

Unfortunately, electronic entanglement is impaired by its own challenges and in this thesis we will address two of them. The first one is the strong interactions with the environment that lead to short decoherence times, swiftly killing any entanglement. This is a particularly

pronounced effect for orbitally entangled electrons, whose decoherence times, due to severe susceptibility to environment-induced charge noise, are typically of the order of merely a few nanoseconds [27–30]. This difficulty may, however, be coped with if the entanglement can be generated and detected on an even shorter time scale; in Paper I we propose such a setup utilizing cotunneling electrons in quantum dots on the picosecond time scale.

The second main challenge addressed in this thesis is related to the detection of electronic entanglement. Entanglement detection is highly challenging as it is difficult, in a solid-state environment, to read out the state of single electrons along an arbitrary measurement axis, especially for spin entanglement. Using so-called entanglement witnesses [31–34], we show in Paper II that the number of measurements required for solid-state entanglement detection may be substantially reduced compared to conventional methods, paving the way for experimentally more feasible entanglement detection schemes for solid-state systems. The theory underpinning Papers I and II is further discussed in Ch. 3.

1.2 Quantum thermodynamics and temperature fluctuations

The second topic of this thesis deals with quantum thermodynamics. More specifically, we consider heat transport and temperature fluctuations in nanoscale systems.

Classical thermodynamics is the field of physics dealing with heat and other forms of energy in typically large, macroscopic close-to-equilibrium systems, where fluctuations and quantum effects do not play an important role [35]. Its underlying, often astonishingly simple, statistical arguments, make it a surprisingly universal and elegant theory, describing everything from everyday-life applications like engines and refrigerators to fundamental phenomena like black-body radiation and thermal states. One of the most fascinating and famous thermodynamical principles is the second law; that the entropy – the disorder – of an isolated system can never decrease over time.

However, when system dimensions are scaled down, fluctuations and quantum effects become increasingly important. For instance, although rare, single microscopic processes may, by chance, give rise to a decrease in the entropy; the second law as defined above only holds on average. The need to fully account for the effect of fluctuations, and also of quantum phenomena, has spurred the development of stochastic and quantum thermodynamics. At first sight, it might not be intuitive that it is possible to apply statistical arguments, as used for the macroscopic systems in classical thermodynamics, on systems containing only one or a few particles. However, as illustrated by, e.g., the Jarzynski equality [36, 37] and the Crooks fluctuation theorem [38], small, microscopic systems may be described statistically if one considers all the individual trajectories that a system may evolve along over time. One may then consider the probabilities for a small system to dissipate a

certain amount of heat or to perform a certain amount of work, leading to various kinds of fluctuation relations, that are valid even arbitrarily far away from equilibrium. These relations relate the probabilities of, e.g., extracting or performing certain amounts of work to the associated entropy production.

In this thesis, we consider heat transport in a small metallic island coupled to an environment, consisting of one or several leads. Such an island may be fabricated using, e.g., electron beam lithography and evaporation techniques [39]. The island may be large enough to prevent quanization effects, but small enough to have its temperature sensitive to the absorption (or emission) of individual particles, such as photons or electrons. Importantly, the temperature is only well-defined if the island has a very short internal thermalization time, so that the electrons may be described by a Fermi–Dirac distribution at any instant of time. This is typically the case in real experiments [40]. In Paper III, we consider how electrons tunneling between a metallic island and a lead give rise to temperature fluctuations in such an island, even in equilibrium. A build-up of fluctuations is possible at low temperatures where the heat exchange with the environment, in this case phonons, can be made much slower than the time scale on which electrons tunnel in and out of the island. In particular, we investigate the influence of charging effects on both the heat transport and the temperature fluctuations. Thanks to recent advances in fast and ultrasensitive thermometry [41–43], it is possible to investigate not only the average temperature but also the noise of the temperature fluctuations. The temperature read-out is typically based on very sensitive measurements of temperature-dependent currents flowing through the system.

The advances in nanoscale thermometry has in turn spurred the interest for nanoscale quantum calorimetry. Quantum calorimetry is a method for inferring the energy of a single particle from a measurement on the temperature change it causes when depositing its energy in an absorber [44], such as a metallic island. In Paper IV, we investigate nanoscale quantum calorimetry based on a metallic island coupled to a superconducting injector of tunneling electrons. We show that our setup works as a versatile calorimeter, where the rate and the energies of the injected electrons may be controlled externally with a voltage source. Besides allowing for the detection of single electrons, the long-term goal is to facilitate the development of better single microwave photon detectors. That would pave the way for new experiments on, e.g., single photon emissions from a microwave cavity, as addressed in Paper V. There we investigate a cavity coupled to one or several heat baths – a conceptually simple system that is surprisingly rich in physics. It allows us to study both the statistics of photon emissions and of heat transport. The main findings of Papers III–V and the underlying theory are all further discussed in Ch. 4.

1.3 Scope of this thesis

The outline of the thesis is as follows. In the first part we give an introduction to the field, starting with quantum transport (Ch. 2) and then proceeding to entanglement (Ch. 3) and quantum thermodynamics (Ch. 4). The purpose of Ch. 2 is to introduce basic transport theory, including master equations, full counting statistics and waiting time distributions. We exemplify these concepts using a single resonance level, bosonic or fermionic, coupled to a reservoir. The bosonic version is identical to the microwave cavity in Paper V, and many of the examples thus summarize the key findings of Paper V.

In Ch. 3, we continue by introducing entanglement, briefly explaining the historical background that led to its discovery, and, most importantly, describing how entangled electrons may be generated and detected in nanoscale systems. We present the main findings of Papers I and II. In Ch. 4, we address quantum thermodynamics and temperature fluctuations, and present the theory and main findings of Papers III and IV, as well as parts of Paper V. Finally, in Ch. 5 we give a conclusion and outlook to the whole thesis.

In the second part of the thesis, the research papers are found in their entirety. The first two papers are related to the first main topic of the thesis and the other three to the second main topic. As a complement to the first part of the thesis, we also provide two appendices in the third part of the thesis that contain technical derivations of some of the equations of the theoretical background.

Chapter 2

Quantum transport

Quantum transport is the field of quantum physics dealing with transport in nanoscale systems [45]. It provides the theory for describing and investigating the physical phenomena considered in this thesis. Here, in this chapter, we will outline some of the most important concepts used in the remainder of the thesis.

Transport theory, whether it is quantum or classical, is inherently a theory of open systems [1], where particles, heat or other physical quantities may be exchanged with an environment. The aim of such a theory is to describe how this exchange depends on various physical properties, such as the internal structure of the system or its coupling to the environment, and how it responds to perturbations, such as temperature gradients or voltage biases. For large, macroscopic systems, it is normally sufficient to only describe the average currents to obtain a complete picture of the transport physics, as any relative deviations are negligible [35]. By contrast, for small systems, such as nanoscale systems, fluctuations may play a crucial role. In fact, in many cases the noise – the typical magnitude of the fluctuations – *is* the actual signal of interest in nanoscale systems [46]; we will see several examples of this in the following chapters. To properly describe transport in nanoscale systems, quantum transport theory must thus provide a statistical description that fully accounts for fluctuations.

The aim of this chapter is to introduce such a statistical description. To this end, we proceed in three steps. First, we define the concepts of pure and mixed states. The latter is vital to describe open quantum systems as statistical ensembles of pure quantum states. These definitions are also of great importance for the subsequent discussion on entanglement in Ch. 3. Second, we consider the time evolution of open quantum systems weakly coupled to an environment (Sec. 2.2). More specifically, we introduce the Lindblad equation and investigate some of its fundamental properties. Third and most importantly, we discuss

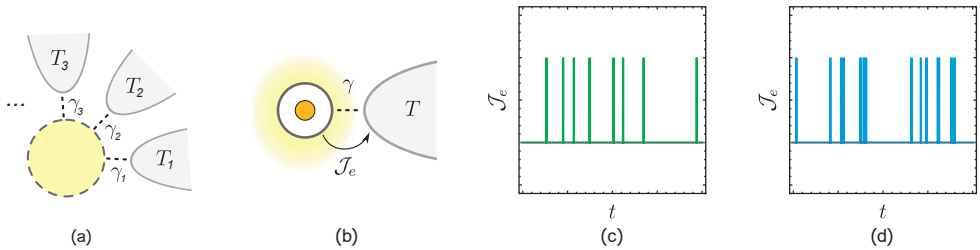

Figure 2.1: (a) A generic nanoscale system (yellow) coupled to a number of terminals (gray, here three) via coupling strengths γ_1, γ_2 and γ_3, respectively. The terminals consist of particle reservoirs with well-defined temperatures T_1, T_2 and T_3 and chemical potentials μ_1, μ_2 and μ_3. The aim of quantum transport is to characterize the transfer of particles, heat o other physical quantities through the system. (b) A single resonance level (fermionic or bosonic) coupled, with a coupling strength γ, to a reservoir, with temperature T and mean occupation number $\bar{n} = (\exp[\varepsilon/(k_B T)] \pm 1)^{-1}$, with $+$ $(-)$ for fermions (bosons) and ε the resonance energy. This system is used as an example system throughout the thesis to illustrate various concepts. Typical examples of Monte Carlo-simulated time traces of the particle emission statistics for (c) fermionic particles and (d) bosonic particles for $\bar{n} = 0.5$. Every particle emission event is indicated by a spike.

a number of different concepts to characterize transport statistics, and show how these may be extracted from the Lindblad equation (Sec. 2.3). In particular, we consider full counting statistics in the long-time limit, where zero-frequency noise measurements form an indispensable tool for investigating both quantum correlations (Ch. 3) and temperature fluctuations (Ch. 4) in nanoscale systems. Such measurements constitute an integral part of all five papers of this thesis.

We will throughout the chapter consider a generic nanoscale system [see Fig. 2.1 (a)] coupled to one or several reservoirs. While the overall goal is to introduce tools to describe the emission, absorption or net currents of particles or heat flowing between the system and one or several of the reservoirs, the main focus will be on particle emission. Most concepts and results may easily be generalized to other transport quantities. To provide as simple and concrete examples as possible of various concepts, we will consider particle emissions from an example system consisting of a single non-degenerate resonance level, either fermionic or bosonic, weakly coupled, with a rate γ, to a single reservoir [see Fig. 2.1 (b)–(d)]. In the fermionic case, this could be a quantum dot operating in the strong Coulomb blockade regime, while in the bosonic case it could be a microwave photon cavity, identical to the one in Paper V. Besides illustrating some of the key concepts of this chapter (and of Paper V), the example system also allows us to highlight some of the fundamental differences between bosonic and fermionic transport.

2.1 States and observables

A key concept, not only of transport theory, but also of classical physics, thermodynamics and quantum mechanics, is that of a *state* [47]. In a broad sense, a state aims at describing the physical *reality* of a system, i.e., the physical quantities which have predetermined and

well-defined values, whether we measure them or not. More precisely, the state of a system allows us, at least to some extent, to predict the outcome of measurements of certain physical quantities – *observables* – of that system. However, although they provide a complete description of the physical reality, quantum states are highly restricted compared to their classical analogs as they are, even in principle, incapable of predicting the outcome of every possible measurement with certainty. According to quantum mechanics, this is not a result of the theory being incomplete, but rather an inherent property of our world, in which it is impossible for all physical observables to form part of one and the same reality simultaneously [48].

The remainder of this section focuses on introducing two important kinds of states. The first kind of states, pure states, provides a complete quantum mechanical description of all the *microscopic* degrees of freedom of a physical system, and corresponds to a microstate in statistical physics [1]. However, as we will see, such states are typically insufficient to describe open quantum systems. This motivates us to introduce the second kind of states – mixed states. Analogous to macrostates in statistical physics [1], they describe a system statistically in terms of ensembles of pure states.

2.1.1 Pure states (microstates)

In the Schrödinger picture of quantum mechanics, pure states are represented by normalized time-dependent state vectors $|\Psi(t)\rangle$, with $\langle\Psi(t)|\Psi(t)\rangle = 1$, that belong to a Hilbert space [49]. Observables are represented by hermitian operators $\hat{A}$ acting on these states; for simplicity we here assume that they do not have any explicit time dependence. While a pure state supposedly provides a complete description of the reality of a quantum system, it may only predict with certainty the outcome a_Ψ of a single measurement if $|\Psi(t)\rangle$ is an eigenstate of $\hat{A}$ with $\hat{A}|\Psi(t)\rangle = a_\Psi|\Psi(t)\rangle$. For any other state, for which we say that $\hat{A}$ lacks *reality*, the measurement outcomes fluctuate and quantum mechanics only provides the average value of such measurements, the expectation value

$$\langle\hat{A}\rangle_t = \langle\Psi(t)|\hat{A}|\Psi(t)\rangle = \mathrm{tr}\{\hat{A}|\Psi(t)\rangle\langle\Psi(t)\}. \tag{2.1}$$

The magnitude of the fluctuations – the quantum uncertainties – is

$$\sigma_A(t) = \sqrt{\langle(\Delta\hat{A})^2\rangle_t} = \sqrt{\langle\hat{A}^2\rangle_t - \langle\hat{A}\rangle_t^2}, \qquad \Delta\hat{A} \equiv \hat{A} - \langle A\rangle_t. \tag{2.2}$$

Importantly, for so-called *incompatible* observables $\hat{A}$ and $\hat{B}$, for which $[\hat{A},\hat{B}] \equiv \hat{A}\hat{B} - \hat{B}\hat{A} \neq 0$, there are no common eigenstates; these observables thus always lack simultaneous reality. This is the essence of the Heisenberg uncertainty principle [49]

$$\sigma_A(t)\sigma_B(t) \geq \frac{1}{2}|\langle[\hat{A},\hat{B}]\rangle_t|, \tag{2.3}$$

which lies at the heart of quantum mechanics. The prime examples of incompatible observables are the momentum and position of a particle or the projection of a spin along different axes. The question whether the Heisenberg uncertainty principle is an inherent property of our physical reality or a result of quantum mechanics being an incomplete theory will be further discussed in Ch. 3.

By finding the largest set of compatible observables, a so-called complete set, one can construct an orthonormal basis of eigenstates $|\Phi_i\rangle$ that fully predict the outcomes of the largest possible set of measurements. Here Φ_i represents the whole set of the corresponding eigenvalues; these are known as *quantum numbers*. Any other state may be written as

$$|\Psi(t)\rangle = \sum_i c_i(t)|\Phi_i\rangle, \qquad c_i(t) = \langle\Phi_i|\Psi(t)\rangle, \tag{2.4}$$

where $p_i(t) = |c_i(t)|^2$ is the probability of obtaining the measurement outcome a_{Φ_i} when the observable $\hat{A}$ is measured, for which $\hat{A}|\Phi_i\rangle = a_{\Phi_i}|\Phi_i\rangle$.

Due to the indistinguishability of identical particles in quantum mechanics, a great deal of care has to be taken in many-particle systems. One way of doing this is to use the occupation number representation [50] with a basis consisting of the so-called Fock states

$$|\Phi_i\rangle = |n_1 n_2 ... n_m\rangle, \tag{2.5}$$

where only the number of particles n_i in every accessible single-particle state $|\phi_i\rangle$ is specified, i.e., no reference to the identities of single particles is being made. More formally, these many-particle states belong to a Fock space $\mathcal{F} = \bigoplus_{n=0}^{\infty} S_{\pm}\mathcal{H}^{\otimes n}$ that is a direct sum over all tensor powers of the single-particle Hilbert space $\mathcal{H}$ [50]. Here S_+ is the antisymmetrizing operator for fermions and S_- the symmetrizing operator for bosons.

To every single-particle state $|\phi_i\rangle$, we introduce creation operators $\hat{a}_i^\dagger$ and annihilation operators $\hat{a}_i$, which increase and decrease, respectively, the particle number in that state [49]

$$\hat{a}_i^\dagger|n_1...n_i...n_m\rangle = \sqrt{n_i+1}|n_1...n_i+1...n_m\rangle, \quad \hat{a}_i|n_1...n_i...n_m\rangle = \sqrt{n_i}|n_1...n_i-1...n_m\rangle. \tag{2.6}$$

We note that $\hat{n}_i \equiv \hat{a}_i^\dagger\hat{a}_i$ may be interpreted as number operators whose eigenvalues are n_i; these operators form the complete set of compatible eigenoperators of the Fock states. The symmetry properties of fermionic and bosonic states are naturally incorporated into the (anti-)commutation properties of the creation and annihilation operators

$$[\hat{a}_i, \hat{a}_j^\dagger]_\pm = \delta_{ij}, \quad [\hat{a}_i, \hat{a}_j]_\pm = [\hat{a}_i^\dagger, \hat{a}_j^\dagger]_\pm = 0, \tag{2.7}$$

where $[\hat{A}, \hat{B}]_\pm \equiv \hat{A}\hat{B} \pm \hat{B}\hat{A}$ denotes the anticommutator $(+)$ for fermions and the commutator $(-)$ for bosons. Furthermore, δ_{ij} denotes the Kronecker delta. Importantly, for fermions we obtain the *Pauli principle* [51]

$$\hat{a}_i^\dagger\hat{a}_i^\dagger = \hat{a}_i\hat{a}_i = 0. \tag{2.8}$$

For the fermionic version of our example system, this means that the resonance level can be occupied by at most one particle at a time. In that case, using the states $|0\rangle$ and $|1\rangle$ with zero and one particles as a basis, the creation and annihilation operators may be represented in terms of the hermitian Pauli matrices (with eigenvalues ± 1)

$$\hat{\sigma}_x = \begin{pmatrix} 0 & 1 \\ 1 & 0 \end{pmatrix}, \qquad \hat{\sigma}_y = \begin{pmatrix} 0 & -i \\ i & 0 \end{pmatrix}, \qquad \hat{\sigma}_z = \begin{pmatrix} 1 & 0 \\ 0 & -1 \end{pmatrix}, \tag{2.9}$$

as

$$\hat{a}^\dagger = \frac{1}{2}\left(\hat{\sigma}_x + i\hat{\sigma}_y\right) \equiv \hat{\sigma}_+, \qquad \text{and} \qquad \hat{a} = \frac{1}{2}\left(\hat{\sigma}_x - i\hat{\sigma}_y\right) \equiv \hat{\sigma}_-. \tag{2.10}$$

Most importantly, any other operator may be expressed in terms of the annihilation and creation operators. For example, the Hamiltonian, describing the energy of a system, may for our example system be expressed as (up to an arbitrary constant)

$$\hat{H} = \varepsilon \hat{a}^\dagger \hat{a} + \sum_i \varepsilon_i \hat{b}_i^\dagger \hat{b}_i + \sum_i \left(t_i \hat{a}^\dagger \hat{b}_i + t_i^* \hat{b}_i^\dagger \hat{a} \right), \tag{2.11}$$

where $\hat{a}$ acts on the single mode of the system (bosonic or fermionic), $\hat{b}_i$ acts on mode i in the reservoir and t_i is the tunneling amplitude from mode i in the reservoir to the single mode in the system. Here $\hat{H}_S = \varepsilon \hat{a}^\dagger \hat{a}$ is the Hamiltonian for the system, $\hat{H}_E = \sum_i \varepsilon_i \hat{b}_i^\dagger \hat{b}_i$ is the Hamiltonian of the environment and $\hat{H}_{\text{int}} = \sum_i \left(t_i \hat{a}^\dagger \hat{b}_i + t_i^* \hat{b}_i^\dagger \hat{a} \right)$ is the interaction Hamiltonian, to be used later. In the bosonic case, this Hamiltonian is exactly the same as the one used in Paper V to describe a microwave cavity. In the fermionic case, the Hamiltonian to some extent resembles the one in Paper I, however, in the latter case we have six different nearest-neighbour coupled quantum dots, each one also coupled to a reservoir, which produces a somewhat more complicated Hamiltonian, to be discussed in Ch. 3.

As we will see in the next section, the full Hamiltonian provides the time evolution of the system *and* its environment. However, since the environment may contain infinitely many degrees of freedom it is desirable to find an effective description of the dynamics of the system alone by integrating out the degrees of freedom belonging to the environment. This is one of the aims of the theory of open quantum systems.

2.1.2 Mixed states (macrostates)

When dealing with open quantum systems, the state vector description introduced above turns out to be insufficient. To see this, we first note, based on Eq. (2.1), that for any state vector there is a density matrix $\hat{\rho}(t) = |\Psi(t)\rangle\langle\Psi(t)|$ describing the same state by a projection operator. Now, supposing that $\hat{\rho}(t)$ describes a composite system, consisting of

an open system S and its environment E, we may also want to consider the density matrix $\hat{\rho}_S(t)$ of the open system S alone. To extract this density matrix we integrate out the degrees of freedom belonging to the environment, thus obtaining

$$\hat{\rho}_S(t) = \mathrm{tr}_E\{\hat{\rho}(t)\} = \sum_i \langle\varphi_i|\Psi(t)\rangle\langle\Psi(t)|\varphi_i\rangle, \tag{2.12}$$

where tr_E denotes the partial trace over the environmental degrees of freedom and $|\varphi_i\rangle$ is any orthonormal basis for the Hilbert space of the environment. Most importantly, $\hat{\rho}_S(t)$ cannot in general be expressed as a projection operator. We thus conclude that an open system may not always be described by a pure state.

Instead, we introduce a more general class of states, mixed states, consisting of a statistical mixture of pure states $|\Psi(t)\rangle$ with weights $q_i \geq 0$. They may be represented [2] by density matrices of the form

$$\hat{\rho}(t) = \sum_i q_i|\Psi_i(t)\rangle\langle\Psi_i(t)|, \qquad \sum_i q_i = 1. \tag{2.13}$$

A straightforward generalization of the expression in Eq. (2.1) yields the expectation values

$$\langle\hat{A}\rangle_t = \sum_i q_i\langle\Psi_i(t)|\hat{A}|\Psi_i(t)\rangle = \mathrm{tr}\{\hat{A}\hat{\rho}(t)\}. \tag{2.14}$$

For a certain basis, the diagonal elements of the density matrix are called *populations* as they describe the probabilities of finding the system in a certain basis state. The off-diagonal elements are called *coherences* and describe superpositions; these are particularly important for entangled states. Equation (2.13) brings two defining properties of density matrices: $\mathrm{tr}\{\hat{\rho}(t)\} = 1$ and $\hat{\rho}(t) \geq 0$ (i.e., $\hat{\rho}(t)$ is a positive operator). These conditions ensure that, in any basis, the populations are non-negative and sum up to 1.

A concrete and important example of a density matrix is that of a qubit [2]

$$\hat{\rho}(t) = \frac{1}{2}\left(\mathbf{I} + \zeta(t)\mathbf{a}(t)\cdot\boldsymbol{\sigma}\right), \tag{2.15}$$

where $\mathbf{I}$ is the identity operator, $\mathbf{a}(t)$ is a unit vector (which may change over time), $\boldsymbol{\sigma} = (\hat{\sigma}_x, \hat{\sigma}_y, \hat{\sigma}_z)$ is the Pauli vector and $0 \leq \zeta(t) \leq 1$ is a parameter determining the mixedness of the qubit state. We will see in Ch. 3 that this kind of structure also appears when we consider entanglement witnesses for nanoscale systems. Another important class of states are steady states, for which $\frac{d\hat{\rho}(t)}{dt} = 0$, i.e., we may write them as $\hat{\rho}(t) = \hat{\rho}_s$. To find the steady state of a system, we have to consider its time evolution, which we discuss in the next section. However, we already now note that for our example system, the steady state should (in accordance with statistical physics) be the thermal state

$$\hat{\rho}_s = \frac{e^{-\beta(\hat{H}_S - \mu\hat{a}^\dagger\hat{a})}}{\mathrm{tr}\left\{e^{-\beta(\hat{H}_S - \mu\hat{a}^\dagger\hat{a})}\right\}}, \tag{2.16}$$

with $\beta = 1/(k_B T)$ the inverse temperature and μ the chemical potential of the system (compared to the reservoir). The average occupation number is then

$$\bar{n} = \mathrm{tr}\{\hat{a}^\dagger \hat{a} \hat{\rho}_s\} = \frac{1}{e^{\beta(\varepsilon-\mu)} \pm 1}, \tag{2.17}$$

yielding the Fermi–Dirac distribution for fermions (+) and the Bose–Einstein distribution for bosons (−) (with $\mu = 0$ for non-conserved particles like photons). Note that $0 \leq \bar{n} \leq 1$ for fermions and $0 \leq \bar{n} < \infty$ for bosons. From now on we will use the sign convention that the upper signs in $\pm$ and $\mp$, respectively, always refer to the fermionic case and the lower signs refer to the bosonic case, unless otherwise stated.

Mixedness – Purity and entropy

We have already noted that any pure state may be described by a density matrix, but the opposite does not hold true. More precisely, a density matrix represents a pure state if and only if it has only one single non-zero eigenvalue (that is equal to 1). How mixed the state represented by a density matrix is may be quantified by its purity [2]

$$p = \mathrm{tr}\{\hat{\rho}(t)^2\}, \tag{2.18}$$

with $p = 1$ for pure states and $p < 1$ for mixed states. For a finite system of dimension d, the maximally mixed state $\hat{\rho} = \mathbf{I}/d$ gives the minimal purity $p = \frac{1}{d}$. For the qubit state in Eq. (2.15), we have $p = \frac{1+|\zeta|^2}{2}$.

As an alternative, one may characterize the mixedness by the von Neumann entropy [2]

$$S(t) = -\mathrm{tr}\{\hat{\rho}(t) \log \hat{\rho}(t)\}, \tag{2.19}$$

which is the quantum analog of the Boltzmann entropy $S = -k_B \sum_n p_n \log p_n$, with p_n the probability of being in a microstate n. The entropy is a measure of the average information obtained when one measures the exact microstate of a macrostate. For a pure state, the entropy is zero. The more mixed the state is, the larger entropy. As we will see in Ch. 3, the von Neumann entropy may be used to identify whether a pure state is entangled or not; if the overall state has zero entropy but the reduced density matrices have non-zero entropy, the state is entangled.

2.2 Time evolution

We now move on to consider the time evolution of quantum systems. For a closed system with Hamiltonian $\hat{H}_S(t)$ (where an explicit time dependence may describe work performed

via externally controllable degrees of freedom), the time evolution is obtained from the Schrödinger equation [49]

$$i\hbar\frac{d}{dt}|\Psi(t)\rangle = \hat{H}_S(t)|\Psi(t)\rangle, \tag{2.20}$$

or, in terms of density matrices, by the Liouville–von Neumann equation

$$\frac{d\hat{\rho}_S(t)}{dt} = -\frac{i}{\hbar}[\hat{H}_S(t), \hat{\rho}_S(t)]. \tag{2.21}$$

Alternatively, the time evolution may be represented by the time evolution operator

$$\hat{U}(t, t_0) = \mathcal{T}_{\leftarrow} e^{-\frac{i}{\hbar}\int_{t_0}^{t}\hat{H}_S(t')dt'}, \tag{2.22}$$

where $\mathcal{T}_{\leftarrow}$ is the time-ordering operator, ensuring a correct ordering of $\hat{H}_S(t)$ when it does not commute with itself at different times. This allows us to write $|\Psi(t)\rangle = \hat{U}(t, t_0)|\Psi(t_0)\rangle$ or $\hat{\rho}_S(t) = \hat{U}(t, t_0)\hat{\rho}_S(t_0)\hat{U}^\dagger(t, t_0) \equiv \Phi_{t,t_0}\hat{\rho}(t_0)$, where Φ_{t,t_0} is a so-called *quantum operation* or *quantum dynamical map* defining the time evolution of the density matrices [52].

The quantum operation originating from the Schrödinger equation displays several important properties ensuring that it maps physical states (density matrices) onto other physical states as time goes by; it is (i) linear, (ii) trace preserving and (iii) completely positive. The latter condition means that if the closed system, with Hilbert space $\mathcal{H}_S$, is extended with a generic n-level system, with Hilbert space C^n, the time evolution $\Phi_{t,t_0} \otimes I_n$ acting on the combined Hilbert space $\mathcal{H}_S \otimes C^n$ still preserves the positivity of the state. We will take the three properties (i)–(iii) as a definition of a quantum operation.

In addition to these criteria, the Schrödinger quantum operation also displays several properties that are characteristic for closed systems. For instance, the time evolution is unitary and preserves the von Neumann entropy of the system. This is connected to the fact that there is no heat exchange with the environment for a closed system. To account for heat (and particle) exchange we instead need to consider the time evolution of open systems.

2.2.1 Quantum operations

For an open quantum system, the equation of motion may become much more complicated than the Liouville–von Neumann equation [Eq. (2.21)]. However, under two quite general assumptions, we may still describe the time evolution within the framework of the quantum operations defined in the previous subsection. To this end, we consider a generic system coupled to an environment as shown in Fig. 2.2 (a). The first assumption is that the system together with its environment forms a closed system, i.e., the time evolution of the combined system is still described by the Lioville–von Neumann equation. The evolution

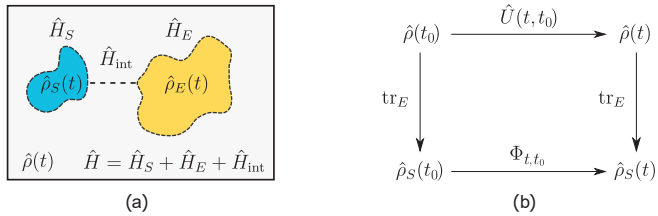

Figure 2.2: (a) An open system (blue), with Hamiltonian $\hat{H}_S$ and density matrix $\hat{\rho}_S(t)$, coupled to an environment (yellow), with Hamiltonian $\hat{H}_E$ and density matrix $\hat{\rho}_E(t)$, that together constitute a closed system, described by the total Hamiltonian $\hat{H}$ and density matrix $\hat{\rho}(t)$. The Hamiltonian $\hat{H}_{\rm int}$ describes the interaction between the system and its environment. (b) By considering the dynamics of the composite, closed system and then tracing out the environmental degrees of freedom one may derive a quantum dynamical map Φ_{t,t_0} that describes the time evolution of the reduced density matrix $\hat{\rho}_S(t)$ only.

of the system density matrix $\hat{\rho}_S(t)$ alone is then obtained by tracing out [c.f. Eq. (2.12)] the environmental degrees of freedom [52], yielding

$$\hat{\rho}_S(t) = \mathrm{tr}_E\{\hat{\rho}(t)\} = \mathrm{tr}_E\{\hat{U}(t,t_0)\hat{\rho}_S(t_0) \otimes |\Psi_E\rangle\langle\Psi_E|\hat{U}^\dagger(t,t_0)\} \equiv \Phi_{t,t_0}\hat{\rho}_S(t_0), \qquad (2.23)$$

where we have made use of the second assumption, that there are no correlations between the system and the environment at the initial time, i.e., $\hat{\rho}(t_0) = \hat{\rho}_S(t_0) \otimes |\Psi_E\rangle\langle\Psi_E|$. We note here that $\hat{U}^\dagger(t,t_0)$ now is the time evolution operator acting on the combined, closed system. The map Φ_{t,t_0} defined by Eq. (2.23) describes the effective time evolution of the system from time t_0 to t [see Fig. 2.23 (b)] and fulfills all the properties of a quantum operation [52]. We thus conclude that under very general assumptions the time evolution of an open system is described by quantum operations.

Introducing the *Kraus operators* $K_i(t) \equiv \langle\varphi_i|\hat{U}(t,0)|\Psi_E\rangle$, where $|\varphi_i\rangle$ is an orthonormal basis of the environment Hilbert space, we note that any quantum operation may be expressed as

$$\hat{\rho}_S(t) = \sum_i K_i(t)\hat{\rho}_S(t_0)K_i^\dagger(t), \qquad \sum_i K_i^\dagger(t)K_i(t) = 1. \qquad (2.24)$$

However, the quantum operations, or equivalently, the Kraus representations, can in general be very complicated; they may depend on the system, the environment and their mutual coupling. In general, they also depend on the initial time. For practical purposes they are thus not always the most convenient tools to describe the time evolution of open systems. We will therefore make another few assumptions to arrive at a simpler class of quantum operations used in Papers I, III and V called master equations.

2.2.2 Master equations

The idea behind master equations is to cast back the quantum operations into (time-local) first-order differential equations like the Liouville–von Neumann equation. In fact, all

divisible quantum operations, for which the inverse Φ_{t,t_0}^{-1} exists for all times $t \geq t_0$, lead to time-local master equations [52] of the form

$$\frac{d\hat{\rho}_S(t)}{dt} = \mathcal{L}_t \hat{\rho}_S(t), \tag{2.25}$$

where $\mathcal{L}_t$ is the *generator* of the master equation. An important class of divisible quantum operations are those fulfilling the *semigroup* property, $\Phi_{t_1,t_0}\Phi_{t_2,t_0} = \Phi_{t_1+t_2,t_0}$, for which the generator is time-independent, $\mathcal{L}_t = \mathcal{L}$. According to the Gorini–Kossakowski–Sudarshan–Lindblad theorem [53, 54] these generators have to take a very particular form (at least for finite-dimensional Hilbert spaces) described by the Lindblad equation

$$\frac{d\hat{\rho}_S(t)}{dt} = \mathcal{L}\hat{\rho}_S(t) = -\frac{i}{\hbar}[\hat{H}, \hat{\rho}_S(t)] + \sum_i \Gamma_i \left[\hat{L}_i \hat{\rho}_S(t) \hat{L}_i^\dagger - \frac{1}{2}\{\hat{L}_i^\dagger \hat{L}_i, \hat{\rho}_S(t)\}\right]. \tag{2.26}$$

Here, the first term on the right-hand side resembles the Liouville–von Neumann equation and describes the coherent time evolution of the system. However, $\hat{H}$ is not necessarily the same as the system Hamiltonian $\hat{H}_S$ of the system as it may also contain a Lamb shift (due to the effect of the environment on the energies of the system). Furthermore, the so-called jump operators $\hat{L}_i$ describe incoherent interactions (with rates Γ_i) between the system and the environment, e.g., transfer of heat and particles. The operators $\mathcal{D}_i\hat{\rho}_S(t) = \Gamma_i \left[\hat{L}_i \hat{\rho}_S(t) \hat{L}_i^\dagger - \frac{1}{2}\{\hat{L}_i^\dagger \hat{L}_i, \hat{\rho}_S(t)\}\right]$ are sometimes called *dissipators*. Time evolution under the Lindblad equation may be non-unitary and lead to a change of the von Neumann entropy of the system, a characteristic property of open systems.

The Lindblad equation – or the classical Pauli master equation where no coherences are present – is used extensively in both Papers I, III and V, and forms a cornerstone for all transport theory discussed in the remainder of this chapter. Importantly, this equation may be microscopically derived for example under the so-called Born–Markov approximation, where the coupling between the system and its environment is treated perturbatively to second order and the correlation times of the environment are assumed to be much shorter than the typical time scales of the system dynamics, see App. A for further details of the microscopic derivation of master equations.

The formal solution to the Lindblad equation may be written as

$$\hat{\rho}_S(t) = e^{\mathcal{L}t}\hat{\rho}_S(0), \tag{2.27}$$

where $\hat{\rho}_S(0)$ is the initial density matrix. The eigenvalues λ_α (which must be nonpositive to yield a physical solution) of the matrix representation of the Lindbladian $\mathcal{L}$ determines the time scales on which various transients die out. The trace preservation of the Lindblad equation ensures that there is always at least one steady-state solution $\hat{\rho}_s$ obtained from

$$\mathcal{L}\hat{\rho}_s = 0. \tag{2.28}$$

Provided that there is a unique steady-state, the system will approach this state after a sufficiently long time. When we consider transport statistics, we will typically assume that the system is starting in (i.e., has already reached) its steady state.

2.2.3 Jump operators and current operators

To use the Lindblad equation for practical purposes, one needs to identify the jump operators $\hat{L}_i$ describing the interaction of the system with its environment. These operators depend on the microscopic physics of the system and its coupling to the environment. In this thesis, we deal with two kinds of jump operators. The first one, used in Paper I, is

$$\hat{L}_i^{(d)} = \hat{a}^\dagger \hat{a}, \qquad \Gamma_i = \Gamma^{(d)}, \tag{2.29}$$

and represents pure *decoherence* with a decoherence time $1/\Gamma^{(d)}$. It suppresses any coherences of the density matrix on the time scale set by the decoherence time, unless there is another mechanism continuously creating new coherences.

In Papers I and V, we also use jump operators to describe emission and absorption of particles to a reservoir, with average occupation number $\bar{n}$, for which the jump operators are

$$\hat{L}^{(e)} = \hat{a}, \qquad \Gamma_i^{(e)} = \Gamma(1 \pm \bar{n}) \tag{2.30a}$$

$$\hat{L}^{(a)} = \hat{a}^\dagger, \qquad \Gamma_i^{(a)} = \Gamma\bar{n}. \tag{2.30b}$$

In this case, we note that we may interpret

$$\mathcal{J}_e\hat{\rho}_S(t) = \gamma(1 \pm \bar{n})\hat{a}\hat{\rho}_S(t)\hat{a}^\dagger, \qquad \mathcal{J}_a\hat{\rho}_S(t) = \gamma\bar{n}\hat{a}^\dagger\hat{\rho}_S(t)\hat{a}, \tag{2.31}$$

as emission and absorption current superoperators, respectively. Furthermore, we note that the emission and absorption rates fulfill detailed balance

$$\Gamma_i^{(e)} = e^{\beta\varepsilon}\Gamma_i^{(a)}, \tag{2.32}$$

where ε is the energy of the quanta that is being transferred.

As a concrete example of a Lindlbad equation, we note that for our example system we obtain

$$\frac{d\hat{\rho}(t)}{dt} = -\frac{i}{\hbar}\varepsilon[\hat{a}^\dagger\hat{a}, \hat{\rho}] + \gamma(1 \mp \bar{n})\left[\hat{a}\hat{\rho}(t)\hat{a}^\dagger - \frac{1}{2}\{\hat{a}^\dagger\hat{a}, \hat{\rho}\}\right] + \gamma\bar{n}\left[\hat{a}^\dagger\hat{\rho}(t)\hat{a} - \frac{1}{2}\{\hat{a}\hat{a}^\dagger, \hat{\rho}\}\right], \tag{2.33}$$

where we for brevity from now on have dropped the subindex S for the density matrix. Since the coherences decouple from the populations, we may, in this particular case, write

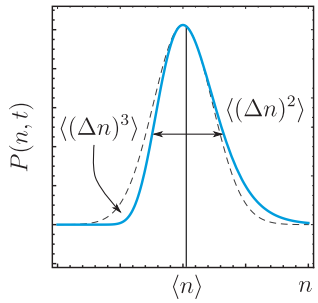

Figure 2.3: An illustration of a probability distribution $P(n,t)$ (blue, solid) with a Gaussian fit (black, dashed). The first three central moments describe the mean, the variance and the skewness of the distribution.

the Lindblad equation as a classical Pauli equation for the populations only. For instance, in the fermionic case we get

$$\frac{d}{dt}\begin{pmatrix} P_0(t) \\ P_1(t) \end{pmatrix} = \gamma \begin{pmatrix} -\bar{n} & 1-\bar{n} \\ \bar{n} & -1+\bar{n} \end{pmatrix} \begin{pmatrix} P_0(t) \\ P_1(t) \end{pmatrix}, \tag{2.34}$$

where $P_0(t) = \langle 0|\hat{\rho}(t)|0\rangle$ and $P_1(t) = \langle 1|\hat{\rho}(t)|1\rangle$ are the populations of the density matrix. Note that the steady state solution to this equation indeed yields the thermal state in Eq. (2.16) as previously claimed. In Paper III, we use another two-dimensional Pauli master equation to describe the probabilities of having zero or one excess electrons in a metallic island, where charging effects are present. This is further discussed in Ch. 4.

2.3 Transport statistics

Having introduced the important concepts of states, observables and time evolution, we are now in a position to consider what lies at the heart of this chapter: transport statistics. Considering the generic system in Fig. 2.1 (a), our aim is to describe transport between a quantum system and one or several reservoirs to which the system is coupled. Our focus will be on particle emission, however, all concepts may be generalized to absorption or net currents. Our aim is to not only find the average currents, but the *full counting statistics* in terms of the probability distribution $P(n,t)$ that n particles are emitted to a certain reservoir during a measurement time t, see Fig. 2.3. One may also consider joint probability distributions of various orders, such as $P(n_i, n_j, t)$, describing the probability that n_i particles are emitted to the ith reservoir and n_j particles are emitted to the jth reservoir during a measurement. Importantly, assuming that the system is in a steady state, these distributions only depend on the duration of the measurement and not the initial time.

As an alternative to the probability distributions themselves, one may consider the Laplace

transformed quantities, the so-called characteristic functions

$$\mathcal{M}(s,t) = \langle e^{ns} \rangle_t = \sum_n P(n,t) e^{ns}, \tag{2.35}$$

where s, often called a *counting field*, is the conjugate variable to n. This formula may easily be generalized to a multidimensional Laplace transform in the case of joint distributions. We note that by changing the counting field s to $i\chi$ (yielding a Fourier transform instead of a Laplace transform), one instead obtains the moment generating function (MGF). The difference between the MGF and the characteristic function is a subtle mathematical technicality and we will use them interchangeably in the following chapters.

The characteristic function contains exactly the same information as the probability distribution, but, as we will see, is typically easier to access theoretically. In addition, the characteristic function (or the MGF) yields the moments $\langle n^m \rangle_t$ of the probability distribution from its derivatives

$$\langle n^m \rangle_t = \left. \frac{\partial^m \mathcal{M}(s,t)}{\partial s^m} \right|_{s=0}, \tag{2.36}$$

which form the cofficients in the expansion $\mathcal{M}(s,t) = \sum_m \frac{s^m \langle n^m \rangle_t}{m!}$. The moments characterize the full probability distribution. For instance, $\langle n \rangle_t$ gives the average number of emitted particles, $\langle (\Delta n)^2 \rangle = \langle n^2 \rangle - \langle n \rangle^2$ gives the variance and $\langle (\Delta n)^3 \rangle = \langle n^3 \rangle - 3\langle n \rangle \langle n^2 \rangle + 2\langle n \rangle^3$ is related to the skewness, see Fig. 2.3. For the MGF, the derivatives are carried out with respect to $i\chi$ instead of s.

From the characteristic function, we may also extract other transport quantities, including waiting time distributions, correlation functions and long-time statistics, which may more clearly illustrate various transport characteristics, such as bunching and anti-bunching.

Full counting statistics extracted from the Lindblad equation

To extract the full counting statistics, i.e., the characteristic function, from the Lindblad equation, we first introduce the projector $\hat{\Pi}(n,t)$, which projects out the conditional part $\hat{\rho}(n,t)$ of a density matrix that describes the system provided that n particles have been emitted

$$\hat{\rho}(t) = \sum_n \hat{\Pi}(n,t) \hat{\rho}(t) \hat{\Pi}^\dagger(n,t) = \sum_n \hat{\rho}(n,t). \tag{2.37}$$

In particular, we have $\mathrm{tr}\{\hat{\rho}(n,t)\} = P(n,t)$, where $\hat{\rho}(n,t)$ is the number-resolved density matrix that describes the system under the condition that n particles have been emitted during a time t. From the Lindblad equation, we then obtain the number-resolved master equation

$$\frac{d\hat{\rho}(n,t)}{dt} = (\mathcal{L} - \mathcal{J}_e)\hat{\rho}(n,t) + \mathcal{J}_e \hat{\rho}(n+1,t), \tag{2.38}$$

where $\mathcal{J}_e$ is the emission current superoperator defined in Eq. (2.31). Using a Laplace transformation, we obtain

$$\frac{d\hat{\rho}(s,t)}{dt} = \mathcal{L}(s)\hat{\rho}(s,t) = (\mathcal{L} - \mathcal{J}_e)\hat{\rho}(s,t) + e^s \mathcal{J}_e \hat{\rho}(s,t), \tag{2.39}$$

where $\hat{\rho}(s,t) = \sum_n \hat{\rho}(n,t)e^{sn}$ is the Laplace transformed density matrix. The formal solution to this equation is

$$\hat{\rho}(s,t) = e^{\mathcal{L}(s)t}\hat{\rho}(0). \tag{2.40}$$

Here we choose $\hat{\rho}(0) = \hat{\rho}_s$ to consider steady-state transport. From this solution, we obtain the characteristic function as

$$\mathcal{M}(s,t) = \mathrm{tr}\{\hat{\rho}(s,t)\}. \tag{2.41}$$

In general, it may be challenging to compute the matrix exponential of the Lindbladian and various methods, including perturbative ones, have been developed for this purpose. In some cases, however, one may solve it analytically, such as for our example system. In that case, we obtain (see Paper V for further details about the derivation in the non-trivial bosonic case)

$$\mathcal{M}(s,t) = \left(\frac{2\xi e^{\gamma t/2}}{2\xi \cosh\left[\frac{\xi\gamma t}{2}\right] + (1+\xi^2)\sinh\left[\frac{\xi\gamma t}{2}\right]} \right)^{\mp 1} \tag{2.42}$$

with $\xi = \sqrt{1 \pm 4(e^s - 1)\bar{n}(1 \mp \bar{n})}$. In the bosonic case, this is one of the main findings of Paper V. It allows us to extract a number of other important transport quantities, such as the long-time statistics, the noise spectrum, the second-order degree of coherence and the waiting time distributions.

2.3.1 Long-time statistics

The solution to Eq. (2.40) is often difficult to find, and even more difficult to measure experimentally. It requires detectors with wide bandwidths, that can resolve fast processes on all relevant time scales where the Lindblad equation is valid. Unfortunately, in real experiments the bandwidths of current detectors are usually very limited, which means that only the characteristic function for very long times is accessible. One may therefore instead consider the long-time statistics, i.e., the statistics of the particle emissions in the limit of a very long measurement time. Such measurements yield surprisingly much information about the transport statistics and form a cornerstone of this thesis. In Ch. 3 and 4 we will see how long-time statistics can be used for both entanglement detection and quantum calorimetry.

In the long-time limit, we find from Eqs. (2.40) and (2.41)

$$\mathcal{M}(s,t) = \mathrm{tr}\{\hat{\rho}(s,t)\} = \mathrm{tr}\{e^{\mathcal{L}(s)t}\hat{\rho}(0)\} \approx e^{\lambda(s)t}\mathrm{tr}\{\hat{\rho}(0)\}, \tag{2.43}$$

where $\lambda(s)$ is the largest eigenvalue of $\mathcal{L}$ (closest to 0 since $\mathcal{L}$ only has non-positive eigenvalues). We note that the characteristic function is proportional to $e^{\lambda(s)t}$ in this limit. Introducing the so-called cumulant generating function (CGF), we then obtain

$$F(s,t) = \log[\mathcal{M}(s,t)] = t\lambda(s), \tag{2.44}$$

to exponential accuracy. The different derivatives of this function yield the cumulants

$$\langle\langle n^m \rangle\rangle_t = \left.\frac{\partial^m F(s,t)}{\partial^m s}\right|_{s=0}, \tag{2.45}$$

which form the cofficients in the expansion $F(s,t) = \sum_m \frac{s^m \langle\langle n^m \rangle\rangle_t}{m!}$. These are particularly favorable to analyze any deviations from Gaussian statistics, for which $\langle\langle n^m \rangle\rangle_t = 0$ for $m > 2$. The first cumulant is the same as the first moment, while the second and third cumulants equal the corresponding central moments

$$\langle\langle n \rangle\rangle_t = \langle n \rangle_t, \qquad \langle\langle n^2 \rangle\rangle_t = \langle (\Delta n)^2 \rangle_t, \quad \text{and} \quad \langle\langle n^3 \rangle\rangle_t = \langle (\Delta n)^3 \rangle_t. \tag{2.46}$$

For higher-order central moments and cumulants, the relation becomes more complicated, although there is still a linear transformation between the two.

A concrete, and important, example of a cumulant generating function is the one describing Poissonian statistics of particle emissions

$$F(s,t) = \gamma t(e^s - 1), \tag{2.47}$$

where γ is the emission rate. In this case, all the cumulants are identical. This is characteristic for the statistics of uncorrelated events.

The most important measurable quantity introduced in this chapter is the *zero-frequency noise*

$$S(0) = \lim_{t\to\infty} \frac{1}{t}\langle\langle n^2 \rangle\rangle_t. \tag{2.48}$$

This noise (or the cross correlated version) is used both for entanglement detection in Papers I and II as well as to describe temperature fluctuations in Papers III and IV and heat transport in Paper V. It is, together with average currents, the typical quantity that is accessible in nanoscale transport measurements.

For our example system, we obtain

$$F(s,t) = \frac{\gamma t}{2}\left(\mp 1 \pm \sqrt{1 \pm 4(e^s - 1)\bar{n}(1 \mp \bar{n})}\right). \tag{2.49}$$

The average emission current is $\langle\langle n \rangle\rangle_t = \gamma t \bar{n}(1 \mp \bar{n})$ and the noise is $\langle\langle n^2 \rangle\rangle_t = \gamma t \bar{n}(1 \mp \bar{n})[\bar{n}^2 + (1 \mp \bar{n})^2]$. Comparing with Eq. (2.47), we see that in this specific case the statistics is Poissonian (uncorrelated) if and only if $\bar{n} \ll 1$. Using the Poissonian limit as a reference, we may define the *Fano factor* $\mathcal{F}$ [55, 56] as the ratio between the zero-frequency noise and the average current in the long-time limit

$$\mathcal{F} \equiv \frac{\langle\langle n^2 \rangle\rangle_t}{\langle\langle n \rangle\rangle_t} = n^2 + (1 \mp n)^2. \tag{2.50}$$

For $\mathcal{F} < 1$, we say that the statistics is sub-Poissonian, while for $\mathcal{F} > 1$, we say that it is super-Poissonian. In some cases, these concepts are directly related to bunching and anti-bunching, however, not in general [57]. We see that the bosonic mode yields super-Poissonian statistics and the fermionic mode yields sub-Poissonian statistics, see Fig. 2.4 (a).

Saddle-point approximation

To regain the probability distribution $P(n,t) = \frac{1}{2\pi} \int ds e^{F(s,t)} e^{-sn}$ from the cumulant generating function we may use the saddle-point approximation [58]

$$\log P(n,t) \approx F(s^*,t) - s^* n, \tag{2.51}$$

with $s^*(n)$ the solution to the saddle-point equation

$$\left.\frac{\partial F(s,t)}{\partial s}\right|_{s=s^*} = n. \tag{2.52}$$

Here we stress that both n and $F(s,t)$ are large numbers in the long-time limit, thus making the saddle-point approximation valid. For our example system, in the limit $\bar{n} \ll 1$, we obtain the Poissonian distribution

$$\frac{\log P(n,t)}{t} \approx n\left(1 - \log\left[\frac{n}{\langle n \rangle}\right]\right) - \langle n \rangle, \tag{2.53}$$

with $\langle n \rangle = \bar{n}\gamma t$ the average number of emitted particles during the measurement time.

2.3.2 Noise spectrum $S(\omega)$

For detectors with finite bandwidths, or systems displaying slow processes, it is possible to investigate time-resolved phenomena. One way of characterizing the transport statistics then is to use the correlation function $\mathcal{C} = \langle\{\Delta\mathcal{J}_e(t), \Delta\mathcal{J}_e(0)\}\rangle$, with $\Delta\mathcal{J}_e = \mathcal{J}_e - \langle\mathcal{J}_e\rangle$ the current fluctuation operator, or its Fourier transform, yielding the noise spectrum

$$S(\omega) = \frac{1}{2}\int dt e^{j\omega t}\langle\{\Delta\mathcal{J}_e(t), \Delta\mathcal{J}_e(0)\}\rangle, \tag{2.54}$$

where $\{\hat{A},\hat{B}\} = \hat{A}\hat{B} + \hat{B}\hat{A}$ denotes the anti-commutator. From now on the expectation values are evaluated with respect to the steady state if nothing else is stated. For charge current correlations a prefactor e^2, stemming from the charge of the transferred quanta, is typically included. The noise spectrum tells us the frequencies of the fluctuations. For $\omega = 0$, this expression yields the zero-frequency noise consistent with the second cumulant of the long-time statistics in Eq. (2.48). One may also consider cross-correlations between emissions to *different* reservoirs α and β:

$$S^{\alpha\beta}(\omega) = \frac{1}{2}\int dt e^{i\omega t}\langle\{\Delta\mathcal{J}_e^{\alpha}(t), \Delta\mathcal{J}_e^{\beta}(0)\}\rangle, \tag{2.55}$$

where $\Delta\mathcal{J}_e^{\alpha,\beta}(t)$ denotes the current fluctuation operator of reservoir α, β. This quantity plays a central role in the next chapter to detect entanglement.

The noise spectrum may be computed from the time-dependent second cumulant obtained from the characteristic function in Eq. (2.41) by using MacDonald's formula [59–61]

$$S(\omega) = \omega\int_0^{\infty} dt \sin(\omega t)\frac{d}{dt}\langle\langle n^2\rangle\rangle_t. \tag{2.56}$$

For our example system, we get

$$S(\omega) = \langle\mathcal{J}_e\rangle \mp 2\frac{\gamma}{\gamma^2+\omega^2}\langle\mathcal{J}_e\rangle^2, \tag{2.57}$$

which is shown in Fig. 2.4 (b). The single resonance level is here manifested as a Lorentzian.

2.3.3 Second-order degree of coherence $g^{(2)}(\tau)$ function

An alternative way of characterizing transport statistics is to consider the second-order degree of coherence $g^{(2)}(\tau)$. The $g^{(2)}(\tau)$ function is in this thesis mainly used in Paper I to formulate a Bell inequality based on real-time measurements as well as in Paper V to characterize the photon emissions from a cavity. It is defined as [57]

$$g^{(2)}(\tau) = \frac{\langle\mathcal{J}_e e^{\mathcal{L}t}\mathcal{J}_e\rangle}{\langle\mathcal{J}_e\rangle^2}, \tag{2.58}$$

i.e., it is the (normalized) correlation function for two emission processes. The advantage of the $g^{(2)}(\tau)$ function is that it determines whether the transport statistics is bunched $[g^{(2)}(0) > g^{(2)}(\tau)]$ or anti-bunched $[g^{(2)}(0) < g^{(2)}(\tau)]$. Bunching means that the emission events tend to cluster together, a property typical for non-interacting bosons. Anti-bunching means the opposite and is typical for non-interacting fermions.

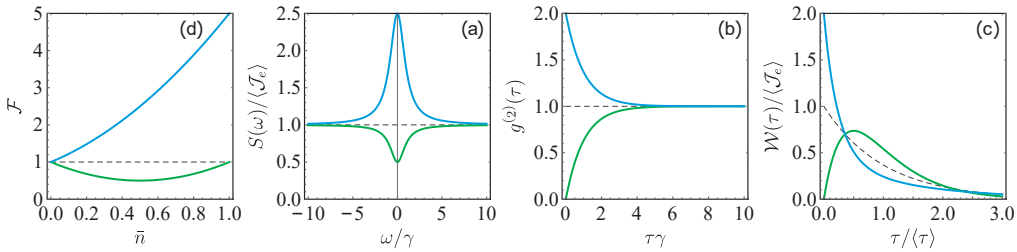

Figure 2.4: Steady-state emission statistics of a bosonic (blue) and a fermionic (green) resonance level weakly coupled (with rate γ) to a reservoir. Poissonian statistics indicated by dashed lines. (a) The Fano factor $\mathcal{F}$ as a function of the mean occupation number $\bar{n}$ (b) The noise spectrum $S(\omega)$ for $\bar{n} = 0.5$ as a function of the frequency ω with $\langle\mathcal{J}_e\rangle$ the average emission current. (c) The second-order degree of coherence $g^{(2)}(\tau)$ as a function of time τ for $\bar{n} = 0.5$. (d) The waiting time distribution $\mathcal{W}(\tau)$ for $\bar{n} = 0.5$ as a function of time τ with $\langle\tau\rangle$ the average waiting time.

We note that the $g^{(2)}(\tau)$ function is related to the noise spectrum [57] via

$$S(\omega) = \langle\mathcal{J}_e\rangle + \langle\mathcal{J}_e\rangle^2 \int_{-\infty}^{\infty} d\tau e^{i\omega\tau}(g^{(2)}(\tau) - 1). \tag{2.59}$$

Provided that we know the average current, they contain the same information about the transport statistics.

For our simple example system, we obtain

$$g^{(2)}(\tau) = 1 \mp e^{-\gamma|\tau|}. \tag{2.60}$$

This is plotted in Fig. 2.4 (c). Here we see the Pauli principle manifested as $g^{(2)}(0) = 0$ in the fermionic case; there cannot be two subsequent emissions without the dot being refilled in between. This implies that the emissions are anti-bunched [57]. In the bosonic case, the emissions are instead bunched. In both cases, for long times $\tau \gg 1/\gamma$, we see that the emission events are uncorrelated and thus $g^{(2)}(\tau) \to 1$ for $\tau \to \infty$. In Paper 5, we discuss the properties of bosonic emission statistics in further detail.

2.3.4 Waiting time distributions

Yet another way of characterizing transport statistics is to use waiting time distributions (WTDs), one of the main concepts of Paper V. The WTD describes the probability distribution of waiting times between successive emission events. It is for that reason sometimes referred to as an *exclusive* probability as no other emission event is allowed in between [62]. Besides a somewhat different normalization, it resembles to a large extent of $g^{(2)}(\tau)$; however, for the $g^{(2)}(\tau)$ function emissions are allowed to take place in between. Mathematically, the WTD is defined as [57]

$$\mathcal{W}(\tau) = \frac{\langle\mathcal{J}_e e^{(\mathcal{L}-\mathcal{J}_e)t}\mathcal{J}_e\rangle}{\langle\mathcal{J}_e\rangle}. \tag{2.61}$$

For steady states, as considered here, the WTD may be obtained from the characteristic function in Eq. (2.41) as [63, 64]

$$\mathcal{W}(\tau) = \frac{1}{\langle\tau\rangle}\partial_\tau^2\chi(-\infty,\tau), \tag{2.62}$$

where $\langle\tau\rangle = \int_0^\infty \mathcal{W}(\tau)\tau d\tau$ is the mean waiting time.

For our example systems, we find

$$\mathcal{W}(\tau) = \gamma(1-\alpha^2)\frac{\sinh\left[\frac{\alpha\gamma t}{2}\right]}{2\alpha}e^{-\gamma t/2} \tag{2.63}$$

in the fermionic case, and (see Paper V for the derivation)

$$\mathcal{W}(\tau) = \gamma\alpha(\alpha^2-1)\frac{-1+3\alpha^2+(1+\alpha^2)\cosh[\alpha\gamma t]+2\alpha\sinh[\alpha\gamma t]}{\left(2\alpha\cosh\left[\frac{\alpha\gamma t}{2}\right]+(1+\alpha^2)\sinh\left[\frac{\alpha\gamma t}{2}\right]\right)^3}e^{\gamma t/2} \tag{2.64}$$

in the bosonic case, with $\alpha = \lim_{s\to-\infty}\sqrt{1\pm 4(e^s-1)\bar{n}(1\mp\bar{n})} = |1\mp 2\bar{n}|$ in both cases. The WTDs are both plotted in Fig. 2.4 (d). As seen in the figure, the bunching and anti-bunching behavior of bosons and fermions, respectively, are clearly manifested in the WTD. For instance, we have $\mathcal{W}(0) = 0$ in the fermionic case since two immediately successive emissions cannot take place as the system needs to be refilled with a particle in between. For the bosons, we instead have $\mathcal{W}(0) = 2\gamma\bar{n}(1+\bar{n})$, i.e., there is an enhancement in the emission immediately after an emission event has taken place.

Renewal processes

In the fermionic case, we find the interesting relation

$$g^{(2)}(s) = \frac{\mathcal{W}(s)}{\langle\mathcal{J}_e\rangle\left[1-\mathcal{W}(s)\right]}, \tag{2.65}$$

between the Laplaced transformed $g^{(2)}(\tau)$ and WTD. This is a general relation that holds for any so-called *renewal process* where subsequent waiting times are uncorrelated [62]. However, in general no such relation exists between the WTD and the $g^{(2)}(\tau)$ function. The bosonic resonance level is an example of this; in that case subsequent waiting times are correlated as the number of bosons is not reset to the same number after each emission. No relation between the $g^{(2)}(\tau)$ and WTD exists then, which is an important finding of Paper V and an illustration of the fact that the two concepts, in general, contain different information about the transport statistics.

2.4 Summary and outlook

In this chapter, we have introduced a number of basic concepts to describe transport phenomena in nanoscale systems. A substantial part of the chapter has been devoted to the theory of open quantum systems, where the Lindblad equation plays a central role. This equation, as well as its classical analog – the Pauli master equation – are widely used in this thesis to describe everything from the generation of entangled electrons in quantum dot systems (Paper I) to the emission of photons from a microwave cavity (Paper V). Some of these examples will be discussed in further detail in the following chapters.

Among the concepts introduced to characterize transport statistics, the zero-frequency noise constitutes the most important one for this thesis. The reason is that detectors of, e.g., currents or temperature in nanoscale systems typically have very limited bandwidths. This prevents time-resolved detection of fast phenomena, which is necessary to obtain for instance the waiting time distribution or the full noise spectrum. However, thanks to zero-frequency noise measurements it is, even with a very limited bandwidth, possible to extract a substantial amount of information of the transport characteristics. We will for example see in the following chapters how zero-frequency noise measurements may be used to detect both quantum correlations and temperature fluctuations.

That said, we also note that recent developments of single-electron [65–68] and single-photon detectors [69–73] for nanoscale systems open up completely new possibilities to investigate transport phenomena. As an example, we propose in Paper I a way of testing a Bell inequality using $g^{(2)}(\tau)$ functions measured for electrons in a quantum dot system. Another example is found in Paper V, where we investigate theoretically single photon emissions from a microwave cavity. Here single-photon detectors could make it possible to investigate waiting time distributions of a non-renewal process.

Finally, we note that many of the concepts introduced in this chapter have been applied to describe particle emission current statistics. However, one may extend these concepts to more general situations, for instance to describe particle net currents or heat currents. It is also possible to consider setups where currents are detected at different junctions, and to introduce different counting fields to describe the statistics of each current. In this way, we may extract current cross-correlations, which are essential for Papers I and II and will be further discussed in the next chapter.

Chapter 3

Quantum entanglement

In this chapter, we introduce one of the two main topics of this thesis: quantum entanglement. Entangled states are composite states of particles whose individual quantum states cannot be described independently of each other. At first sight, these states may seem insignificant. However, as Einstein, Podolsky and Rosen (EPR) highlighted in 1935 [4], entangled states may give rise to seemingly counterintuitive results, violating the classical notion of local realism. EPR argued that this violation was a result of the absence of so-called "hidden variables", missing variables that would bring quantum mechanics back into the realm of local realism and even determinism. This sparked a metaphysical debate on whether quantum mechanics provides a complete description of reality, a debate which was settled only in 1964. That year, Bell presented [5] an inequality to experimentally test the validity of local realism, paving the way for a series of experiments [74–79], that turned out to be in favour of quantum mechanics.

However, it was not until the 1980s, with the advent of quantum information theory, that the real power of entanglement was fully understood. Entanglement then emerged as, not only a peculiar feature of quantum mechanics, but an indispensable resource for quantum information processing. Today, we know that entangled states constitute a key ingredient for many quantum information protocols, including superdense coding [7], quantum teleportation [8] and quantum cryptography [9]. In addition, entangled qubits are crucial to realizing universal quantum computing. The importance of entanglement as a computational resource has motivated a tremendous amount of research, including Papers I and II of this thesis, aiming to develop schemes for generating, manipulating and detecting entangled states in controllable ways.

In this chapter, we present an overview of the theory underlying Papers I and II as well as a summary of the main findings of these two papers. We start by considering the fundamental

aspects of entanglement that originally led to its discovery (Sec. 3.1) and based on this introduce the formal definition of entanglement (Sec. 3.2). We then consider the generation of entangled electrons in nanoscale systems (Sec. 3.4), with a focus on the quantum dot system proposed in Paper I, and briefly discuss how to quantify entanglement in terms of entanglement measures (Sec. 3.4). Finally, we discuss entanglement detection schemes based on zero-frequency current cross-correlation measurements (Sec. 3.5), both in terms of Bell inequalities and entanglement witnesses. The latter includes an overview of the main findings of Paper II. We end the chapter with a conclusion and outlook (Sec. 3.6).

3.1 EPR paradox and Bell tests

The peculiar features of entangled states were first highlighted by Einstein, Podolsky and Rosen (EPR) in their famous paper [4] from 1935, where they presented a thought experiment, now known as the EPR paradox, in an attempt to prove that quantum mechanics is an incomplete theory. The thought experiment revolves around the Heisenberg uncertainty relation [Eq. (2.3)] for two particles, A and B, that have previously been interacting and then spatially separated. The interaction is assumed to have caused the states of the particles to be correlated. In the original formulation of the paradox, EPR considered correlations between the positions and momenta of the particles. Inspired by the formulation of the EPR paradox by Bohm [80], we here instead consider electrons whose spins are correlated, an example which is more relevant for the nanoscale systems discussed in this thesis.

Given a certain projection axis, each electron has a spin that may point either up or down along that axis. The EPR paradox is most clearly illustrated by assuming that the composite state $|\Psi\rangle$ of the spins, after having interacted, is described by a singlet state (with total spin zero)

$$|\Psi\rangle = \frac{1}{\sqrt{2}} \left(|+\rangle_A |-\rangle_B - |-\rangle_A |+\rangle_B \right), \tag{3.1}$$

where the signs ($+$ and $-$) indicate the spin direction (parallel or anti-parallel, respectively) of each particle along a certain projection axis. This composite state has the peculiar property that, while we know the total spin with certainty, we know nothing about the individual spins. More precisely, according to quantum mechanics, the spin of, say, particle A along a direction $\mathbf{a}$ (where $\mathbf{a}$ is a unit vector), represented by the operator $\hat{A}(\mathbf{a}) = \hat{\sigma}_{\mathbf{a}} = \mathbf{a} \cdot \boldsymbol{\sigma}$, lacks reality. Only after measuring the spin along $\mathbf{a}$, thus projecting its state onto one of the eigenstates of $\hat{A}(\mathbf{a})$, we may assign a certain state vector to that particle. Importantly, the reality of the system after a measurement will depend on the projection axis used; the measurement unavoidably affects the reality in accordance with the Heisenberg uncertainty principle.

Now, if we would instead measure both the spin of particle A (along $\mathbf{a}$) and the spin of particle B (along $\mathbf{b}$), the correlation between these measurements would be

$$E(\mathbf{a},\mathbf{b}) = \langle\Psi|\hat{\sigma}^A_{\mathbf{a}} \otimes \hat{\sigma}^B_{\mathbf{b}}|\Psi\rangle = -\mathbf{a}\cdot\mathbf{b}. \tag{3.2}$$

Here we note that, for parallel projection axes at A and B, the measurement outcomes would be perfectly anti-correlated. Thus, by measuring on particle A only, we obtain full information about the state of not only particle A, but also particle B. We can thus assign a state vector to particle B. However, the principle of local realism prescribes that a measurement at A cannot instantaneously affect the reality of the spatially separated particle B. This leads to the very startling result: Depending on the measurement axis chosen for the measurement at A, we may assign different state vectors to one and the same reality at B. However, according to the Heisenberg uncertainty relation, it is impossible for states representing definite values of different non-commuting variables to describe the same reality. This leads to the contradiction that is now known as the EPR paradox.

Based on this seemingly contradictory result, EPR concluded that quantum mechanics must be an incomplete theory in need of some additional, lacking elements, so-called hidden variables. These variables would, they believed, turn quantum mechanics into a complete theory, with the ability to predict the outcome of any single measurement. This idea was not new; de Broglie had already in 1927 [81] started to formulate such a theory based on so-called pilot-waves, a work that was later completed by Bohm in 1952 [82, 83]. However, this theory was highly non-local and inconsistent with the local realistic worldview of EPR.

For a long time, it was therefore unclear whether the claims by EPR – that it should be possible to predict the outcome of single measurements with a local hidden variable theory – was more than merely a philosophical question. However, in 1964, Bell showed [5] that the claims by EPR could be tested experimentally, thus paving the way for settling an almost 30 year long debate. Assuming a local hidden variable theory, Bell introduced a variable λ that would, with certainty, determine the outcomes $A(\mathbf{a},\lambda), B(\mathbf{b},\lambda)$ of measurements along $\mathbf{a}$ and $\mathbf{b}$ on each respective particle. From now on we will call $\mathbf{a}$ and $\mathbf{b}$ for the *detector settings*. Locality prescribes that the settings chosen at particle A do not influence the outcome at particle B, and vice versa. Each emitted pair may be associated with a certain value of the hidden variable λ. Introducing $p(\lambda)$ as the probability that the state of an emitted pair of particles is associated with λ, the measured expectation value of the correlations (with no knowledge about the actual hidden variables) would be

$$E(\mathbf{a},\mathbf{b}) = \int d\lambda A(\mathbf{a},\lambda)B(\mathbf{b},\lambda)p(\lambda). \tag{3.3}$$

Bell found that these expectation values have to fulfill certain inequalities [5], now known as Bell inequalities. Here we will use such an inequality, the CHSH inequality, formulated by Clauser–Horn–Shimony–Holt (CHSH) in 1969 [84]

$$\mathcal{B} \equiv |E(\mathbf{a},\mathbf{b}) + E(\mathbf{a}',\mathbf{b}) + E(\mathbf{a},\mathbf{b}') - E(\mathbf{a}',\mathbf{b}')| \leq 2, \tag{3.4}$$

where $\mathcal{B}$ is the so-called Bell parameter and $\mathbf{a}, \mathbf{a}', \mathbf{b}, \mathbf{b}'$ denote different detector settings. Quite surprisingly, the correlation functions given by quantum mechanics in Eq. (3.2) may violate this inequality; in fact they may reach values of $\mathcal{B}$ as large as $2\sqrt{2}$. Thus, if quantum mechanics is correct, it should be possible to violate the CHSH inequality in a real experiment and reject local realism as a property of our world.

This insight spurred a series of so-called Bell experiments, with the aim of testing if the Bell inequalities, such as the CHSH inequality, could be violated. The first experiments took place already in the 1970s [74, 75], and utilized polarized entangled photons. The polarization state of a photon may be read out by using polarizers, with two output channels $A\pm$ and $B\pm$, respectively. The measured value of the correlation coefficient is then obtained from

$$E(\mathbf{a}, \mathbf{b}) = \frac{N_{AB}^{++} - N_{AB}^{+-} - N_{AB}^{-+} + N_{AB}^{--}}{N_{AB}^{++} + N_{AB}^{+-} + N_{AB}^{-+} + N_{AB}^{--}}, \tag{3.5}$$

where $N_{AB}^{\pm\pm}$ are the number of pairs of particles detected at each combination of output ports at the A and B polarizers. While challenging to entangle, photons have the advantage that they may be separated coherently – and thus keep the entanglement intact – over long distances. The first experiments indicated that the CHSH inequality could be violated. Later experiments, such as those by Aspect et al. [76, 85] in the 1980s and 1990s, tried to address various so-called loopholes, possible ways of explaining Bell violations without necessarily abandoning local realism. For instance, one needs to ensure that no information may be exchanged between the detector systems during the measurements (the locality assumption) [76, 86–88], that the settings are chosen independently of the emitted state (the freedom-of-choice assumption) [89] and, for detectors with finite efficiencies, that the detected particles constitute a statistically representative set of all emitted particles (the fair-sampling assumption) [90]. It was not until 2015 that all these loopholes were closed simultaneously in one and the same experiment [77–79]. Even later, additional experiments have been carried out with the aim of improving the freedom-of-choice assumption, for instance by using pulses obtained from quasars to randomly select the detector settings in the Bell tests [91].

3.2 Separable and entangled states

The singlet state in Eq. (3.1) is just one of many examples of entangled states sharing the startling features illustrated in the EPR paradox. We now give a proper definition of entangled states and the complementary set of states, the separable states. We also present some of the methods to determine mathematically whether a certain state vector or density matrix is entangled or separable.

To define entanglement and separability, we first need to specify over what partition(s)

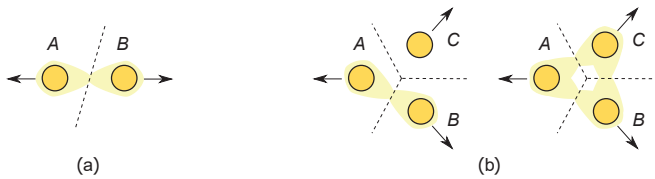

Figure 3.1: (a) A bipartite system consisting of two particles (yellow discs), with a partition separating the two subsystems. (b) For a multipartite system, consisting of more than two particles (here three), the states may be entangled either with respect to only one partition (left figure) or several/all partitions (right figure). In this thesis, we mainly focus on bipartite entanglement.

a state is entangled/separable, see Fig. 3.1. A state may be entangled with respect to one partition, but not to another. Focusing on bipartite entanglement, Fig. 3.1 (a), we consider a system partitioned into two subsystems A and B, with Hilbert spaces $\mathcal{H}_A$ and $\mathcal{H}_B$. We stress that all definitions below can be easily generalized to multipartite entanglement, where more than one partition is involved, see Fig. 3.1 (b).

3.2.1 Pure states

In the case of pure states, represented by state vectors $|\Psi\rangle \in \mathcal{H}_A \otimes \mathcal{H}_B$, a state is *separable* if and only if it may be written in a product form

$$|\Psi\rangle = |\Phi\rangle_A \otimes |\Omega\rangle_B, \tag{3.6}$$

where $|\Phi\rangle_A \in \mathcal{H}_A$ and $|\Omega\rangle_B \in \mathcal{H}_B$ are state vectors of subsystems A and B, respectively. Any pure state which is not separable, and thus cannot be written as in Eq. (3.6), is an *entangled* state.

Considering a measurement of an observable $\hat{A}_{\mathbf{a}}$ on subsystem A and another observable $\hat{B}_{\mathbf{b}}$ on subsystem B, the expectation value for a combined measurement factorizes

$$E(\mathbf{a}, \mathbf{b}) = \langle\Psi|\hat{A}_{\mathbf{a}} \otimes \hat{B}_{\mathbf{b}}|\Psi\rangle = \langle\Phi|\hat{A}_{\mathbf{a}}|\Phi\rangle_A \langle\Omega|\hat{B}_{\mathbf{b}}|\Omega\rangle_B, \tag{3.7}$$

for separable states, i.e., local measurement outcomes are independent. Most importantly, this is not the case for entangled states, for which correlations – quantum correlations – between the subsystems do exist.

Schmidt decomposition

To determine if a bipartite state may be expressed in a product form or not, one may employ the Schmidt decomposition [2] of a state vector

$$|\Psi\rangle = \sum_{i=1}^{d} \alpha_i |\Phi_i\rangle_A \otimes |\Omega_i\rangle_B, \qquad \sum_{i=1}^{d} \alpha_i^2 = 1, \tag{3.8}$$

where $\{|\Phi_i\rangle_A\}_{i=1}^{d_A}$ and $\{|\Omega_i\rangle_B\}_{i=1}^{d_B}$ form bases for $\mathcal{H}_A$ and $\mathcal{H}_B$, with $d = \min(d_A, d_B)$. Here the Schmidt coefficients $\alpha_i \geq 0$ are positive numbers that fully characterize the separability/entanglement of a bipartite system. In practice, the Schmidt decomposition is obtained by writing the state vector in a matrix form and then applying a single value decomposition.

The number of nonzero Schmidt coefficients is called the Schmidt rank or the Schmidt number. Whenever the Schmidt rank is larger than one, the state is entangled. Interestingly, the Schmidt rank is related to the purity of the reduced density matrix of one of the subsystems:

$$p(\hat{\rho}_A) = \mathrm{tr}_A \left\{ (\mathrm{tr}_B \hat{\rho})^2 \right\} = p(\hat{\rho}_B) = \mathrm{tr}_B \left\{ (\mathrm{tr}_A \hat{\rho})^2 \right\} = \sum_{i=0}^{d} \alpha_i^4 \leq 1. \tag{3.9}$$

Equality holds if and only if the Schmidt rank is one; this means that a bipartite pure state is entangled if and only if its reduced states are mixed.

Bell states

For a two qubit system, the four Bell states are defined as the entangled states

$$|\Psi_\pm\rangle = \frac{1}{\sqrt{2}} \left(|+-\rangle \pm |-+\rangle \right), \qquad |\Phi_\pm\rangle = \frac{1}{\sqrt{2}} \left(|++\rangle \pm |--\rangle \right), \tag{3.10}$$

of which the singlet state in Eq. (3.1) corresponds to $|\Psi_-\rangle$. Their reduced states, when integrating out the degrees of freedom of one of the subsystems, are maximally mixed. These states are known as maximally entangled states. They form a key ingredient in superdense coding [7], quantum teleportation [8] and quantum cryptography [9]. Thus, many entanglement generation schemes aim at creating this class of states.

3.2.2 Mixed states

The definition of entangled pure states in terms of correlations may be extended to all mixed states. However, some care has to be taken since mixed states may also contain classical correlations, which are not owing to entanglement. We therefore has to distinguish

between classical correlations and quantum correlations. Classical correlations are correlations which can be produced from local operations and classical communication (LOCC). This includes all operations that may be performed locally on each subsystem, either independently or correlated, via classical communication, with the other subsystem. There is no simple expression for parametrizing LOCC operations in general, but they may all be written as a product of local operations

$$\hat{V} = \hat{V}_A \otimes \hat{V}_B, \tag{3.11}$$

where $\hat{V}_A$ and $\hat{V}_B$ act only on subsystem A and B, respectively. Surprisingly, the converse is not true: not all products of local operations can be implemented as LOCC operations [92]. An important class of LOCC operations are the local unitary operations

$$\hat{U} = \hat{U}_A \otimes \hat{U}_B, \tag{3.12}$$

where $\hat{U}_A$ and $\hat{U}_B$ are both unitary operators acting on each subsystem. These correspond to a change of basis at each subsystem, which do not change the amount of entanglement.

A bipartite mixed state which only contains classical correlations may be written as

$$\hat{\rho} = \sum_i p_i \hat{\rho}_A^{(i)} \otimes \hat{\rho}_B^{(i)}, \qquad \sum_i p_i = 1. \tag{3.13}$$

This corresponds to an incoherent mixture, where we with probability p_i find subsystem A in the state $\hat{\rho}_A^{(i)}$ and subsystem B in the state $\hat{\rho}_B^{(i)}$. Only if $p_i = 0$ for all i except one, this state reduces to a product state, for which no correlations between the subsystems exist at all. It follows from Eq. (3.13) that the set of separable states is convex, a property that will be particularly important when we discuss entanglement witnesses.

We note that the expectation value of two local measurements for a separable state is given by

$$E(\mathbf{a}, \mathbf{b}) = \langle \Psi | \hat{A}_\mathbf{a} \otimes \hat{B}_\mathbf{b} | \Psi \rangle = \sum_i p_i \mathrm{tr}\left\{ \hat{A}_\mathbf{a} \hat{\rho}_A^{(i)} \right\} \mathrm{tr}\left\{ \hat{B}_\mathbf{b} \hat{\rho}_B^{(i)} \right\}. \tag{3.14}$$

This expectation value can always be mimicked by one obtained from a local hidden variable theory [see Eq. (3.3)].

We define any state which cannot be written in the form given by Eq. (3.13), thus containing quantum correlations, as entangled. Quite surprisingly, not all entangled mixed states violate the principle of local realism. One example is the Werner states [93]

$$\hat{\rho}_W = \lambda \hat{\mathbf{I}}/4 + (1 - \lambda) |\Psi_-\rangle\langle\Psi_-|, \tag{3.15}$$

which may model a singlet state that is exposed to noise. They are entangled for $0 \leq \lambda < 2/3$, but violates local realism only for $0 \leq \lambda < 1/\sqrt{2}$.

Peres–Horodecki criterion

Determining whether a mixed state is separable or entangled is an increasingly challenging task as the dimensions of a Hilbert space increases. In general, there is no known efficient method to determine if a state is entangled. However, for two-qubit systems, which are the relevant systems for Papers I and II, there is a simple and efficient method, known as the Peres–Horodecki criterion [94]. This criterion prescribes that a state is separable if and only its partial transpose

$$\hat{\rho}^{T_A} = \left(\sum_{ijkl} c_{ij}^{kl} |i\rangle_A |k\rangle_B \langle l|_B \langle j|_A \right)^{T_A} = \sum_{ijkl} c_{ji}^{kl} |i\rangle_A |j\rangle_B \langle k|_B \langle l|_A \tag{3.16}$$

is also a physical state (i.e., a positive operator). This statement is clear from Eq. (3.13). Thus, any state producing an unphysical state under the partial transpose must be entangled. For systems with dimensions $2x2$ or $2x3$, the Peres–Horodecki criterion is a necessary *and* sufficient condition for entanglement. However, for larger dimensions the criterion is only a sufficient condition; in that case there are entangled states which may yield physical states under the partial transpose [95].

3.3 Generation of entanglement in nanoscale systems

Having introduced the formal definition of entanglement, we now consider how to generate entangled states physically. Any degree of freedom, including photons, nuclear spins, electron spins, ion traps and quantum dots, may in principle be utilized to produce entangled states [2]. However, for practical purposes, it is important to choose a degree of freedom that provides good conditions for quantum computing applications. The so-called DiVincenczo criteria [96] prescribe that one needs degrees of freedom where well-defined qubits may be initiated, manipulated and read-out, without losing the quantumness due to decoherence. As a rule of thumb, there is a trade-off between good read-out control and long decoherence times. A degree of freedom interacting more strongly with its environment is typically easier to read out, but is at the same time also more sensitive to noise induced by the environment, leading to shorter decoherence times. One of the more extreme examples in this regard is nuclear spins, which may retain their coherences over very long times, even days, but are hard to control and manipulate, limiting their usefulness for future quantum computers.

The prospects of scalability as well as integrability with conventional electronics make entangled electrons in nanoscale systems particularly interesting [16, 17]. However, due to the strong interaction of electrons with their environment, these systems are typically impaired

by short decoherence times in the nano- to microsecond range [97], thus requiring fast coherent control of the systems. The spin degree of freedom of electrons [31, 98, 99] provides a natural two-level system that may be used as a qubit [20, 100, 101]. Experiments with one- and two-qubit systems have demonstrated the possibility of both controling the spins coherently [102, 103] and entangling them [104, 105]. Measurements have shown that such qubits can reach relatively long decoherence times, typically of the order of microseconds [97]. A natural resource of singlet-entangled electrons is found in *s*-wave superconductors, from which singlet states may be extracted via Cooper pair splitters [106–109].

Despite the prospects of all-electrical quantum state control and readout, much less attention has been devoted to orbital entanglement, where the charge degree of freedom is used in, e.g., ballistic channels [18, 19, 24–26, 33] or quantum dots [21, 22, 110, 111]. The main reason is the short decoherence time, typically in the nanosecond range [27–30], stemming from severe charge noise induced from the environment. While recent experiments have demonstrated coherent manipulation of single-electron orbital qubits [112–114] on the picosecond time scale, no experiment up to date has provided an unambigious test of orbital entanglement. This motivated the work in Paper I, where we propose a quantum dot-based setup to generate and detect orbitally entangled electrons via cotunneling processes that take place on a time scale much shorter than the decoherence time. This setup paves the way for a proof-of-principle experiment on orbital entanglement between electrons. In the following subsection we summarize the main idea and some of the main results of this work.

3.3.1 Sub-decoherence time generation of orbital entanglement

The system considered in Paper I [see Fig. 3.2 (a)] consists of three pairs of nearest-neighbour coupled quantum dots, with one pair forming an entangler (*E*) and the other two each forming part of a detector system (*A* and *B*, respectively). Henceforth, the dots will be indexed by $\gamma = 1, 2, A+, A-, B+, B-$, with $\gamma = 1, 2$ for the entangler dots, $\gamma = A+, A- \equiv \alpha$ for the dots at the *A* side and $\gamma = B+, B- \equiv \beta$ for the dots at the *B* side. Each dot is also coupled to a reservoir, denoted by the same γ. Keeping the reservoirs in the middle at finite bias and the other four grounded, electrons are injected into the entangler dots and extracted from the detector dots. Each dot has only one resonance level ϵ_γ within the transport window, with strong on-site Coulomb interaction preventing two electrons from occupying the same dot. Furthermore, the system is operated in the high-bias limit, i.e., the resonance levels are placed well inside the transport window, allowing us to effectively put the temperature to zero.

The intended entanglement generation cycle is shown in Fig. 3.2 (b). First, the entangler dots are filled with electrons from the reservoirs at rates Γ_1 and Γ_2, respectively. Tuning the single-particle energy levels ϵ_γ of the dots off resonance, subsequent sequential tunneling

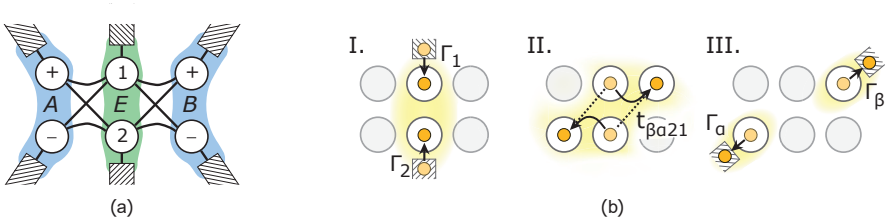

Figure 3.2: (a) The proposed quantum dot based setup consisting of two entangler dots (E) and two pairs of detector dots (A and B). Each dot is tunnel-coupled to nearest neighbors as well as to a reservoir. (b) The entanglement generation–detection cycle with pairs of electrons injected through the two reservoirs in the middle (I), then transferred via cotunneling to the detector dots (here showing one of four possible processes) (II) and finally extracted through any of the four reservoirs on the sides. This figure is taken from Paper I.

to the detector dots is suppressed. Instead, tuning the two-particle cotunneling processes on resonance,

$$\epsilon_1 + \epsilon_2 + U_{12} \approx \epsilon_\alpha + \epsilon_\beta + U_{\alpha\beta}, \tag{3.17}$$

where $U_{\gamma\gamma'}$ is the inter-dot Coulomb repulsion between dot γ and γ', the two electrons will cotunnel, with one going to detector system A and the other to detector system B (strong inter-dot interaction prevents the two from going to the same detector system). The electrons may end up in the detector dots in four possible combinations: $A{+}B{+}$, $A{+}B{-}$, $A{-}B{+}$ and $A{-}B{-}$, similar to the spin experiment in the EPR paradox. The electrons eventually leave the dot system at rates $\Gamma_\alpha, \Gamma_\beta$ through any of the four reservoirs on the sides. We are considering the regime where $\Gamma_\alpha, \Gamma_\beta \gg \Gamma_1, \Gamma_2 \gg t_{\beta\alpha 21}/\hbar$, for which the electrons tunnel out of the system before new electrons tunnel into the entangler dots. In this regime, back-tunneling of electrons from the detector dots to the entangler dots is also negligible.

Most importantly, the cotunneling processes take place on the picosecond time scale, i.e., on a time scale much faster than the typical decoherence time, which is of the order of nanoseconds [27–30]. The cotunneling time Δt may be estimated from $\Delta E \Delta t \geq \hbar$, where ΔE is the energy of the intermediate state where one electron has tunneled to a detector dot but not yet the other. For a typical energy of $\Delta E = 1$ meV, we get $\Delta t \sim 1$ ps. This estimate shows that the cotunneling processes indeed take place on a much shorter time scale than the decoherence from the environment.

Hamiltonian

As we show below, the cotunneling processes from the entangler dots to the detector dots may be seen as the emission of an entangled state that is locally rotated (the tunnel couplings effectively work as an electronic beam splitter) on the way to the detector dots. The emitted state is orbitally entangled, with a superposition between the upper electron going to the left and the lower going to the right and vice versa. Furthermore, by tuning the tunnel

couplings with electrostatic side gates, different detector settings may be used in order to perform, e.g., a Bell test.

We consider the Hamiltonian of the full system

$$\hat{H} = \hat{H}_L + \hat{H}_D + \hat{H}_T + \hat{V}, \tag{3.18}$$

with the Hamiltonians for the leads and the dots, respectively,

$$\hat{H}_L = \sum_{\gamma k} \varepsilon_{\gamma k} \hat{c}^\dagger_{\gamma k} \hat{c}_{\gamma k}, \qquad \hat{H}_D = \sum_{\gamma} \varepsilon_\gamma \hat{d}^\dagger_\gamma \hat{d}_\gamma + \frac{1}{2} \sum_{\gamma\gamma'} U_{\gamma\gamma'} \hat{d}^\dagger_{\gamma'} \hat{d}^\dagger_\gamma \hat{d}_\gamma \hat{d}_{\gamma'}, \tag{3.19}$$

as well as the Hamiltonians for the lead–dot tunneling couplings and the dot–dot tunneling couplings

$$\hat{H}_T = \sum_{\gamma k} t_{\gamma k} \hat{d}^\dagger_\gamma \hat{c}_{\gamma k} + \text{H.c.}, \qquad \hat{V} = \frac{1}{2} \sum_{\gamma\gamma} t_{\gamma\gamma'} \hat{d}^\dagger_\gamma \hat{d}_{\gamma'} + \text{H.c.} \tag{3.20}$$

Here $\hat{c}_{\gamma k}$ and $\hat{d}_\gamma$ are annihilation operators acting on the leads and the dots, respectively. Furthermore, $\varepsilon_{\gamma k}$ denotes single-particle energies of the leads and $t_{\gamma k}$ and $t_{\gamma\gamma'}$ denote the lead–dot and the dot–dot tunneling amplitudes. We note that the total Hamiltonian resembles the one in Eq. (2.11), however, here we have six quantum dots instead of just one, which also means that we have to take into account their mutual interactions.

Under the two-particle resonance condition, and with the the sequential tunneling off resonance, the sequential terms in $\hat{V}$ are eliminated using a Schrieffer–Wolf transformation (see App. B for further details), yielding the cotunneling dynamics in terms of an effective Hamiltonian

$$\hat{H}_{\text{eff}} = \hat{H}_L + \hat{H}_D + \hat{H}_T + \sum_{\alpha\beta} \left(t_{\beta\alpha 21} \hat{d}^\dagger_\beta \hat{d}^\dagger_\alpha \hat{d}_2 \hat{d}_1 + \text{H.c.} \right) \tag{3.21}$$

up to a renormalization of the dot energy levels. Here $\alpha = A+, A-$ and $\beta = B+, B-$ as before. The two-particle tunneling amplitudes $t_{\beta\alpha 21}$ are given by

$$t_{\beta\alpha 21} = \frac{t_{\beta 1} t_{\alpha 2}}{\Delta E_{\beta\alpha}} - \frac{t_{\alpha 1} t_{\beta 2}}{\Delta E_{\alpha\beta}}, \tag{3.22}$$

where $1/\Delta E_{\beta\alpha} = (\varepsilon_1 + \varepsilon_2 + U_{12} - [\varepsilon_2 + \varepsilon_\beta + U_{2\beta}])^{-1} + (\varepsilon_1 + \varepsilon_2 + U_{12} - [\varepsilon_1 + \varepsilon_\alpha + U_{1\alpha}])^{-1}$ at two-particle resonance, and $\Delta E_{\alpha\beta}$ obtained by permuting α and β in the expression for $\Delta E_{\beta\alpha}$. We note that the two-particle tunneling amplitude may be interpreted as the sum of the amplitudes of two different interfering electron paths, with the minus sign stemming from the anti-symmetry property of fermionic wavefunctions.

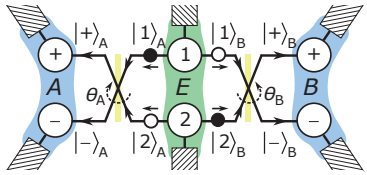

Figure 3.3: The entangler–detector transfer process. Electrons are emitted from the entangler through different "rails", either to the left or to the right. The entangled state emitted from the entangler dots is effectively locally rotated (depending on the tunnel couplings) at both detector systems before the electrons end up in the detector dots. This figure is taken from Paper I.

Emission from the entangler to the detectors

Starting with the initial state vector $|\Psi\rangle_{\rm ini} = \hat{d}_1^\dagger \hat{d}_2^\dagger |0\rangle = |21\rangle$, where the two entangler dots are occupied, we find that the state that leaks out to the detector systems is given by

$$|\Psi\rangle_{\rm dot} = (\hat{H}_{\rm eff} - \hat{H}_0)|\Psi\rangle_{\rm ini} = \sum_{\alpha\beta} t_{\beta\alpha 21} \hat{d}_\beta^\dagger \hat{d}_\alpha^\dagger |0\rangle = \sum_{\alpha\beta} t_{\beta\alpha 21} |\alpha\beta\rangle. \tag{3.23}$$

By parametrizing the tunnel amplitudes as $t_{A+1} = t_{A1}\cos\theta_A$, $t_{A-1} = t_{A1}\cos\theta_A$, etc., with $|t_{A1}|^2 = |t_{A+1}|^2 + |t_{A-1}|^2$, we may write

$$|\Psi\rangle_{\rm dot} = (S_A \otimes S_B)|\Psi\rangle_{\rm emi}, \quad S_i = \begin{pmatrix} \cos\theta_i & \sin\theta_i \\ -\sin\theta_i & \cos\theta_i \end{pmatrix}, \tag{3.24}$$

where the state emitted from the entangler is given by (up to a normalization constant)

$$|\Psi\rangle_{\rm emi} = c_{21}|2\rangle_A|1\rangle_B - c_{12}|1\rangle_A|2\rangle_B, \tag{3.25}$$

with $c_{21} = t_{A2}t_{B1}/\Delta E_{BA}$ and $c_{12} = t_{A1}t_{B2}/\Delta E_{AB}$. We thus conclude that the state $|\Psi\rangle_{\rm dot}$ in the detector dots may be seen as the emitted state $|\Psi\rangle_{\rm emi}$ locally rotated at each detector system, see Fig. 3.3. Most importantly, the emitted state $|\Psi\rangle_{\rm emi}$ is entangled in the orbital degree of freedom, as desired, for any finite values of c_{21} and c_{12}.

So far we have considered an idealized situation, where we start with the entangler dots occupied. However, to rigorously model the dynamics of the open quantum dot systems, we use the Lindblad equation [c.f. Eq. (2.26)]

$$\frac{d\hat{\rho}(t)}{dt} = -\frac{i}{\hbar}[\hat{H}_{\rm eff}, \hat{\rho}(t)] + \sum_\gamma \Gamma_\gamma \Big[\Big(f_\gamma \mathcal{D}_{-\chi_\gamma}[\hat{d}_\gamma^\dagger, \hat{\rho}(t)] + (1-f_\gamma)\mathcal{D}_{\chi_\gamma}[\hat{d}_\gamma, \hat{\rho}(t)] \Big) + \frac{\Gamma_\varphi}{2}\mathcal{D}_0[\hat{d}_\gamma^\dagger d_\gamma, \hat{\rho}(t)] \Big], \tag{3.26}$$

where $\hat{\rho}(t)$ is the reduced density matrix of the quantum dot system, $\mathcal{D}[\hat{L}, \hat{\rho}] = \hat{L}\hat{\rho}\hat{L}^\dagger - \frac{1}{2}\{\hat{L}^\dagger\hat{L}, \hat{\rho}\}$ is the dissipator and f_γ is the Fermi function of lead γ. In the high-bias limit

considered, we have $f_\gamma = 1$ for $\gamma = 1, 2$ (the leads coupled to the entangler dots) and $f_\gamma = 0$ for $\gamma = A\pm, B\pm$ (the leads coupled to the detector dots). The Lindblad equation fully takes into account the transport of particles in and out of the system as well as between the quantum dots. We have also included dephasing, with a rate Γ_φ. We will return to this equation later in the chapter, when we consider the detection of the entangled electrons. But first we consider how to quantify the amount of entanglement contained in a quantum state.

3.4 Entanglement measures

While the definition of entanglement in Sec. 3.2 specifies what entanglement *is*, it does not specify how to *quantify* it. Different entangled states display quantum correlations of various strengths and are of various use for quantum information applications. It is thus desirable to introduce a measure that quantifies the amount of entanglement.

To make sense as a quantification of entanglement, an entanglement measure $E(\hat{\rho})$ should be a function that maps density matrices to real numbers under the following conditions [115]

1. $E(\hat{\rho}) = 0$ for any separable $\hat{\rho}$,
2. $E(\hat{\rho}) > 0$ for any entangled $\hat{\rho}$, and
3. $E(\hat{\rho})$ does not increase on average under LOCC operations.

The last criterion is motivated by the fact that LOCC operations cannot create quantum correlations.

3.4.1 Measures for pure states

For pure bipartite states, any entanglement is fully characterized by the Schmidt coefficients previously introduced. This means that any entanglement measure for pure bipartite states has to be a function of these coefficients. The most common such entanglement measure is the *entropy of entanglement* [116], which is defined as the von Neumann entropy of one of the reduced states

$$E(\hat{\rho}) = S(\mathrm{tr}_A\{\hat{\rho}\}) = S(\mathrm{tr}_B\{\hat{\rho}\}) = -\sum_i \alpha_i^2 \log\left(\alpha_i^2\right), \tag{3.27}$$

where α_i are the Schmidt coefficients. We see from this relation that the more mixed a reduced state of a pure state is, the more entangled is the state. In a sense, entanglement in

this case is about the lack of information of the individual subcomponents of a composite system about which we have full information. For the spin singlet and the other Bell states, the reduced states are maximally mixed and the entropy of entanglement attains its maximal value; these states are maximally entangled.

3.4.2 Measures for mixed states

A disadvantage of the entropy of entanglement is that there is no unique generalization to the mixed states. Instead there are several ways of extending it to the mixed states, including entanglement of formation, distillable entanglement and entanglement cost. These entanglement measures are normally difficult to compute. In this thesis, we therefore instead use another measure, called *concurrence*. Similar to the entropy of entanglement, the concurrence $C_p(\hat{\rho})$ of a pure state $\hat{\rho}$ is defined in terms of the purity of its reduced states $\hat{\rho}_A$

$$C_p(|\Psi\rangle\langle\Psi|) = \sqrt{2(1 - \mathrm{tr}\{\hat{\rho}_A^2\})}. \tag{3.28}$$

This quantity may be easily generalized to all mixed states by a so-called complex roof construction, which means that we define the concurrence as

$$C(\hat{\rho}) = \min_{|\Psi_i\rangle} \sum_i p_i C_p(|\Psi_i\rangle\langle\Psi_i|), \quad \text{with} \quad \hat{\rho} = \sum_i p_i |\Psi_i\rangle\langle\Psi_i|. \tag{3.29}$$

Most importantly, Wootter's formula [117, 118] allows us to easily compute this quantity for a two qubit system as

$$C(\hat{\rho}) = \max(0, \lambda_1 - \lambda_2 - \lambda_3 - \lambda_4), \tag{3.30}$$

where λ_i is the ith eigenvalue (in decreasing order) of $\sqrt{\sqrt{\hat{\rho}}(\sigma_y \otimes \sigma_y)\hat{\rho}^*(\sigma_y \otimes \sigma_y)\sqrt{\hat{\rho}}}$, with * denoting the complex conjugate. We note that the concurrence is equal to 0 for separable states and to 1 for maximally entangled states.

Applying the definition of concurrence on the emitted state in Eq. (3.25), we find

$$C(|\Psi\rangle_{\mathrm{ent}}\langle\Psi|_{\mathrm{ent}}) = 2\frac{|c_{12}| \cdot |c_{21}|}{|c_{12}|^2 + |c_{21}|^2}. \tag{3.31}$$

A maximally entangled state may be generated if $c_{12} = c_{21}$, for which $C(|\Psi\rangle_{\mathrm{ent}}\langle\Psi|_{\mathrm{ent}}) = 1$. We also note that the emitted state is entangled for all $c_{12}, c_{21} \neq 0$. Any concurrence may be generated in the quantum dot system depending on the tunneling amplitudes. Thus, the system constitutes a kind of testbed for producing orbital states with various amount of entanglement.

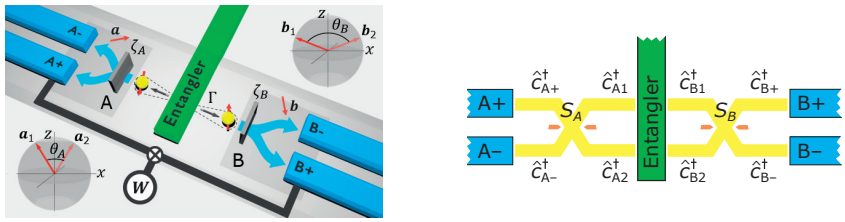

(a) (b)

Figure 3.4: (a) A generic entangler–detector system for bipartite entangled electrons. Entangled electrons (here in the spin degree of freedom) are emitted from an entangler (green) at a rate Γ and separated to two different detector systems A and B. At each detector system the state of each electron is read out, e.g., with ferromagnetic leads. The projection of the state of an electron onto the polarization axes $\mathbf{a}$ and $\mathbf{b}$, respectively, determine the probabilities to end up at the $+$ and $-$ leads. In addition, there is a probability $1-\zeta_{A,B}$ to end up randomly at any lead, independent of the state of the spins, where $0 \leq \zeta_{A,B} \leq 1$ are the detector effiencies. Inset: For two measurements, the detector settings can always be chosen such that the polarization axes are symmetric in the xz plane about the z axis. The result only depends on the local relative angles θ_A and θ_B. This figure is taken from Paper II. (b) The current cross-correlations are related to the annihilation (creation) operators $\hat{c}^{(\dagger)}_{A+}$, $\hat{c}^{(\dagger)}_{A-}$, $\hat{c}^{(\dagger)}_{B+}$, $\hat{c}^{(\dagger)}_{B-}$ at the leads. These are in turn related via scattering theory, described by scattering matrices S_A and S_B, to the annihilation operators (creation operators) at the entangler, $\hat{c}^{(\dagger)}_{A1}$, $\hat{c}^{(\dagger)}_{A2}$, $\hat{c}^{(\dagger)}_{B1}$, $\hat{c}^{(\dagger)}_{B2}$.

3.5 Entanglement detection in nanoscale systems

So far, we have seen how orbitally entangled electrons can be generated in a quantum dot system. We have also seen how the entanglement may be quantified using entanglement measures. However, to actually measure the entanglement experimentally is a completely different story. We here address entanglement detection schemes – schemes aiming at unambiguously verifying that a quantum state is entangled. Inspired by their equivalents in quantum optics, Bell tests [19, 24, 25, 119, 120], full quantum state tomography [121] and entanglement witnesses [31–34] have been proposed for nanoscale systems over the last two decades. However, in contrast to their equivalents in quantum optics, these schemes are typically formulated in terms of current cross-correlations [19, 24, 25, 120, 122], and not single-shot correlation measurements. The main reason is that current detectors normally have a limited bandwidth that does not allow for time-resolved detection of single electrons. That said, recent advances in single-electron detectors [65], for instance based on quantum point contacts [66–68], may eventually open up the possibility of conducting single-shot detection completely analogous to quantum optics experiments. This will be further discussed at the end of this section.

Entanglement detection based on zero-frequency current cross-correlations

To investigate entanglement detection in nanoscale systems, we now consider the generic entangler-detector setup shown in Fig. 3.4. An entangler, whose internal structure is of less importance here, emits electrons, entangled either in the spin or the orbital degrees of freedom, to two spatially separated detector systems, A and B, each consisting of two leads

$+$ and $-$. The system is operated in the high-bias limit, with a large bias applied between the entangler and the detector systems to drive a unidirectional flow of electrons from the entangler to the detector leads, with the temperature effectively set to zero. In general, the emitted state of the entangler is a full many-body state consisting of a superposition of states with different particle numbers, whose effective two-particle density matrix may be probed with cross-correlation measurements [121]. However, here we assume that the entangler is operating in the tunneling regime, with single pairs of electrons emitted well-separated in time at a rate Γ. In that case, the emitted state $\hat{\rho}_{AB}$ is a truly two-particle state.

On their way to the detector leads, each electron of a pair passes through an electronic beam splitter. Using, e.g., electrostatic side gates one may modify the lengths between the entangler and the detector leads, effectively inducing controllable phase shifts. The beam splitters act as local unitary transformations (determining the detector settings) on the emitted state before the electrons end up either at lead $+$ or lead $-$ depending on their spin or orbital state. The aim of this section is to investigate how the entanglement of the emitted state may be probed by measuring low-frequency current cross-correlations between the detector leads.

The zero-frequency current cross-correlators are defined analogous to Eq. (2.54), but with currents of different conductors cross-correlated and ω set to zero, thus yielding

$$S_{AB}^{\alpha\beta} \equiv \frac{1}{2}\int dt \langle\{\Delta\mathcal{J}_{A\alpha}(t), \Delta\mathcal{J}_{B\beta}(0)\}\rangle, \tag{3.32}$$

where $\Delta\mathcal{J}_{A\alpha}(t)$ is the current fluctuation operator at lead $A\alpha$ at time t and $\Delta\mathcal{J}_{B\beta}(0)$ is the current fluctuation operator at lead $B\beta$ at time 0, with $\alpha, \beta = \pm$. The average is taken with respect to the steady-state density matrix describing the continous flow of electrons from the entangler to the detector leads. The cross-correlators may be [121, 123] expressed in terms of the number operators $\hat{n}_A^\alpha = \hat{c}_{A\alpha}^\dagger \hat{c}_{A\alpha}$ and $\hat{n}_B^\alpha = \hat{c}_{B\alpha}^\dagger \hat{c}_{B\alpha}$ for each respective lead as

$$S_{AB}^{\alpha\beta} = 2e^2\Gamma\left[\langle \hat{n}_A^\alpha \hat{n}_B^\beta\rangle - \langle \hat{n}_A^\alpha\rangle\langle \hat{n}_B^\beta\rangle\right]. \tag{3.33}$$

Importantly, in the tunneling regime where the second term is negligible, we see that a zero-frequency cross-correlation measurement naturally produces an ensemble average over many realizations of single emissions from the entangler.

Using scattering theory, we may go "backwards" in the system and relate, via the electronic beam splitters, the creation/annihilation operators at the detector leads to the creation/annihilation operators of the degrees of freedom of the emitted state. In general, the beam splitter at the A side may be described by the following scattering matrix

$$\begin{pmatrix} \hat{c}_{A+} \\ \hat{c}_{A-} \end{pmatrix} = S_A \begin{pmatrix} \hat{c}_{A1} \\ \hat{c}_{A2} \end{pmatrix}, \quad S_A = \begin{pmatrix} \sqrt{R_A} e^{i\varphi_{A2}} & \sqrt{T_A} e^{i(\varphi_{A3}-\phi_A)} \\ \sqrt{T_A} e^{i(\varphi_{A1}+\varphi_{A2})} & -\sqrt{R_A} e^{i(\varphi_{A1}+\varphi_{A3}-\phi_A)} \end{pmatrix}, \tag{3.34}$$

where R_A is the reflection coefficient, $T_A = 1 - R_A$ is the transmission coefficient, $\varphi_{A\gamma}$, $\gamma_1 = 1, 2, 3$, are uncontrollable (but for one and the same measurement fixed) phases and ϕ_A is the phase shift induced by, e.g., an electrostatic side gate. An analogous relation holds for the beam splitter at the B side. Using these relations, we may, in the tunneling limit, rewrite Eq. (3.33) as

$$S_{AB}^{\alpha\beta} = 2e^2\Gamma \mathrm{tr}\left(\mathcal{A}^\alpha \otimes \mathcal{B}^\beta \hat{\rho}_{AB}\right) \tag{3.35}$$

where $\hat{\rho}_{AB}$ still denotes the emitted state and

$$\mathcal{A}^\pm = \frac{1}{2}\left(\mathbf{I} \pm \mathbf{a}\cdot\boldsymbol{\sigma}\right) \qquad \text{and} \qquad \mathcal{B}^\pm = \frac{1}{2}\left(\mathbf{I} \pm \mathbf{b}\cdot\boldsymbol{\sigma}\right), \tag{3.36}$$

with $\mathbf{a}$ and $\mathbf{b}$ the polarization unit vectors of each detector system parametrizing the beam splitters, $\mathbf{I}$ the identity operator and $\boldsymbol{\sigma}$ the Pauli vector. We have thus obtained a relation between the zero-frequency current cross-correlators and the emitted state of the entangler.

Non-ideal detectors

So far, we have assumed that the scattering process is perfect and neglected the influence of the environment on the emitted state during its transfer from the entangler to the detector leads. This influence may be modeled as polarization channels acting on each electron, $\mathcal{E}_A \mathrm{tr}_B\{\hat{\rho}_{AB}\} = \zeta_A \mathrm{tr}_B\{\hat{\rho}_{AB}\} + (1-\zeta_A)\frac{\mathbf{I}}{2}$ for the A side and similar for the B side. The effect on the whole two-particle density matrix is

$$\mathcal{E}(\hat{\rho}_{AB}) = (\mathcal{E}_A \otimes \mathcal{E}_B)\hat{\rho}_{AB}, \tag{3.37}$$

where $\zeta_{A,B} = p_{A,B}(1-\eta_{A,B})$ [124] are the effective detector efficiencies, with $0 \leq p_{A,B} \leq 1$ the polarization of detector system A, B and $\eta_{A,B}$ the spin-flip rate on the way from the entangler to detector system A, B. Using the relation $\mathrm{tr}\{\mathcal{A}^\pm \otimes \mathcal{B}^\pm \mathcal{E}(\hat{\rho}_{AB})\} = \mathrm{tr}\{\mathcal{E}_A(\mathcal{A}^\pm) \otimes \mathcal{E}_B(\mathcal{B}^\pm)\hat{\rho}_{AB}\}$ [32, 124], we obtain

$$S_{AB}^{\pm\pm} = \frac{e^2\Gamma}{2}\mathrm{tr}\left\{(\mathbf{I} \pm \zeta_A \mathbf{a}\cdot\boldsymbol{\sigma}) \otimes (\mathbf{I} \pm \zeta_B \mathbf{b}\cdot\boldsymbol{\sigma})\hat{\rho}_{AB}\right\}, \tag{3.38}$$

in the case of non-ideal detector efficiencies. As expected, we see that for $\zeta_A = \zeta_B = 0$, we do not obtain any information about $\hat{\rho}_{AB}$ from the zero-frequency current cross-correlations.

3.5.1 Bell test

Dating back to the original EPR paradox and the debate on violations of local realism, Bell tests are the most conventional way of detecting entanglement. The aim of such a test is

to violate a Bell inequality, derived from the condition that local realism has to hold, and thereby demonstrating the presence of entanglement. We focus on the CHSH inequality previously introduced in Sec. 3.1 [see Eq. (3.4)]

$$\mathcal{B} = |E(\mathbf{a},\mathbf{b}) + E(\mathbf{a},\mathbf{b}') - E(\mathbf{a}',\mathbf{b}) + E(\mathbf{a}',\mathbf{b}')| \leq 2, \tag{3.39}$$

where $\mathcal{B}$ is the so-called Bell parameter. Here $E(\mathbf{a},\mathbf{b}) \equiv \langle \hat{\sigma}_{\mathbf{a}} \otimes \hat{\sigma}_{\mathbf{b}} \rangle$ are the correlation functions for the measurement outcomes at detector system A and B for various detector settings $\mathbf{a}$ and $\mathbf{b}$. If a combination of two pairs of settings $\mathbf{a}$, $\mathbf{b}$ and $\mathbf{a}'$, $\mathbf{b}'$ are found to lead to a violation of Eq. (3.39), the measured state must be entangled. However, as previously mentioned, the opposite is not true; there are entangled states that are not violating any Bell inequality.

Using the expression in Eq. (3.38), we may express the correlation functions for the Bell test as

$$E(\mathbf{a},\mathbf{b}) = \frac{S_{AB}^{++} - S_{AB}^{+-} - S_{AB}^{-+} + S_{AB}^{--}}{S_{AB}^{++} + S_{AB}^{+-} + S_{AB}^{-+} + S_{AB}^{--}}, \tag{3.40}$$

where we have assumed ideal detectors, $\zeta_A = \zeta_B = 1$. Here we note that the correlation functions may be obtained from the zero-frequency current cross-correlations. However, we may also note that for each correlation function we need four different current cross-correlation measurements, thus 16 in total for a complete Bell test.

Bell test for orbital entanglement in a quantum dot system

We now demonstrate how to extract the zero-frequency current cross-correlations from the quantum dot system discussed in Paper I and use them to formulate a Bell inequality. To this end, we first introduce counting fields χ_γ that couple to the net particle current to each lead γ, yielding the counting-field resolved Lindblad equation [c.f. Eq. (3.26)]

$$\frac{d\hat{\rho}(t)}{dt} = -\frac{i}{\hbar}[\hat{H}_{\text{eff}}, \hat{\rho}(t)] + \sum_\gamma \Gamma_\gamma \Big[\Big(f_\gamma \mathcal{D}_{-\chi_\gamma}[\hat{d}_\gamma^\dagger, \hat{\rho}(t)] + (1-f_\gamma)\mathcal{D}_{\chi_\gamma}[\hat{d}_\gamma, \hat{\rho}(t)] \Big) + \frac{\Gamma_\varphi}{2}\mathcal{D}_0[\hat{d}_\gamma^\dagger d_\gamma, \hat{\rho}(t)] \Big], \tag{3.41}$$

where $\mathcal{D}_\chi[\hat{L},\hat{\rho}] = e^{i\chi}\hat{L}\hat{\rho}\hat{L}^\dagger - \frac{1}{2}\{\hat{L}^\dagger\hat{L},\hat{\rho}\}$ is the counting-field resolved dissipator.

Using Eq. (2.44), we obtain the cumulant generating function of the long-time statistics from Eq. (3.41) by extracting the eigenvalue that goes to zero when the zero counting fields go to zero

$$F_\chi = \sum_{\alpha\beta} (e^{i(\chi_\alpha + \chi_\beta - \chi_1 - \chi_2)} - 1) P_{\alpha\beta} \tag{3.42}$$

to leading order in the tunneling amplitudes. Here $\alpha = A+, A-$ and $\beta = B+, B-$ as before. The transfer rates are given by

$$P_{\alpha\beta} = \frac{|t_{\beta\alpha 21}|^2(\Gamma_\alpha + \Gamma_\beta + \Gamma_\varphi)}{\frac{\hbar^2}{4}(\Gamma_\alpha + \Gamma_\beta + \Gamma_\varphi)^2 + \varepsilon_{12\alpha\beta}^2}, \tag{3.43}$$

with the energy difference $\varepsilon_{12\alpha\beta} \equiv \varepsilon_\alpha + \varepsilon_\beta + U_{\alpha\beta} - (\varepsilon_1 + \varepsilon_2 + U_{12})$ from two-particle resonance. The expression in Eq. (3.42) corresponds to four different cotunneling processes, where the two electrons in the entangler dots are transferred to the four different combinations of detector dots. Each transfer process is Poissonian and takes place at a rate set by $P_{\alpha\beta}$. $P_{\alpha\beta}$ may be interpreted as the (unnormalized) joint detection probabilities of having one electron transferred to dot α and another to dot β.

Most importantly, these quantities may be extracted from zero-frequency current cross-correlations. This can be seen by calculating the cross-correlations as derivatives of (3.42) with respect to different counting fields, yielding

$$S_{\alpha\beta} = e^2 P_{\alpha\beta} = e^2 \frac{\partial^2 F_\chi}{\partial(i\chi_\alpha)\partial(i\chi_\beta)}\bigg|_{\chi_\alpha=\chi_\beta=0}. \tag{3.44}$$

From this expression, we can also obtain the correlation function in Eq. (3.40), where we set $\zeta_A = \zeta_B = 1$ since all charge transfer events are assumed to be perfectly detected for the quantum dot setup.

We recall that the detector settings are determined by the tunneling couplings between the entangler and the detector dots. By tuning them, with electrostatic side gates, one may choose different settings to perform a Bell test. However, this tuning must be made in such a way that the emitted state [see Eq. (3.25)] is not altered. To this end, we assume that the tuning of the tunneling may be parametrized with an angle θ_A as

$$\begin{aligned} t_{A+1} &= t_{A1}\cos\theta_A, \qquad & t_{A-2} &= t_{A2}\cos\theta_A \\ t_{A-1} &= t_{A1}\sin\theta_A, \qquad & t_{A+2} &= -t_{A2}\sin\theta_A, \end{aligned} \tag{3.45}$$

where $t_{A1}^2 = t_{A+1}^2 + t_{A-1}^2$ is the total probability for an electron in the upper entangler dot to tunnel to detector system A and $t_{A2}^2 = t_{A+2}^2 + t_{A-2}^2$ is the corresponding probability for an electron in the lower entangler dot. A similar parametrization is assumed to hold at detector system B. Under this rotation of the tunneling rates, for which $|t_{A+1}/t_{A-1}| = |t_{A-2}/t_{A+2}|$ and $|t_{B+1}/t_{B-1}| = |t_{B-2}/t_{B+2}|$, the emitted state is the same. More specifically, the coefficients defining the emitted state in Eq. (3.25) are given by $c_{12} \propto t_{A1}t_{B2}$ and $c_{21} \propto t_{A2}t_{B1}$ [see Eq. (3.25)].

Inserting these parametrizations in Eq. (3.43) and using Eq. (3.39), we obtain the maximal value of the Bell parameter that one can obtain for the emitted state

$$\mathcal{B}_{\max} = 2\sqrt{1 + \sin^2\theta}, \tag{3.46}$$

where $\theta = 2\arctan(c_{12}/c_{21})$, $-\pi \leq \theta \leq \pi$. This value of the Bell parameter is clearly larger than 2 unless c_{12} or c_{21} is zero. This demonstrates that the inequality in Eq. (3.39) can be violated – at least in principle – whenever the emitted state is entangled. We have thus showed how the emitted state can be detected using zero-frequency current cross-correlations. That said, it is still experimentally highly challenging to perform a Bell test. The main reason is that the tuning of the tunneling couplings have to be made in a very controllable way. In reality, the control of the tunneling couplings may be very limited and it can be challenging to tune, e.g., one of the couplings without affecting the others. One would therefore instead like to use a detection scheme based on a smaller set of settings and measurements, such as entanglement witnesses.

3.5.2 Entanglement witnesses

Although the above calculations show that a Bell test may – at least in principle – be performed in our quantum dot system, realizing such a test still remains a big hurdle to overcome. As already pointed out, a Bell test requires 16 different cross-correlation measurements, in four different bases. Both for the tunneling couplings used in the quantum dot system as well as for other nanoscale detection schemes, such as those based on ferromagnetic leads for spin entanglement detection, it is challenging to fully control the detector settings. This makes it difficult in practice to realize all the right settings that are needed for a Bell test. It is therefore desirable to use alternative detection schemes where the required number of measurements, in particular the number of settings, can be reduced.

One such kind of detection schemes is based on entanglement witnesses [95, 125], which are the main objects of Paper II. The idea behind witnesses is to use *any* observable which is capable of distinguishing entangled states from the separable ones to detect entanglement. More precisely, if an observable, for at least one entangled state, produces an expectation value that no separable state can yield, it can be used as a witness for that entangled state. Mathematically, we define a witness operator $\mathcal{W}$ as any operator fulfilling

$$\langle \mathcal{W} \rangle = \mathrm{tr}\{\mathcal{W}\hat{\rho}\} > \max_{\hat{\rho}_s} \mathrm{tr}\{\mathcal{W}\hat{\rho}_s\} \quad \text{or} \quad \langle \mathcal{W} \rangle = \mathrm{tr}\{\mathcal{W}\hat{\rho}\} < \min_{\hat{\rho}_s} \mathrm{tr}\{\mathcal{W}\hat{\rho}_s\} \tag{3.47}$$

for at least one entangled state $\hat{\rho}$, where the minimization/maximization is performed over all separable states $\hat{\rho}_s$. The first condition we call the "upper limit condition" and the second condition the "lower limit condition". In the literature, these conditions are often renormalized to

$$\mathrm{tr}\{\mathcal{W}\hat{\rho}\} < 0 \quad \text{and} \quad \mathrm{tr}\{\mathcal{W}\hat{\rho}_s\} \geq 0 \quad \forall \hat{\rho}_s. \tag{3.48}$$

However, here we will focus on the actual experimentally measured quantities and thus stick to the conditions in Eq. (3.47).

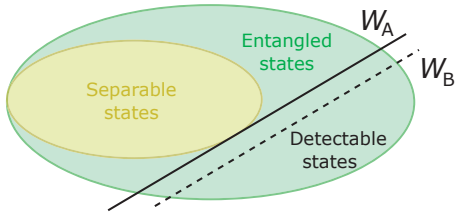

Figure 3.5: The set of all states (density matrices) is convex. This set is made up of the convex subset of separable states (yellow) and the non-convex subset of entangled states (green). An entanglement witness may be represented as a hyperplane, separating the entangled states that are detectable from the separable states. Here $\mathcal{W}_A$ is a witness superior to the non-optimal $\mathcal{W}_B$.

We note that the Bell parameter in Eq. (3.39) itself may be seen as a witness. It detects all entangled states that yield a larger value than $\mathcal{B} = 2$. Entanglement witnesses are thus a more general class of detection schemes than the Bell tests. Another example of a witness is $\mathcal{W} = \sigma_x \otimes \sigma_x + \sigma_y \otimes \sigma_y$. The great benefit of entanglement witnesses compared to Bell tests is indeed their generality. First, in contrast to Bell inequalities, there is a witness for every entangled state [95] that can detect it. This fact is illustrated in Fig. 3.5; for every entangled state there is a witness, represented by a hyperplane, that separates it from the convex set of separable states. Second, witnesses allows for detection schemes that require much fewer measurements [126–128] than conventional Bell tests. This holds true even for multipartite entanglement [129].

Minimal entanglement witnesses based on zero-frequency cross-correlations

We now address how entanglement witnesses can be used to minimize the number of zero-frequency current cross-correlations needed to detect entanglement, the topic of Paper II. In previous works, entanglement witnesses have been formulated in terms of zero-frequency cross-correlations with the aim of decreasing the number of measurements needed to witness entanglement in solid-state systems [31–34]. Here we will present the idea behind Paper II, that is, how to find the *minimal* number of measurements needed to detect entanglement.

Based on Eq. (3.35), we start by writing down an expression for an observable corresponding to an arbitrary number N current cross-correlations (up to uninmportant prefactor of $\frac{e^2\Gamma}{2}$) between lead $A+$ and lead $B+$

$$\mathcal{W} = \sum_{i=1}^{N} (1 + \zeta_A \mathbf{a}_i \cdot \boldsymbol{\sigma}) \otimes (1 + \zeta_B \mathbf{b}_i \cdot \boldsymbol{\sigma}). \tag{3.49}$$

Here $\mathbf{a}_i$ and $\mathbf{b}_i$ denote the polarization vectors used as the ith measurement setting at detector A and B, respectively. We are assuming that the detector efficiencies ζ_A and ζ_B are the same throughout one and the same experiment. The work of Paper II focuses on

investigating what the smallest possible number N is that makes $\mathcal{W}$ a witness and what entangled states are detectable for that N.

Witness conditions

To be a witness, the operator in Eq. (3.49) needs to fulfill the condition in Eq. (3.47) for at least one entangled state $\hat{\rho}$. First, we note that for $N = 1$, $\mathcal{W}$ is just a tensor product of local operators. The expectation value of such an operator can always be mimicked by a separable state. Thus, as expected, it is not possible to detect any entangled states with just one single measurement.

However, we will now show that for $N = 2$, $\mathcal{W}$ works as a witness. To see this, we first reformulate the witness conditions in Eq. (3.47). To have a witness the largest/smallest possible expectation value has to be produced only by entangled states. At the same time, the largest/smallest expectation value is obtained from the eigenstates of $\mathcal{W}$. Thus, the witness condition implies that the eigenstates with the largest/smallest eigenvalues have to be entangled. In addition, the eigenvalues must be nondegenerate since one may otherwise construct a separable state out of a linear combination of the two entangled degenerate eigenstates that also maximizes/minimizes the expectation value. The witness condition is therefore equivalent to having eigenstates with the largest/smallest eigenvalues that are (i) entangled and (ii) unique.

To investigate these conditions, we first note that the expectation value $\mathrm{tr}\{\mathcal{W}\hat{\rho}\}$ as well as the amount of entanglement of the state $\hat{\rho}$ are invariant under local unitary transformations. This means that, without loss of generality, we may consider a coordinate system where the polarization vectors at each detector system lie symmetric about the z axis in the xz-plane. The angle between the polarization vectors for the two different settings is denoted by θ_A and θ_B, respectively. The witness conditions then boil down to conditions only on these angles and the efficiencies ζ_A and ζ_B. To investigate condition (i), we use an eigenvalue decomposition of $\mathcal{W}$, yielding the eigenstates with the largest and the smallest eigenvalues

$$\begin{aligned} |\psi_1\rangle &= \sin\alpha|{+}{+}\rangle - \cos\alpha|{-}{-}\rangle, \\ |\psi_4\rangle &= \cos\alpha|{+}{+}\rangle + \sin\alpha|{-}{-}\rangle, \end{aligned} \tag{3.50}$$

in the local $\{|++\rangle, |+-\rangle, |-+\rangle, |--\rangle\}$-basis with the angle $0 \leq \alpha \leq \pi/4$ obtained from

$$\tan\alpha = \left(\sqrt{(c_A + c_B)^2 + s_A^2 s_B^2} - (c_A + c_B)\right)/s_A s_B. \tag{3.51}$$

Here we have introduced $c_\alpha = \zeta_\alpha \cos(\theta_\alpha/2)$, $s_\alpha = \zeta_\alpha \sin(\theta_\alpha/2)$, $\alpha = A, B$, with $\cos(\theta_A) = \mathbf{a}_1 \cdot \mathbf{a}_2$ and $\cos(\theta_B) = \mathbf{b}_1 \cdot \mathbf{b}_2$. Importantly, both $|\psi_1\rangle$ and $|\psi_4\rangle$ are entangled for all $\alpha \neq 0$, i.e., for all detector parameters except $\theta_A = 0$, $\theta_B = 0$, $\zeta_A = 0$ or $\zeta_B = 0$, for which $W^{(2)}$ can be written as a product of local operators.

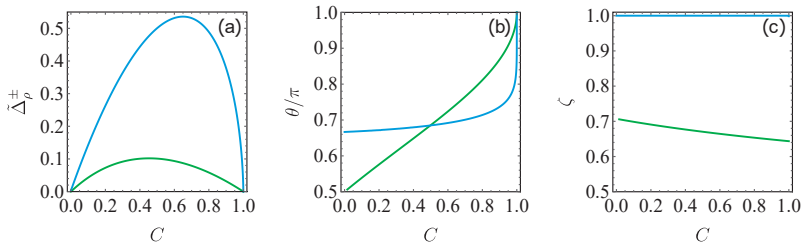

Figure 3.6: Left panel: The maximal detection margin as a function of the concurrence C of an entangled pure state for a symmetric setup, $\zeta = \zeta_A = \zeta_B$ and $\theta = \theta_A = \theta_B$. The blue curve corresponds to the upper limit condition and the green curve corresponds to the lower limit condition. Right panels: The optimal detector settings ζ and θ as a function of C.

To investigate condition (ii), we consider the corresponding eigenvalues

$$\lambda_i = 2\left(1 \pm c_A c_B \pm \sqrt{(c_A \pm c_B)^2 + s_A^2 s_B^2}\right), \tag{3.52}$$

where the indices $i = 1, 2, 3, 4$ correspond to an order of $\pm$ as $\{+-+\}$,$\{---\}$,$\{-++-\}$,$\{+++\}$, with $\lambda_1 \leq \lambda_2 \leq \lambda_3 \leq \lambda_4$. We here see that both eigenvalues λ_1, λ_4 are non-degenerate for all detector parameters, except $\theta_A = \pi$, $\theta_B = \pi$, $\zeta_A = 0$ or $\zeta_B = 0$, for which $\lambda_1 = \lambda_2$ and $\lambda_3 = \lambda_4$ due to local rotation symmetries of the polarization vectors, and $\zeta_A = \zeta_B = 1$ for which $\lambda_1 = \lambda_2$ due to a hidden, non-local symmetry [130, 131].

We thus conclude that for $N = 2$, we have a witness for all finite detector efficiencies ($\zeta_A, \zeta_B > 0$) and non-collinear polarization vectors ($\theta_A, \theta_B \neq 0, \pi$). This is one of the main findings of Paper II. This result shows that our minimal entanglement witness allows us to significantly reduce the number of required settings to detect entangled states compared to a conventional Bell test.

Detectable states

Interestingly, the results in the previous subsection also answers what entangled pure states are detectable since every entangled pure state may, under local unitary transformations, be turned into an eigenstate of the form in Eq. (3.50) for some α. This means that any pure state may maximize/minimize the expectation value of $\mathcal{W}$ for some detector setting. Only for the maximally entangled states, for which $\alpha = 1$, $\mathcal{W}$ is not a witness. In all other cases, $\mathcal{W}$ works as a witness that can detect the entangled pure state.

For the singlet state $\hat{\rho}^*$, we have $2(1 - \zeta_A\zeta_B) \leq \mathrm{tr}\{\mathcal{W}\hat{\rho}^*\} \leq 2(1 + \zeta_A\zeta_B)$, while for separable states $\hat{\rho}_s$, $\min_{\hat{\rho}_s} \mathrm{tr}\{\mathcal{W}\hat{\rho}_s\} \leq 2(1 - \zeta_A\zeta_B)$ and $\max_{\hat{\rho}_s} \mathrm{tr}\{\mathcal{W}\hat{\rho}_s\} \geq 2(1 + \zeta_A\zeta_B)$. In other words, the expectation value of the singlet state can always be reproduced by a separable state. Since the singlet state is equivalent to all maximally entangled states under the local unitary transformations, we conclude that none of them are detectable. We thus

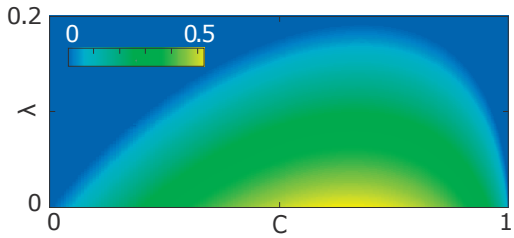

Figure 3.7: The detection margins for a symmetric setup with $\theta \equiv \theta_A = \theta_B$ and $\zeta \equiv \zeta_A = \zeta_B$ for mixed states of the form $\hat{\rho} = (1-\lambda)|\Psi\rangle\langle\Psi| + \lambda\mathbf{I}/4$, $0 \leq \lambda \leq 1$, with $|\Psi\rangle$ state with concurrence $0 \leq C \leq 1$. This figure is taken from Paper II.

conclude that all entangled pure states are detectable, except the maximally entangled. The maximally entangled can, however, be detected with three measurements, which is still much better than the 16 measurements required in a Bell test.

For a real experiment it is not only interesting to know which states can be detected, but also how large the detection margin is. The detection margin is defined as the difference between the expectation value of $\mathcal{W}$ with respect to a certain entangled state and the closest expectation value obtained for any separable state

$$\begin{aligned} \Delta_\rho^{W+} &\equiv \mathrm{tr}(W^{(N)}\rho) - \max_{\rho_s} \mathrm{tr}(W^{(N)}\rho_s), \\ \Delta_\rho^{W-} &\equiv \min_{\rho_s} \mathrm{tr}(W^{(N)}\rho_s) - \mathrm{tr}(W^{(N)}\rho). \end{aligned} \tag{3.53}$$

Focusing on symmetric setups, we find the optimal settings shown in Fig. 3.6 as a function of the concurrence of the pure state. As expected, we see that both separable ($C = 0$) and maximally entangled states ($C = 1$) are undetectable, while all non-maximally entangled states give finite detection margins. Interestingly, the hidden, non-local symmetry discussed before makes non-ideal detectors better than ideal detectors for the lower limit condition.

Furthermore, we investigate which mixed states may be detected with just two measurements. We find the maximal detection margin for mixed states of the form

$$\hat{\rho} = \lambda\mathbf{I}/4 + (1-\lambda)|\Psi\rangle\langle\Psi|, \tag{3.54}$$

shown in Fig. 3.7. We see there that some noise may be tolerated, but that the detection margin decreases with increasing noise level and eventually becomes zero.

3.5.3 Short time detection

We end this section by considering a short-time detection based on the second-order degree of coherence. Motivated by the advances in single-electron detectors [65–68], there is a growing interest for performing a short-time formulation of a Bell inequality in solid-state

systems, corresponding to the single-shot measurements in quantum optics. In Paper I, we investigate how to formulate a Bell inequality in terms of the cross-correlated second-order degree of coherence, which is defined as

$$g^{(2)}_{\alpha\beta}(\tau) = \frac{\langle\langle \mathcal{J}_\alpha e^{\mathcal{L}_0\tau}\mathcal{J}_\beta\rangle\rangle + \langle\langle \mathcal{J}_\beta e^{\mathcal{L}_0\tau}\mathcal{J}_\alpha\rangle\rangle}{2\langle\langle \mathcal{J}_\alpha\rangle\rangle\langle\langle \mathcal{J}_\beta\rangle\rangle}, \tag{3.55}$$

similar to the ordinary $g^{(2)}(\tau)$ function in Ch. 2. For the quantum dot system in Paper I, we find

$$g^{(2)}_{\alpha\beta}(\tau) = P_{\alpha\beta}\frac{\Gamma_\alpha\Gamma_\beta}{\Gamma_\alpha+\Gamma_\beta}\frac{e^2}{2I_\alpha I_\beta}(e^{-\Gamma_\alpha\tau}+e^{-\Gamma_\beta\tau}), \tag{3.56}$$

to leading order in the cotunneling amplitudes. We see here that $P_{\alpha\beta}$ may be extracted directly from this quantity if we know the tunneling rates Γ_α, Γ_β and the currents I_α and I_β. We note that this expression is only valid for $\tau \ll 1/\Gamma_\alpha$ and $\tau \ll 1/\Gamma_\beta$; terms of order unity are neglected.

Importantly, the zero-frequency current cross-correlators may also be obtained since

$$S_{\alpha\beta} = e^2 P_{\alpha\beta} = 2I_\alpha I_\beta \int_0^\infty d\tau g^{(2)}_{\alpha\beta}(\tau). \tag{3.57}$$

Short-time detection in terms of $g^{(2)}(\tau)$ functions is thus equivalent to the zero-frequency current cross-correlation measurements. In both cases, we may extract the (unnormalized) joint detection probabilities $P_{\alpha\beta}$.

3.6 Summary and outlook

In this chapter, we have introduced some of the most peculiar features of quantum mechanics: entanglement and quantum correlations. These concepts constitute key ingredients for many applications in the field of quantum information and quantum computing. Much of this chapter has thus focused on how to generate and detect entangled states in a controllable way. For instance, we have seen how the quantum dot system in Paper I allows us to generate and detect orbitally entangled electrons on a sub-decoherence time scale. This is possible by taking advantage of cotunneling processes that take place on a time scale much faster than the decoherence time. The quantum correlations displayed by entangled states may be detected from zero-frequency current cross-correlation measurements. One of the advantages of such measurements is that they do not require detectors with wide bandwidths that can resolve single-electron events.

While most proposals for entanglement detection in nanoscale systems so far are based on zero-frequency cross-correlation measurements, new technological advances in single-electron detection methods pave the way to single-shot coincidence measurements of individual electrons. The setup in Paper I would be very suitable for such an experiment,

completely analogous to the ones in quantum optics, since the tunnel rates to the leads can be made arbitrarily weak. The mean time between tunneling events may then be long enough to allow for today's single-electron detectors, with a bandwidth in the sub-MHz range, to detect the electrons.

As shown in the last section of this chapter, entanglement witnesses provide a way of substantially reducing the number of measurements needed to detect entanglement. In Paper II, we show that the number of measurements may be reduced from the 16 of a Bell test to just two or three. Surprisingly, the maximally entangled states require three measurements. However, it is not clear if the use of nonlinear entanglement witnesses could reduce this number to two. In any case, two or three measurements is still much better than 16. It reduces the experimental effort needed to detect entangled electrons significantly and can hopefully contribute to making entanglement detection in solid-state system experimentally more feasible.

Chapter 4

Quantum thermodynamics

In this chapter, we introduce the second main topic of this thesis: quantum thermodynamics or, more specifically, heat transport and temperature fluctuations in nanoscale systems.

Classical thermodynamics, dealing with energy, heat and work in large systems close to equilibrium, was largely developed during the 19th and the beginning of 20th century. Based on often fascinatingly simple arguments, this theory typically describes complex systems, consisting of an enormously large amount of degrees of freedom, with only a very few parameters like temperature, volume and pressure. Despite this, or maybe because of this, thermodynamics has been a surprisingly successful theory, laying the theoretical foundation for everything from daily-life applications such as heat engines and refrigerators to fundamental concepts such as black-body radiation and thermal states.

However, when going to smaller systems, such as nanoscale systems, fluctuations play an increasingly important role. It is not obvious that a thermodynamical treatment, based on statistical arguments, of such small systems with one or only a few particles would be possible. Only during the last decades, with the advent of the Jarzynski equality [36, 37] and the Crooks fluctuation theorem [38], it was realized that thermodynamics may also be applied to these systems, leading to the development of stochastic and quantum thermodynamics. In the latter case, the influence of quantum effects may also be investigated. However, despite a great amount of research recently, heat transport in nanoscale systems is still much less explored than, e.g., charge transport, mainly owing to the lack of a thermal counterpart to the ammeter.

Here, in this chapter, we will introduce some of the basic tools to describe and investigate heat transport. We start by considering heat transport in nanoscale systems in terms of long-time statistics (Sec. 4.1). We will consider the same example system as in Ch. 2 to exemplify important concepts. Then we introduce the single electron box (Sec. 4.2) and

present an overview of the main findings of Paper III, in particular how to extract the temperature statistics and its relation to the heat transfer statistics. After that, we consider the main topic of this chapter, namely quantum calorimetry in a metallic island coupled to a superconducting injector (Sec. 4.4) with the aim to detect heat. We end the chapter with a summary and outlook (Sec. 4.5).

4.1 Heat transport in nanoscale systems

Just as in classical thermodynamics, heat constitutes, together with work, one of the most important concepts in quantum thermodynamics. According to the first law of thermodynamics, a closed system (i.e., a system which does not exchange mass with its environment) may change its energy only through heat and work. Work is energy added through a change of the macroscopic degrees of freedom that may be controlled externally, e.g., by an applied bias or a volume change. Work may be described by a Hamiltonian that depends explicitly on these macroscopic degrees of freedom, or implicitly through a time dependence. By contrast, heat is energy added through the microscopic degrees of freedom that are usually not accessible externally (by an experimentalist), for instance the motion of single particles. The difference between heat and work for a quantum system is most clearly illustrated by considering an infinitesimal change dE of the expectation value of the Hamiltonian $\hat{H}(t)$ [132]

$$dE \equiv d\mathrm{tr}\left\{\hat{H}(t)\hat{\rho}(t)\right\} = \mathrm{tr}\left\{d\hat{H}(t)\hat{\rho}(t)\right\} + \mathrm{tr}\left\{\hat{H}(t)d\hat{\rho}(t)\right\} \equiv dW + dQ, \tag{4.1}$$

where $\hat{\rho}(t)$ is the reduced density matrix of the system. Here we see that an energy change dE may be caused either by a change in the Hamiltonian (corresponding to the infinitesimal work dW described by the first term) or by a change in the density matrix (corresponding to the infinitesimal heat dQ described by the second term). For a closed system whose time evolution is described by the Liouville–von Neumann equation, the last term drops out as there is no heat exchange with the environment. However, the second term may become important for systems whose time evolution is described by master equations. Notably, for systems exchanging particles, the second term may also contain a work contribution μdN, where μ is the chemical potential and dN is an infinitesimal change in the particle number. If the Hamiltonian of the system is time-independent, this results in the heat expression

$$dQ = dE - \mu dN. \tag{4.2}$$

Much of this chapter will focus on heat transport and its connection to temperature fluctuations in nanoscale systems. In this section, we introduce the basic concepts to describe heat transport statistically using the tools from Ch. 2. Heat transport is of vital importance

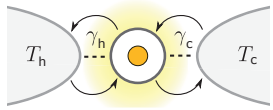

Figure 4.1: A single resonance level coupled, with coupling strenghts γ_c and γ_h, to two reservoirs, one with temperature T_c and the other with temperature T_h. The occupation numbers of the reservoirs are $\bar{n}_{c,h} = (\exp[\varepsilon/(k_B T_{c,h})] \pm 1)^{-1}$.

for our following discussion on temperature fluctuations and quantum calorimetry. To exemplify all concepts, we again consider the example system introduced in Ch. 2. However, to make this system somewhat more interesting, we now consider a single resonance level coupled to *two* reservoirs, one hot with occupation number $\bar{n}_h$ and one cold with occupation number $\bar{n}_c$, see Fig. 4.1. For simplicity, in the fermionic case, we assume that there is no voltage bias applied between the reservoirs. We consider the net heat transferred from the system to the cold reservoir, but all concepts may equally well be used to describe the net heat transfer to the hot reservoir. In the bosonic case, this allows us to present some of the key findings of the second part of Paper V.

4.1.1 Master equation approach

To extract the heat transfer statistics for a certain system, we proceed in the same way as we did in Ch. 2 to obtain the particle emission statistics. The main difference is that we now use a counting field s that couples to the transfer of *heat* instead of particles. Introducing the density matrices $\hat{\rho}(E,t)$ describing the system state provided that a certain amount of heat E has been transferred to the cold reservoir during a measurement time t, we obtain the following energy-resolved master equation

$$\frac{d\hat{\rho}(E,t)}{dt} = (\mathcal{L} - \mathcal{J}_a - \mathcal{J}_e)\hat{\rho}(E,t) + \mathcal{J}_e\hat{\rho}(E+\varepsilon,t) + \mathcal{J}_a\hat{\rho}(E-\varepsilon,t), \tag{4.3}$$

where $\mathcal{J}_a\hat{\rho}(t) = \gamma_c\bar{n}_c\hat{a}^\dagger\hat{\rho}(t)\hat{a}$ is the absorption current superoperator and $\mathcal{J}_e\hat{\rho}(t) = \gamma_c(1 \pm \bar{n}_c)\hat{a}\hat{\rho}(t)\hat{a}^\dagger$ is the emission current superoperator for adding and subtracting, respectively, an amount of energy ε in the system from/to the cold reservoir. The Lindbladian superoperator $\mathcal{L}$ is, as before, obtained from Eq. (2.33).

Employing a Laplace transformation, $\hat{\rho}(s,t) = \int dE\hat{\rho}(E,t)e^{Es}$, we obtain the counting-field resolved master equation, which in the fermionic case of our example system is

$$\frac{d}{dt}\begin{pmatrix} P_0(s,t) \\ P_1(s,t) \end{pmatrix} = \begin{pmatrix} -\gamma_c\bar{n}_c - \gamma_h\bar{n}_h & \gamma_c(1-\bar{n}_c)e^{\varepsilon s} + \gamma_h(1-\bar{n}_h) \\ \gamma_c\bar{n}_c e^{-\varepsilon s} + \gamma_h\bar{n}_h & -\gamma_c(1-\bar{n}_c) - \gamma_h(1-\bar{n}_h) \end{pmatrix}\begin{pmatrix} P_0(s,t) \\ P_1(s,t) \end{pmatrix}, \tag{4.4}$$

where $P_0(s,t) = \langle 0|\hat{\rho}(s,t)|0\rangle$ and $P_1(s,t) = \langle 1|\hat{\rho}(s,t)|1\rangle$ are the populations of the counting-field resolved density matrix. In the bosonic case, the system dimension is infinite and the matrix representation of the master equation becomes infinitely large, see

Paper V for further details. However, due to the weak coupling limit, where only one particle is exchanged with the environment at a time, this matrix representation has a simplified tridiagonal structure.

4.1.2 Long time statistics

To characterize the heat current statistics, we extract the long-time cumulant generating function. This is done completely analogous to the procedure described in Ch. 2 for emission currents, i.e., from the eigenvalue of the counting-field resolved Lindbladian that goes to zero when the corresponding counting field goes to zero. This yields

$$\frac{F(s,t)}{t} = \frac{\gamma_c+\gamma_h}{2}\left(\mp 1 \pm \sqrt{1 \pm 4\frac{\gamma_c\gamma_h}{(\gamma_c+\gamma_h)^2}\kappa(s)}\right), \tag{4.5}$$

where $\kappa(s) = (e^{\varepsilon s}-1)(1\mp\bar{n}_c)\bar{n}_h + (e^{-\varepsilon s}-1)\bar{n}_c(1\mp\bar{n}_h)$.

From the CGF we obtain all the cumulants that describe the heat transfer statistics. For instance, the average heat current is

$$\overline{J_E} = \frac{1}{t}\langle\langle E\rangle\rangle = \frac{1}{t}\frac{\partial F(s,t)}{\partial s}\bigg|_{s=0} = \varepsilon\frac{\gamma_c\gamma_h}{\gamma_c+\gamma_h}(n_h-n_c). \tag{4.6}$$

We see that the average heat current depends on the difference in the occupation numbers; if the difference goes to zero the net heat current goes to zero as well. The expression in Eq. (4.6) may be understood as a number of particles n_h and n_c being transferred at a rate $\frac{\gamma_c\gamma_h}{\gamma_c+\gamma_h}$ in each direction, with each particle carrying an amount ε of heat. Interestingly, in terms of the occupation numbers, this expression is identical for both bosons and fermions.

The zero-frequency noise, on the other hand, does depend on the particle statistics, as shown by

$$\begin{aligned} S_{J_E}(0) &= \frac{1}{t}\langle\langle E^2\rangle\rangle = \frac{1}{t}\frac{\partial^2 F(s,t)}{\partial s^2}\bigg|_{s=0} \\ &= \varepsilon^2\frac{\gamma_c\gamma_h}{\gamma_c+\gamma_h}\left(\bar{n}_c(1\mp\bar{n}_h)+\bar{n}_h(1\mp\bar{n}_c)\mp 2(\bar{n}_h-\bar{n}_c)^2\frac{\gamma_c\gamma_h}{(\gamma_c+\gamma_h)^2}\right). \end{aligned} \tag{4.7}$$

One may easily consider higher-order cumulants by considering higher-order derivatives of the CGF.

4.1.3 Thermal conductance

The thermal conductance κ is the analog quantity of electrical conductance for describing how well a junction sustains a heat current. Characterizing the linear response to a

temperature gradient, it is defined [133] as the amount of average heat $\overline{J_E}$ flowing through the junction per unit time when an infinitesimal temperature bias ΔT is applied over the junction

$$\kappa = -\lim_{\Delta T \to 0} \frac{\overline{J_E}}{\Delta T}. \tag{4.8}$$

The thermal conductance is typically temperature dependent. For instance, for our example system, we obtain

$$\kappa = \left.\frac{d\overline{J_E}}{dT_h}\right|_{T \equiv T_h = T_c} = \frac{\varepsilon^2}{k_B T^2} \frac{\gamma_c \gamma_h}{\gamma_c + \gamma_h} \bar{n}(1 \mp \bar{n}), \tag{4.9}$$

where we clearly see the manifestation of the Pauli principle in the fermionic case as a blocking factor $\bar{n}(1 - \bar{n})$. Here $\bar{n} \equiv \bar{n}_h = \bar{n}_c$ is the equilibrium occupation number. The thermal conductance is suppressed at low temperatures for both bosons or fermions. At high temperatures, the conductance increases and reaches a maximum for both bosons (for which $\bar{n} \to \infty$) and fermions (for which $\bar{n} \to 1/2$).

For metals, the thermal conductance at temperature T is typically linked to the electrical conductance G via the Wiedemann–Franz law [134]

$$\kappa = \mathcal{L}_0 G T, \tag{4.10}$$

with the Lorenz number $\mathcal{L}_0 = \frac{\pi^2}{3}\frac{k^2}{e^2}$. As a side remark, we note that for thermoelectrical applications it is desirable to reach a as high ratio of GT/κ as possible to obtain a high value of the figure of merit, $ZT = S^2 GT/\kappa$, with S the thermopower. With the Wiedemann–Franz law setting a fixed value for this ratio, much research has focused on violating this relationship between the thermal and the electrical conductance [135–143]. Such violations typically occur where interactions are present that cause the single-particle theory to fail.

Here our interest in the thermal conductance instead lies in its crucial role for the relation between heat and temperature fluctuations. As we will see later in this chapter, a high thermal conductance to the environment suppresses temperature fluctuations as any excess energy is more quickly dissipated to the environment.

4.1.4 Fluctuation–dissipation theorem

So far, we have seen several different ways of characterizing heat transport, for instance in terms of average heat currents, zero-frequency noise and thermal conductances. While the average current does not contain any information about the particle statistics, both the zero-frequency noise and the thermal conductance do. Quite surprisingly, the two latter quantities are interlinked. This is the essence of the fluctuation–dissipation theorem [144,

145], which relates fluctuations in equilibrium to the linear response to a small perturbation. The theorem states that

$$S_{J_E} = 2k_B T^2 \kappa, \tag{4.11}$$

which is also what we find by comparing Eqs. (4.7) and (4.9) for our example system.

Besides providing a deeper physical understanding for the relation between fluctuations and dissipation, the fluctuation–dissipation theorem allows us to obtain the thermal conductance from the noise, and vice versa.

4.1.5 Fluctuation relation

While the fluctuation–dissipation theorem provides us with the noise at equilibrium, it says nothing about fluctuations far from equilibrium. However, even fluctuations arbitrarily far away equilibrium do obey certain relations, as illustrated by the Crooks fluctuation relation [38]. These fluctuation relations may be obtained directly from a symmetry property of our CGF. Using that $e^{-\sigma/\varepsilon}(1 \mp \bar{n}_c)\bar{n}_h = (1 \mp \bar{n}_h)\bar{n}_c$, we find

$$F(-s - \Delta\beta, t) = F(s, t), \qquad \Delta\beta = (\beta_c - \beta_h), \tag{4.12}$$

which, by transforming back to the probability distributions, results in the fluctuation relation

$$\frac{1}{t} \ln \left[\frac{P(J_E, t)}{P(-J_E, t)} \right] = \Delta\beta J_E. \tag{4.13}$$

Here we stress that J_E is the average heat current measured over a long time t. The fluctuation relation describes the probability $P(J_E, t)$ of having a certain J_E over a time t relative to the probability of having the same average current flowing in the opposite direction. This relation is governed by the entropy production rate $\Delta\beta J_E$ associated with the heat current J_E. The more entropy production associated with a certain current, the less likely it runs in the opposite ("wrong") direction.

From the fluctuation relation, we may derive other important results, such as the second law of thermodynamics for the average entropy production over a long time t

$$\begin{aligned} \langle S \rangle_t &\equiv \int_{-\infty}^{\infty} dS S P(S, t) = t\Delta\beta \int_{-\infty}^{\infty} dJ_E J_E P(J_E, t) \\ &= t\Delta\beta \int_{0}^{\infty} dJ_E J_E P(J_E, t)(1 - e^{-S}) \geq 0, \end{aligned} \tag{4.14}$$

where $P(S, t) = \frac{dJ_E}{dS} P(J_E, t)$ is the probability that an amount of entropy $S = t\Delta\beta J_E$ is produced over a time t. In the third step, we have made use of the fluctuation relation from Eq. (4.13).

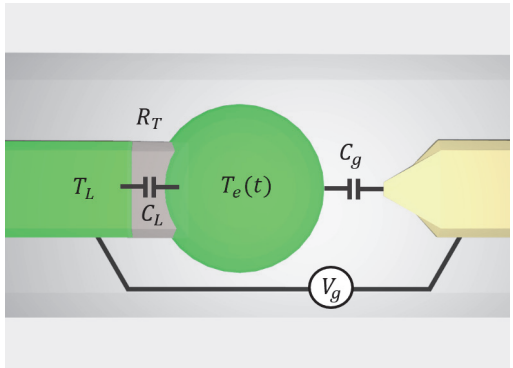

Figure 4.2: The single electron box consisting of a metallic island (green, circle) with a quasi-temperature $T_e(t)$ tunnel-coupled (gray connection) to a normal metallic lead (green, rectangular) with a tunnel resistance R_T and a capacitance C_L. The island is also coupled to a gate (yellow) with capacitance C_g and an applied bias V_g.

4.2 Single electron box

We now consider the system discussed in Paper III and summerize some of the main findings of that paper. The aim of the paper is to investigate heat transport in a somewhat more complicated system than our example system – the so-called single electron box – where charging effects are present. In particular, we want to investigate the temperature fluctuations induced as heat is transferred back and forth between the system and its environment. This forms the basis for our later discussions on quantum calorimetry.

We first describe the system itself. The single electron box consists of a small metallic island coupled, via a tunnel junction with resistance $R_T \gg \frac{h}{e^2}$, to a normal metallic lead with a fixed temperature T_L. The island contains an electron gas of about 10^8 electrons with a very short internal thermalization time τ_{e-e}, typically of the order of a few nanoseconds or less [40]. The thermalization process normally takes place on a time scale much faster than all other relevant processes, allowing us to describe the electron gas by a Fermi–Dirac distribution with an effective temperature $T_e(t)$ at any instant of time on these time scales.

In contrast to our example system, the Fermi wavelength in the single electron box is typically less than a nanometer [146] and thus much shorter than the dimensions of the island. Quantization effects are therefore negligible. However, single-particle effects may still be relevant due to charging effects if the unit of charging energy $E_c \equiv \frac{e^2}{2C_{\text{tot}}}$ exceeds other energy scales, such as the thermal energies $k_B T_L$ and $k_B T_e(t)$ as well as the potential energy eV_g. Here $C_{\text{tot}} = C_L + C_g$ is the total capacitance to the environment, with C_L the capacitance to the lead and C_g the capacitance to an electrostatic gate that has a fixed potential V_g. The charging energy of the island is then given by $E_c(n) = E_c(n - n_g)^2$, where n is the number of excess electrons on the island and $n_g = V_g C_g$ is the gate-induced charge on the island. The change in the charging energy when an electron is added is

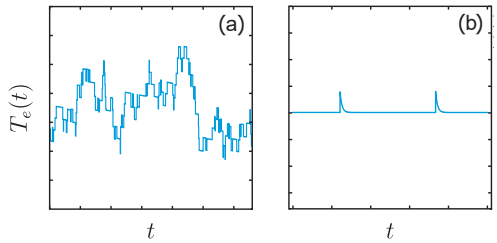

Figure 4.3: Monte Carlo simulations of the temperature fluctuations in a single electron box for (a) a much higher injection rate than the electron–phonon relaxation rate ($1/\tau_E \gg 1/\tau_{e-ph}$) and (b) a much smaller injection rate than the electron–phonon relaxation rate ($1/\tau_E \ll 1/\tau_{e-ph}$), under ideal conditions (very low temperatures) for which phonon-induced fluctuations are negligible.

$\Delta = E_c(1) - E_c(0) = E_c(1 - 2n_g)$. We assume that E_c is large and that the gate is tuned so that only zero or one excess electrons may occupy the island, thus motivating the name "single electron box".

Time scales

When electrons tunnel back and forth between the island and the lead, the energy of the island changes, which induces fluctuations in its temperature. The dynamics of these fluctuations depend on three important time scales. First, the internal thermalization time τ_{e-e} – the time it takes for the system to redistribute excess heat within the island to form a new Fermi–Dirac distribution. As already mentioned, this time scale is only a few nanoseconds or even shorter, which normally makes it the shorterst time scale. This is a precondition for us to assign an effective temperature $T_e(t)$ to the electron gas at any instant of time on the time scales for the interactions with the environment. The second time scale is the electron–phonon thermalization time τ_{e-ph}, i.e., the time scale on which the electron gas equilibrates with phonons in the system. The phonons are assumed to have a fixed bath temperature T_b. The third time scale is the typical time τ_E between subsequent tunnel events between the island and the lead.

At low temperatures, the electron–phonon coupling becomes very weak and the electrons are effectively decoupled from the phonons. This allows us to consider the regime where $\tau_E \ll \tau_{e-ph}$, where the metallic island does not have time to equilibrate with the phonons in between subsequent tunneling events. The temperature of the metallic island may then deviate substantially from the phonon bath temperature and develop a build-up of larger fluctuations [see Fig. 4.3 (a)] that may act back on the tunneling rates. In this regime, the effect of the phonons may be completely neglected.

In the opposite limit, with a very low tunneling rate relative to the electron–phonon thermalization time, $\tau_E \gg \tau_{e-ph}$, $T_e(t)$ will equilibrate with the phonon bath in between subsequent tunneling events, as shown in Fig. 4.3 (b). This regime will be further discussed

when we consider quantum calorimetry. For now, we focus on the regime where the phonons are effectively decoupled from the electrons.

4.2.1 Heat transport fluctuations

Before going into the statistics of temperature fluctuations in the single electron box, we consider the heat transport statistics. The weak coupling between the metallic island and the connected lead allows us to employ a master equation. We assume that a high charging energy prevents more than one excess electron from occupying the island. Analogous to our treatment of heat transport in the example system, we use a Pauli master equation to describe the time evolution of the probabilities to have an unoccupied or an occupied island. One important difference is that an electron may now transfer various energies in a finite interval, and not only one single energy. We introduce a counting field ξ that couples to the net heat transferred between the lead and the island, and obtain the master equation

$$\frac{d}{dt}\begin{pmatrix} P_0(\xi,t) \\ P_1(\xi,t) \end{pmatrix} = \begin{pmatrix} -\Gamma_{\text{in}}(0) & \Gamma_{\text{out}}(\xi) \\ \Gamma_{\text{in}}(\xi) & -\Gamma_{\text{out}}(0) \end{pmatrix} \begin{pmatrix} P_0(\xi,t) \\ P_1(\xi,t) \end{pmatrix}. \tag{4.15}$$

Here $P_0(\xi,t)$ and $P_1(\xi,t)$ are the counting field-resolved probabilities of having zero and one electron, respectively. The rates are given by

$$\Gamma_{\text{in}}(\xi) = \frac{1}{e^2 R_T}\int dE\,[1-f(E,T_e)]f(E+\Delta,T_L)e^{i\xi E} \tag{4.16}$$

$$\Gamma_{\text{out}}(\xi) = \frac{1}{e^2 R_T}\int dE f(E,T_e)\,[1-f(E+\Delta,T_L)]\,e^{-i\xi E}, \tag{4.17}$$

where the absorption and emission of energies in a continous range are taken into account. For brevity, we introduce $\Gamma_{\text{in}} \equiv \Gamma_{\text{in}}(0)$ and $\Gamma_{\text{out}} \equiv \Gamma_{\text{out}}(0)$.

From the eigenvalues of Eq. (4.15), we obtain the cumulant generating function (CGF) for the long-time statistics

$$\frac{F(\xi,t)}{t} = \frac{1}{2}\left(\sqrt{(\Gamma_{\text{in}}-\Gamma_{\text{out}})^2 + 4\Gamma_{\text{in}}(\xi)\Gamma_{\text{out}}(\xi)} - \Gamma_{\text{in}} - \Gamma_{\text{out}}\right). \tag{4.18}$$

Note that $F(0,t)=0$ as required from the normalization of the CGF. Introducing $\Gamma_{\text{in}}^{(n)} \equiv \frac{\partial^n \Gamma_{\text{in}}(\xi)}{\partial(i\xi)^n}\Big|_{\xi=0}$ and $\Gamma_{\text{out}}^{(n)} \equiv \frac{\partial^n \Gamma_{\text{out}}(\xi)}{\partial(-i\xi)^n}\Big|_{\xi=0}$, we may express the first two cumulants as

$$\begin{aligned} \overline{J_E} &= \frac{\langle E\rangle}{t} = \frac{\Gamma_{\text{out}}^{(0)}\Gamma_{\text{in}}^{(1)} - \Gamma_{\text{in}}^{(0)}\Gamma_{\text{out}}^{(1)}}{\Gamma_{\text{out}}^{(0)} + \Gamma_{\text{in}}^{(0)}} \\ S_{J_E}(0) &= \frac{\langle\langle E^2\rangle\rangle}{t} = \frac{\Gamma_{\text{in}}^{(2)}\Gamma_{\text{out}}^{(0)} + \Gamma_{\text{in}}^{(0)}\Gamma_{\text{out}}^{(2)} - 2\Gamma_{\text{in}}^{(1)}\Gamma_{\text{out}}^{(1)}}{\Gamma_{\text{in}}^{(0)} + \Gamma_{\text{out}}^{(0)}} - 2\frac{\left(\Gamma_{\text{out}}^{(0)}\Gamma_{\text{in}}^{(1)} - \Gamma_{\text{in}}^{(0)}\Gamma_{\text{out}}^{(1)}\right)^2}{\left(\Gamma_{\text{in}}^{(0)} + \Gamma_{\text{out}}^{(0)}\right)^3} \end{aligned} \tag{4.19}$$

To get a deeper understanding for these results, we consider an equilibrium situation where $T_e = T_L$.

Equilibrium statistics

For equal temperatures, $T_e = T_L$, we find the analytic expressions

$$\Gamma_{\text{in}}(\xi) = \frac{1}{e^2 R_T} \frac{\Delta}{e^{\Delta/(k_B T_L)} - 1} h(\xi), \quad \Gamma_{\text{out}}(\xi) = \frac{1}{e^2 R_T} \frac{\Delta}{e^{\Delta/(k_B T_L)} - 1} e^{\Delta/(k_B T_L)} h(-\xi) \tag{4.20}$$

with

$$h(\xi) = e^{-i\xi\Delta/2} \frac{2\pi k_B T_L \sin(\xi\Delta/2)}{\Delta \sinh(\pi k_B T_L \xi)}. \tag{4.21}$$

The cumulant generating function then becomes

$$\frac{F(\lambda, t)}{t} = -\frac{k_B T_L}{e^2 R_T} \frac{\alpha}{\sinh \alpha} \left[\cosh \alpha - \sqrt{\sinh^2 \alpha + \left(\frac{\pi \sin(\lambda\alpha)}{\alpha \sinh(\pi\lambda)} \right)^2} \right] \tag{4.22}$$

where $\alpha = \Delta/(2k_B T_L)$ and $\lambda = \xi k_B T_L$. This CGF is no longer periodic in the counting field as a result of the non-quantization of the transferred energy. The expression may be seen as a composition of the statistics of the number of particles transferred, and the amount of energy carried by each particle. To see this, we decompose the CGF into

$$F(\lambda, t) = G(\chi(\lambda), t), \tag{4.23}$$

where

$$G(\chi, t)/t = -\frac{k_B T_L}{e^2 R_T} \frac{\alpha}{\sinh \alpha} \left[\cosh \alpha - \sqrt{\sinh^2 \alpha + e^{i\chi}} \right] \tag{4.24}$$

describes the statistical distribution of the number of particles transferred over a time t and

$$\begin{aligned} e^{i\chi(\lambda)} &= \left(\int dE e^{i\lambda E/(k_B T_L)} p(E) \right) \left(\int dE e^{-i\lambda E/(k_B T_L)} p(E) \right) \\ &= h(\lambda) h(-\lambda) = \left(\frac{\pi \sin(\lambda\alpha)}{\alpha \sinh(\pi\lambda)} \right)^2 \end{aligned} \tag{4.25}$$

describes the statistical distribution of the energies transferred by an electron during a single in-and-out tunneling event.

Importantly, we have $F(\lambda, t) = F(-\lambda, t)$, i.e., the probability distribution is symmetric around $J_E = 0$ and we obtain the trivial fluctuation relation

$$\ln \left[\frac{P(J_E, t)}{P(-J_E, t)} \right] = 0, \tag{4.26}$$

as expected for an equilibrium setup (no entropy production). Furthermore, we find

$$\overline{J_E} = 0, \tag{4.27}$$

i.e., there is on average no net heat transport between the island and the lead if they have the same temperatures. In fact, all odd cumulants are zero (since the CGF is an even function of λ). By contrast, the zero-frequency noise is obtained as

$$S_{J_E}(0) = \frac{(k_B T_L)^2}{t} \frac{d^2 F(\lambda, t)}{d(i\lambda)^2}\bigg|_{\lambda=0} = \frac{2(k_B T_L)^3}{3e^2 R_T} \frac{\alpha(\pi^2 + \alpha^2)}{\sinh(2\alpha)}. \tag{4.28}$$

Here we see that the noise gets exponentially suppressed for large α. Furthermore, up to a factor $(k_B T_L)^2$, the noise expression is given by the average number of events $\frac{dG(\chi,t)}{d(i\chi)}\Big|_{\chi=0} = t\frac{k_B T_L \alpha}{e^2 R_T \sinh(2\alpha)}$ during a measurement time t times the noise $\frac{d^2\chi(\lambda)}{d(i\lambda)^2}\Big|_{\lambda=0} = \frac{2(\alpha^2+\pi^2)}{3}$ in the transferred energy of a single in-and-out tunneling event. The suppression of the noise for large α thus arises as a result of the average number of events decreasing faster than the the noise of the transferred energy of a single in-and-out tunneling event increases.

4.2.2 Temperature fluctuations

As energy is transferred back and forth, the temperature of the system will also change. If a small amount of energy is added, the change of the temperature [147] is

$$\Delta T = \frac{\Delta E}{C}, \qquad C = \frac{\pi^2}{3} k_B^2 T_e \nu_F, \tag{4.29}$$

where we have used the expression for the heat capacity of a non-interacting electron gas with ν_F the density of states at the Fermi level. What makes it challenging to describe the induced temperature fluctuations is the feedback effect that arises as a temperature change acts back on the tunneling rates. When the temperature changes, the distribution of the injected energies also changes, resulting in a negative feedback loop that suppresses large deviations from the average temperature.

To derive the temperature statistics, we employ a stochastic path integral. To this end, we first consider a small time interval τ during which the temperature is approximately kept constant. The probability that the energy is changed by small amount $E_{10} = E_1 - E_0$ may be expressed as

$$P(E_{10}) = \frac{1}{2\pi} \int d\xi_0 e^{-i\xi_0(E_1 - E_0) + \tau F(\xi_0, E_0)}. \tag{4.30}$$

If we now consider subsequent time intervals of equal lengths, the probability that the energy is changed by certain values E_{10}, E_{21} etc. is obtained from

$$\begin{aligned} P(E_{10})P(E_{21})...P(E_{NN-1}) &= \frac{1}{(2\pi)^N}\int ... \int d\xi_0...d\xi_{N-1} \\ &\times \exp\left(\sum_{n=0}^{N-1}\left[-i\xi_n(E_{n+1}-E_n)+\tau F(\xi_n,E_n)\right]\right). \end{aligned} \tag{4.31}$$

The probability of transferring an energy E_N over the total time interval $N\tau$ is obtained by integrating over all intermediate energy changes

$$P(E_N) = \int ... \int dE_1...dE_{N-1}P(E_{10})...P(E_{NN-1}). \tag{4.32}$$

The corresponding probability that the temperature follows a certain time trace is

$$\begin{aligned} P_N(T_0,...,T_{N-1}) &= \int ... \int dE_1...dE_{N_1}P(E_{10})...P(E_{NN-1}) \\ &\times \Pi_{n=0}^{N-1}\delta(T_n-\mathcal{T}(E_n)). \end{aligned} \tag{4.33}$$

We then find

$$P_N(T_0,...,T_{N-1}) = \frac{1}{(2\pi)^N}\int ... \int d\zeta_0...d\zeta_{N-1}e^{-i\sum_{n=0}^{N-1}\tau\zeta_nT_n+S_N(\zeta_0,...,\zeta_{N-1})} \tag{4.34}$$

with

$$\begin{aligned} e^{S_N(\zeta_0,...,\zeta_{N-1})} &= \frac{1}{(2\pi)^N)}\int ... \int dE_0...dE_{N-1}d\xi_0...d\xi_{N_1} \\ &\times \exp\left(\sum_{n=0}^{N-1}\left[-i\xi_n(E_{n+1}-E_n)+\tau F(\xi_n,E_n)+i\tau\zeta_n\mathcal{T}(E_n)\right]\right). \end{aligned} \tag{4.35}$$

Taking the continuum limit, we obtain

$$e^{S[\zeta(t)]} = \int\int \mathcal{D}E(t)\mathcal{D}\xi(t)\exp(H[\xi,E]), \tag{4.36}$$

where

$$H[\xi,E] = \int_0^t dt'\left(-i\xi(t')\frac{dE(t')}{dt'}+F[\xi(t'),E(t')]+i\zeta(t')\mathcal{T}(t')\right). \tag{4.37}$$

Here $\mathcal{D}E(t)$ and $\mathcal{D}\xi(t)$ denote different paths in energy and counting field spaces. Equation (4.36) is one of the main findings of Paper III. It allows us to obtain the full temperature statistics from the heat transfer statistics. However, in reality the stochastic path integral is complicated to evaluate. In the long-time limit, however, we may employ the saddle-point approximation to obtain the solution.

Long time limit – Saddle-point solution

In the limit of a long measurement time, we may evaluate Eq. (4.36) using the saddle-point approximation [58]. This yields

$$S[\zeta(t)] = H[\xi^*(t), E^*(t)], \tag{4.38}$$

where $\xi^*(t)$ and $E^*(t)$ are saddle-point solutions to the saddle-point equations

$$\delta H[\xi, E]/\delta\xi = 0, \qquad \delta H[\xi, E]/\delta E = 0. \tag{4.39}$$

These may be written as [with $\mathcal{T}^* = \mathcal{T}(E^*)$]

$$2iC_e(\mathcal{T}^*)\frac{d\mathcal{T}^*(t)}{dt} = \frac{\partial F(\xi^*(t), \mathcal{T}^*(t))}{\partial \xi^*(t)}, \tag{4.40a}$$

$$-2iC_e(\mathcal{T}^*)\frac{d\xi^*(t)}{dt} = \frac{\partial F(\xi^*(t), \mathcal{T}^*(t))}{\partial \mathcal{T}^*(t)} + i\zeta(t) \tag{4.40b}$$

where $C_e(\mathcal{T}^*) \equiv \nu_F \pi^2 k_B^2 \mathcal{T}^*(t)/3$ is the heat capacity of the electron gas at temperature $\mathcal{T}^*$.

Using response theory, these saddle-point equations may be solved perturbatively in $\zeta(t)$, see Paper III for further details. We find

$$\langle T_e(t)\rangle = -i\frac{\delta S[\zeta]}{\delta\zeta(t)}\bigg|_{\zeta(t)=0} = T_L, \tag{4.41a}$$

$$\langle\langle T_e(t)T_e(t')\rangle\rangle = -\frac{\delta^2 S[\zeta]}{\delta\zeta(t)\delta\zeta(t')}\bigg|_{\zeta(t)=0} = \frac{F_{\xi\xi}}{2\kappa^2\tau_C}e^{-|t-t'|/\tau_C}, \tag{4.41b}$$

with the zero-frequency noise $F_{\xi\xi} = \frac{1}{t}\frac{\partial^2 F(\xi,t)}{\partial(i\xi)^2}\Big|_{\xi=0,\,T_e=T_L} = 2k_B\kappa T_L^2$ and the thermal conductance $\kappa = \frac{1}{t}\frac{\partial^2 F(\xi,t)}{\partial(i\xi)\partial T_e}\Big|_{\xi=0,\,T_e=T_L}$. This is another main finding of Paper III.

The results shown in Eqs. (4.41a) and (4.41b) are worth some commenting. The first equation confirms, as expected, that the average temperature of the electron gas is equal to the temperature T_L of the lead. The 2-point correlation function also shows that the correlations between two temperature measurements are decaying exponentially over time, with a correlation time set by $\tau_C = C/\kappa$.

The instantaneous noise is

$$\langle\langle T_e(t)^2\rangle\rangle = \frac{F_{\xi\xi}}{2\kappa^2\tau_C} = \frac{k_B T_L^2}{C}, \tag{4.42}$$

while the long-time noise, the zero-frequency noise, is

$$S_T = \int_{-\infty}^{\infty} dt \langle\langle T_e(t)\, T_e(0) \rangle\rangle = \frac{F_{\xi\xi}}{\kappa^2} = \frac{2k_B T_L^2}{\kappa}. \tag{4.43}$$

Comparing Eqs. (4.42) and (4.43), we see that for short times, the noise is determined by the internal properties of the system (the heat capacity), while for long times, the noise is determined by the coupling of the system to its environment (the thermal conductance).

We note that higher-order cumulants may also be obtained. For instance, the third low-frequency cumulant is given by

$$S_T^{(3)} = \frac{F_{\xi\xi\xi}}{\kappa^3} + \frac{1}{\kappa F_{\xi\xi}} \frac{d}{dT_e} \left(\frac{F_{\xi\xi}(T_e)}{\kappa(T_e)} \right)^3 \Bigg|_{T_e = T_b}. \tag{4.44}$$

where $F_{\xi\xi\xi} = \frac{1}{t} \frac{\partial^3 F(\xi,t)}{\partial (i\xi)^3} \Big|_{\xi=0, T_e = T_L}$, $F_{\xi\xi}(T_e) \equiv \frac{1}{t} \frac{\partial^2 F(\xi,t)}{\partial (i\xi)^2} \Big|_{\xi=0}$ and $\kappa(T_e) = \frac{1}{t} \frac{\partial^2 F(\xi,t)}{\partial (i\xi) \partial T_e} \Big|_{\xi=0}$. Here we see that the temperature distribution may be skewed either as a result of a skewed heat transfer distribution and/or a temperature dependence of $F_{\xi\xi}(T_e)/\kappa(T_e)$, i.e., fluctuations above and below the average value are suppressed differently. For the single electron box, the first effect is zero since all odd cumulants of the heat transfer statistics are zero.

In summary, we have in this section seen how the statistics of the temperature fluctuations may be related to the heat transfer statistics. The temperature statistics may be interested by itself, but it is also of interest for quantum calorimetry as a tool to infer the heat deposited in an absorber, in this case the metallic island.

4.3 Thermometry

To actually be able to detect the fluctuations discussed in the previous section we need a device that is sensitive to temperature. This is what we normally call a thermometer. Over the last few decades, several different methods have been developed for nanoscale thermometry [41], including NIS and SIS thermometers, proximity-effect thermometry, Coulomb blockade thermometers (CBT) and shot-noise thermometers (SNT). Much of the research on nanoscale thermometry has been motivated by the prospects of developing single-microwave photon detectors [69–73] as well as to study heat transport between electrons and phonons [42, 148]. In general, any quantity which depends on the temperature may be used for thermometry, however, it should also allow for high-speed and sensitivite read out and be experimentally feasible to implement, with as little self-heating of the probed system as possible. An important measure of the sensitivity of a thermometer is the noise-equivalent temperature (NET), which is a measure of the input temperature

signal needed to match the internal temperature noise of the thermometer to yield a unit signal-to-noise ratio. The smaller NET, the more sensitive is the thermometer. Usually any temperature dependent current through some kind of junction, e.g., a NIS junction [42], a NIN junction [149, 150] or a SNS junction [151], may be used. Other alternatives include quantum dots [148, 152, 153] and shot noise thermometry [154, 155]. Below we give a brief overview of two of these thermometers: the NIS thermometer and a new method based on the zero-bias anomaly of a superconducting junction [43].

4.3.1 NIS thermometry

A NIS thermometer is based on the temperature dependence of a current running through a normal metal–insulator–superconductor (NIS) junction. The quasi-particle current through such a junction is given by [41, 156]

$$I = \frac{1}{eR_T}\int dE\nu_S(E-eV)[f(E-eV,T_s)-f(E,T_e)], \tag{4.45}$$

where R_T is the tunnel resistance of the junction, $\nu_S(E)$ is the normalized density of states of the superconductor and $f(E,T) = (\exp[E/(k_BT)]+1)^{-1}$ is the Fermi function, with T_e the temperature of the normal metal and T_s the temperature of the superconductor. Ideally, the normalized density of states is given by $\nu_S(E) = \frac{|E|}{\sqrt{|E|^2-\Delta^2}}\theta(|E|-\Delta)$, where $\theta(|E|-\Delta)$ is the Heaviside step function suppressing the number of states within the superconducting gap Δ. In reality, impurities and other imperfections may lead to the presence of sub-gap states, which can be modelled as $\nu_S(E) = \mathrm{Re}\left[\frac{E+i\gamma}{\sqrt{(E+i\gamma)^2-\Delta^2}}\right]$, where γ is the so-called Dynes parameter [157–160] measuring the number of in-gap states.

Most importantly, the quasi-particle current is strongly depending on T_e, while the dependence on T_s is negligible, at least for temperatures far below the critical temperature of the superconductor, where Δ takes on its zero-temperature value. In that case, for small bias, we have

$$I \approx \frac{\sqrt{2\pi k_B T_e \Delta}}{2eR_T} e^{-(\Delta-eV)/(k_BT_e)}. \tag{4.46}$$

The strong dependence on T_e, in contrast to a NIN junction, makes the NIS thermometer an appealing choice for nanoscale thermometry. In addition, its sensing element can be made very small, which allows for local temperature probing. The superconducting gap suppresses heat conduction, thus limiting self-heating. NIS thermometry has the ability to go all the way down to 1 mK [42]. Such low temperatures may be achieved with a dilution refrigerator [161, 162]. By embedding the thermometer in a LC resonant circuit, it is possible to achieve fast and ultrasensitive thermometry [163–165], with read out times on sub-microsecond time scales. The sensitivity may reach well below a noise-equivalent

temperature 100 μK/$\sqrt{\text{Hz}}$ [165]. As with all superconductor-based thermometers, one of the drawbacks with a NIS thermometer is the high sensitivity to external magnetic fields. Another drawback may be possible deviations in a real setup from the ideal model used above and that self-heating is not completely negligible.

4.3.2 Zero-bias anomaly thermometry

A new kind of nanoscale thermometer based on the zero-bias anomaly (ZBA) in a Josephson junction was recently developed [43]. Similar to a conventional NIS thermometer, this thermometer operates with a superconductor tunnel-coupled to a normal conducting metal. However, in this case, another, clean contacted superconductor is attached to the normal conductor, such that the normal metallic region is proximized. The thermometry is based on the probing of the zero-bias anomaly of the $\mathcal{P}$IS junction, where $\mathcal{P}$ stands for the proximized normal metal. The ZBA thermometer is dissipationless and sensitive also at very low temperatures. It allows for sensitive temperature measurements down to 25 mK and even below.

4.4 Quantum calorimetry

We now consider the main subject of this chapter – quantum calorimetry. The idea behind quantum calorimetry is to infer the amount of heat transferred by a single particle by measuring the resulting temperature change induced in an absorber where the energy is deposited. A generic calorimeter consists of an absorber, which is coupled to a thermometer as well as to some kind of injector. The injector emits particles that deposit their energy in the absorber.

Focusing on the nanoscale calorimeter proposed in Paper IV, we here consider calorimetric detection of tunneling electrons. The calorimeter consists of a metallic island, containing an electron gas that acts as the absorber, see Fig. 4.4. Just as for the single electron box, the electron gas is assumed to have a very short relaxation time (on the order of nanoseconds), much faster than any other relevant time scales. We may thus at any instant of time assign an effective temperature to the absorber. The injector consists of a tunnel-coupled superconducting lead, with gap Δ and temperature T_s. From the injector, (quasi-)electrons tunnel with an energy Δ into the absorber. Each tunnel event gives rise to a change of the energy in the absorber and thus also a change of the absorber temperature. The advantage of using a superconducting injector instead of a normal metallic lead is twofold. First, every particle transfers an amount of heat of at least Δ. Second, a superconductor better isolates the island thermally, which improves the conditions for single-particle calorimetry.

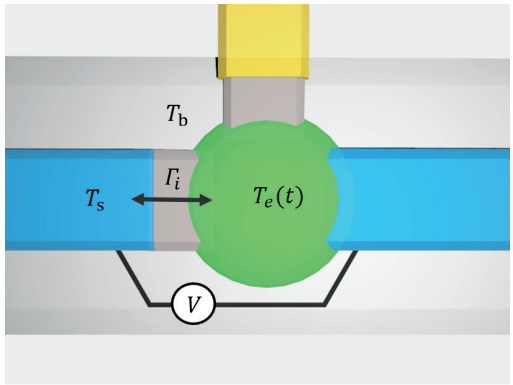

Figure 4.4: The quantum calorimeter proposed in Paper IV consisting of a metallic island (green) with quasi-temperature $T_e(t)$ as absorber, a superconducting injector with temperature T_s (left, blue), a potential regulor (right, blue) and a thermometer (yellow). The gray connections indicate tunnel couplings. A bias V may be applied between the injector and the regulator. Tunneling electrons are injected (or extracted) at a rate Γ_i. The bath of phonons in the sample has a fixed temperature T_b.

So far, the calorimeter resembles the single electron box; only that the normal metallic lead has been replaced by a superconductor. However, to be able to measure the temperature fluctuations we assume that another superconductor is tunnel coupled to the island. Under ideal conditions, the influence of this superconductor on the temperature statistics is negligible. To allow for ZBA thermometry and to fix the potential of the absorber, a third superconductor is also attached to the absorber. In contrast to the other two, this superconductor is clean contacted, so that an applied bias V between it and the injector only falls over the injector–absorber tunnel junction. At low temperatures, quasi-particle transport over the direct contact is suppressed and since there is no voltage drop over this junction the transfer of Cooper pairs do not carry any heat. This superconductor thus acts as both a heat mirror and a potential regulator.

Last, but not least, we are now taking into account the interaction between the electrons and the phonons. We will consider the regime where $\tau_i \sim \tau_{e-ph}$, i.e., the energy exchange with the injector takes place on the same time scale as with the phonons or even on a longer time scale. For the so-called single-injection event regime, $\tau_i \gg \tau_{e-ph}$, the injection events are well separated in time, allowing us to investigate the preconditions for quantum calorimetry.

Below we first investigate the heat transfer statistics in the system and then connect this to the temperature statistics. Finally, we discuss the experimental feasibility of implementing single-particle detection calorimetry and possible non-idealities.

4.4.1 Heat transfer statistics

Before analyzing the temperature statistics of our nanoscale calorimeter, we investigate the statistics of the heat transfer between the normal metallic island, on the one hand, and the superconducting injector and the phonon bath, on the other hand.

Superconducting injector

To fully describe the heat transfer statistics of the electrons tunneling between the superconducting injector and the normal metallic absorber, it is necessary to take into account the various energies that a single electron may transfer. The spectral rates are the rates at which a certain amount of energy is transferred by electrons tunneling into (+) or out of (−) the absorber. For a tunneling barrier, these rates are given by [41, 156]

$$\Gamma^i_+(E) = \frac{1}{e^2 R_T}\nu_S(E-eV)f(E-eV,T_s)[1-f(E,T_e)], \tag{4.47a}$$

$$\Gamma^i_-(E) = \frac{1}{e^2 R_T}\nu_S(E-eV)[1-f(E-eV,T_s)]f(E,T_e), \tag{4.47b}$$

where R_T is the tunnel resistance between the injector and the absorber, $\nu_S(E)$ is the normalized density of states in the superconductor and $f(E,T) = (\exp[E/(k_B T)]+1)^{-1}$ is the Fermi function. Just like in the section about thermometry, we will here assume that the superconductor is ideal in the sense that its normalized density of states is given by $\nu_S(E) = \theta(|E|-\Delta)\frac{|E|}{\sqrt{E^2-\Delta^2}}$.

In contrast to the single electron box, no charging effects are present in the metallic island due to the potential regulator. For given temperatures T_e and T_s, the tunneling processes at different energies are independent of each other and each process is Poissonian, i.e., uncorrelated. The cumulant generating function for the heat transfer statistics is then obtained as

$$F(\xi_i)/t = \int dE \left[\Gamma^i_+(E)(e^{i\xi_i E}-1) + \Gamma^i_-(E)(e^{-i\xi_i E}-1)\right], \tag{4.48}$$

where we have introduced the counting field ξ_i that couples to the net heat transfer between the injector and the absorber.

In general, Eq. (4.48) cannot be solved analytically. However, for $k_B T_s, k_B T_e \ll \Delta$, it describes the injection of particles with energies $\pm\Delta \pm eV$ (see the appendix of Paper IV for further details). In the limits (i) $V = 0$, $T_s \gg T_e$, (ii) $V = 0$, $T_s \ll T_e$ and (iii) $T_s(1-e|V|/\Delta) \ll T_e \ll e|V|/k_B$, the energy distribution of the injected particles becomes very focused at well-defined energies, $\varepsilon_i = \Delta$, $\varepsilon_{ii} = -\Delta$ and $\varepsilon_{iii} = eV-\Delta$, respectively, as

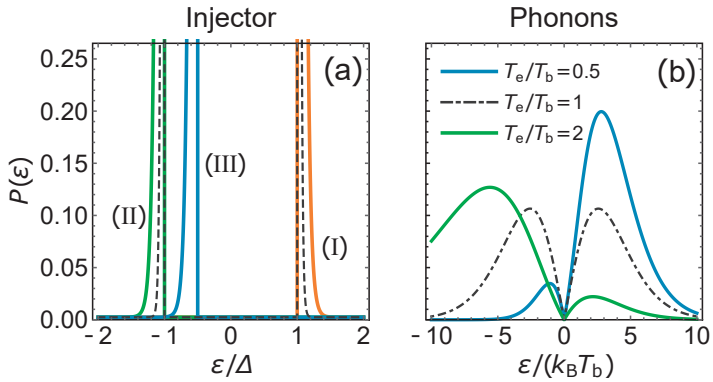

Figure 4.5: (a) The energy distribution of the injected electrons from the superconductor for four different sets of $\{k_B T_s/\Delta, k_B T_e/\Delta, eV/\Delta\} = \{0.02, 0.02, 0\}$ (dashed), $\{0.05, 0.01, 0\}$ (orange, solid), $\{0.01, 0.05, 0\}$ (green, solid) and $\{0.01, 0.05, 0.5\}$ (blue, solid). Corresponding injector regimes (I), (II) and (III) shown (see main text). (b) The energy distribution of the phonons absorbed and emitted from the environment for three different temperature settings, $T_e/T_b = 0.5$ (blue), $T_e/T_b = 1$ (black, dashed) and $T_e/T_b = 2$ (green).

shown in Fig. 4.5 (a). The corresponding CGF obtained from Eq. (4.48) is

$$F^{(\alpha)}(\xi_i, T_e) = \sqrt{2\pi}\frac{\Delta}{e^2 R_T} c_\alpha (e^{jE\xi_i} - 1), \qquad \alpha = i, ii, iii. \tag{4.49}$$

Here $c_i = h(T_s)$, $c_{ii} = h(T_e)$ and $c_{iii} = h(T_e)\exp[e|V|/(k_B T_e)]/2$ with

$$h(T) = \sqrt{k_B T/\Delta}\exp[-\Delta/(k_B T)]. \tag{4.50}$$

We see that the heat transfer statistics becomes Poissonian in these limits, with rates that may be tuned with the applied voltage V. Our superconducting lead thus works as a versatile injector of particles with tunable well-defined energies. This is one of the main findings of Papers IV. We also note that the thermal conductance κ_i over the tunnel junction, at least for small bias and temperature differences, is exponentially suppressed by $\Delta/(k_B T_b)$.

We finally note that in a real experiment there are several imperfections that might change the theoretical description above. First, impurities and other imperfections in the superconductor might lead to the presence of sub-gap states. This may be modeled by adjusting the normalized density of states of the superconductor [157–160], as discussed in the previous section on thermometry. However, this effect may be avoided in high-quality superconductors. At very low temperatures, the transfer of quasi-particles gets expontentially suppressed and the Andreev current plays an increasingly important role as the Thouless energy $E_{Th} = \hbar D/L^2$ may be of the same order of magnitude as the thermal energies, $k_B T_e$, $k_B T_s$. Here D is the diffusivity of the absorber and L its length. Importantly, for a biased junction, the Andreev current may carry heat [166]. Yet another imperfection is possible overheating of the superconducting lead. If the heat generated by the current flowing through the tunnel junction is not removed quickly enough, it could heat up the

superconductor and thus change its temperature from T_s. For simplicity, we neglect these effects here.

Phonon bath

The heat transfer between the absorber and the phonon bath differs from the injector–absorber heat transfer in the sense that we are now dealing with two different kinds of particles – fermionic electrons and bosonic phonons. Even so, in the weak-coupling limit, which holds at low temperatures, one may employ Fermi's golden rule and derive the following effective spectral rates (see the Appendix of Paper IV for further details) [167]

$$\Gamma^b_+(E) = \frac{\Sigma\mathcal{V}}{24k_B^5\zeta(5)}E^3 n(E,T_b)[1+n(E,T_e)], \tag{4.51a}$$

$$\Gamma^b_-(E) = \frac{\Sigma\mathcal{V}}{24k_B^5\zeta(5)}E^3 [1+n(E,T_b)]n(E,T_e). \tag{4.51b}$$

Here Σ is a coupling constant, $\mathcal{V}$ the volume of the electron gas, $\zeta(x)$ the Riemann zeta function and $n(E,T_b) = (\exp[E/(k_BT_b)]-1)^{-1}$ the Bose distribution. The spectral rates may be interpreted in a similar way as the injector–absorber rates. For instance the emission rate of phonons may be interpreted as the transfer of an energy E at a rate proportional to the number of phonons $[E^2 n(E,T_b)]$ and the total number of electrons that may scatter from an energy ε to an energy $\varepsilon - E$ ($n(E,T_e) = \int d\varepsilon f(\varepsilon,T_e)[1-f(\varepsilon-E,T_e)]$). The third E comes from the energy dependence of the scalar deformation potential of the phonons, see the Appendix of Paper IV for further details.

Analogous to the injector–absorber coupling, the CGF is directly obtained as

$$F(\xi_b)/t = \int dE\left[\Gamma^i_+(E)(e^{iE\xi_b}-1)+\Gamma^i_-(E)(e^{-iE\xi_b}-1)\right]. \tag{4.52}$$

The first two cumulants of the electron–phonon heat exchange are given by

$$\overline{J_E} = \frac{\langle E\rangle}{t} = \frac{\Sigma\mathcal{V}\zeta(4)}{\zeta(5)}(T_e^5 - T_b^5), \qquad S_{J_E}(0) = \frac{\langle\langle E^2\rangle\rangle}{t} \approx \frac{5\Sigma\mathcal{V}k_B\zeta(6)}{\zeta(5)}(T_e^6+T_b^6), \tag{4.53}$$

where the result for the first cumulant is exact and the result for the second cumulant is accurate approximately, with a deviation $< 2\%$. The energy distribution of the absorbed and emitted photons is shown in Fig. 4.5 (b). Compared to the injected electrons, the distribution is wider and smoother. The typical energy of the emitted or absorbed phonons is of the order of k_BT_b for $T_e \approx T_b$. The full expression for the absorber-bath coupling is another important main finding of Paper IV, and in good agreement with previous works

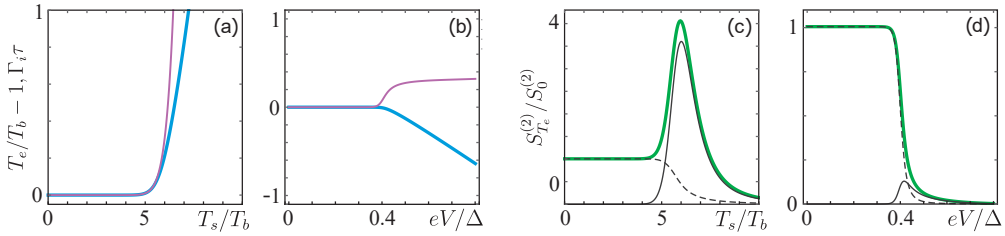

Figure 4.6: (a)–(b) The relative temperature deviation from the bath temperature (blue) and the injection rate (purple) for a pure thermal bias (a) and a pure voltage bias (b). (c)–(d) The temperature noise normalized by $S^{(2)}(0) = 2k_B T_b^2/\kappa$ with the phonon contribution (black, dashed), the injector contribution (black, solid) and the total contribution (green, solid) for a pure thermal bias (c) and a pure voltage bias (d).

in the field [168, 169]. We also note that the thermal conductance in the linear response regime is $\kappa_b = 5\Sigma\mathcal{V}T_b^4$.

We finally note that at very low temperatures, around 30-40 mK and below, *photonic* heat exchange with electromagnetic modes in the environment may also become important [170, 171]. This heat exchange is typically proportional to T^2, which means that at low temperatures it may dominate over the phononic heat exchange.

4.4.2 Temperature statistics

Having obtained the full heat transfer statistics, we are now in a position to consider the temperature statistics. We proceed in a similar way as for the single electron box. The average temperature of the absorber is obtained from

$$\overline{J_E^i}(\overline{T}_e, V) = \Sigma\mathcal{V}(\overline{T}_e^5 - \overline{T}_b^5). \tag{4.54}$$

For small temperature deviations, $\Delta T \equiv \overline{T}_e - T_b \ll T_b$, we find

$$\Delta T = \frac{\overline{J_E^i}(\overline{T}_b, V)}{\kappa} \tag{4.55}$$

where $\kappa = \kappa_i + \kappa_b$ is the total thermal conductance. Normally, at low temperatures and small bias, the thermal conductance to the superconducting injector is negligible and we get $\kappa \approx \kappa_b$. Using Eq. (4.43), we also obtain an expression for the temperature noise

$$S_T = \frac{S_{J_E}}{\kappa^2}. \tag{4.56}$$

Higher-order cumulants can be related in a similar way. Below we discuss the first two cumulants and how these depend on an applied temperature or voltage bias between the injector and the bath for our proposed nanoscale calorimeter.

Thermal bias

We consider the regime $\beta \gg \ln(r) \gg 1$, where $\beta = \Delta/(k_B T_b)$ and $r = \sqrt{2\pi} G_T \Delta^2/(e^2 T_b \kappa)$. The average temperature of the absorber is then obtained from

$$\overline{T_e} = T_b[1 + 5rh(T_s)]^{1/5}. \tag{4.57}$$

This function is shown in Fig. 4.6 (a) where a cross-over takes place at $T_s \sim T_s^* \equiv \Delta/[k_B \ln(r)]$ from constant (dominated by bath coupling) to exponentially increasing $e^{-\Delta/(5k_B T_s)}$ (dominated by injector coupling).

The noise is, in terms of the equilibrium phonon noise $S_0^{(2)} = 2k_B T_b^2/\kappa$, obtained as

$$\frac{S_{T_e}^{(2)}}{S_0^{(2)}} = \frac{1+q^6}{2q^8} + \frac{\beta(q^5-1)}{10q^8}, \tag{4.58}$$

where $q \equiv \overline{T_e}/T_b$. The phonon noise decreases around T_s^*, while the injected noise first increases and peaks at $T_s \approx T_s^*$. Importantly, the noise is suppressed for large temperature biases, as the thermal conductance $\kappa(\overline{T_e}) = \kappa q^4$ to the environment increases strongly and suppresses all temperature noise, see Fig. 4.6 (c).

We conclude that the most favorable operation point would be close to T_s^*. To achieve single-particle calorimetry and no back action from the absorber on the injection, we need $T_s \lesssim T_s^*$. In that case, we have $\Gamma_i \tau \ll 1$.

Voltage bias

For a voltage bias, we obtain using a similar analysis, a cross-over in the average temperature around $V^* \equiv [\Delta - \ln(r) k_B T_b]/e$ from a constant to close-to-linear decrease $k_B \overline{T_e} \approx (\Delta - eV)/\ln(r)$, see Fig. 4.6 (b). The noise is given by

$$\frac{S_{T_e}^{(2)}}{S_0^{(2)}} = \frac{q^4}{2} \frac{1 + q^6 + \frac{\tilde{\beta}}{5}(1-q^5)}{\left[q^6 + \frac{\tilde{\beta}}{5}(1-q^5)\right]^2}, \tag{4.59}$$

with $\tilde{\beta} = \beta(1 - eV/\Delta)$. This expression is a sum of the noise stemming from the injector ($\propto 1 - q^5$) and from the bath ($1 + q^6$). Similar to a thermal bias, the noise is dominated by the phonons at small bias and then, around V^*, gets dominated by the injector. Around V^*, the thermal conductance $\kappa(\overline{T_e}) = \kappa(q^4 + \tilde{\beta}(1-q^5)/[5q^2])$ starts to increase strongly, suppressing all temperature noise, see Fig. 4.6 (d).

4.4.3 Detection of single particles

We now consider the conditions for detecting energies of single particles, the aim of quantum calorimetry. If ε denotes the energy of a particle, the induced temperature change in the absorber is

$$\Delta T = \varepsilon / C, \tag{4.60}$$

provided that $\Delta T \ll T_e$ for which the heat capacity C of the system is approximately constant. At close-to-zero temperature, the absorber relaxes back to the background temperature that is set by the phonons (or photons) in the environment. This gives rise to a temperature spike

$$\Delta T(t) = \frac{\varepsilon}{C} e^{-t/\tau_C}, \tag{4.61}$$

where $\tau_C = C/\kappa$ is the relaxation time (at close-to-zero temperature it will be very long). This temperature spike may be detected provided that high-speed and ultrasensitive thermometry is available.

However, at finite temperature, things get more complicated. In that case, as we have already seen, the environment also induces temperature fluctuations. Phonons are exchanged randomly with the environment, which gives rise to stochastic fluctuations on top of the temperature spike(s) that we are interested in. If we consider the single-event regime, where injection events are well-separated in time, the average absorber temperature $\overline{T}_e$ will be very close to the bath temperature, $\overline{T}_e \approx T_b$. We may then apply the fluctuation–dissipation theorem, yielding the magnitude of the instantaneous noise

$$\sqrt{\langle\langle (\Delta T)^2 \rangle\rangle} = \sqrt{\frac{k_B T_b^2}{C}}. \tag{4.62}$$

To be able to detect the single temperature spikes among all the fluctuations induced by the energy exchange with the environment with a unit signal-to-noise ratio, we need to have

$$\varepsilon / C \sim \sqrt{\frac{k_B}{C}} T_b. \tag{4.63}$$

In the case of our proposed nanoscale calorimeter, we have $\Delta \approx 200$ μeV for an aluminum injector. For $C = 1000 k_B$, we get $T_b \sim \Delta / \sqrt{C k_B} \approx 6.25$ μeV$/k_B = 7.2$ mK. This is a very low temperature. Although not impossible, this shows that single-shot calorimetry is experimentally challenging.

As an alternative, or intermediate step, to single-particle calorimetry, one could perform a long-time measurement over many realizations. The advantage compared to a single-shot measurement would be that the whole distribution of injected energies in priniciple could be obtained. From the previous results, as shown in Fig. (4.6), it would be favorable to be

as close as possible to T_s^* and V^*, respectively, without leaving the regime where the time between subsequent injection events is much longer than the relaxation time, which also ensures that back-action effects of the injection events on the injector are avoided. By first measuring the temperature fluctuations for a negligible injection rate, one can extract the statistics of the fluctuations induced by the phonons. Then, activating the injector by, e.g., applying a temperature or voltage bias, one may extract the statistics of the temperature fluctuations owing to the injector only. From this, it is possible to infer the statistics of the heat transfer to the detector.

4.5 Summary and outlook

In this chapter, we have considered heat and temperature fluctuations and how to utilize them for quantum calorimetry. We first considered heat transport in the example system introduced in Ch. 2. In contrast to the average current, the bosonic and fermionic nature of the particles are clearly manifested in the zero-frequency noise expressions. The fluctuation–dissipation theorem relates the linear response of a perturbation, in this case the thermal conductance, to the noise in equilibrium.

The single electron box is a key component in this chapter. The results of Paper III shows how the temperature statistics is related to the heat transport statistics for such a setup, where a metallic island is coupled to a normal metallic lead. This setup also forms the basis for our quantum calorimetry, the main object of Paper IV. Although calorimetric detection of single electrons (and photons) constitute a highly challenging task experimentally, recent advances in the field of thermometry make the prospects of realizing such calorimetry in the near future very promising.

To improve the calorimeter, one could aim for an absorber with an even smaller heat capacity. For instance, instead of using a three-dimensional normal metallic island, one could use a two-dimensional material, for instance graphene, with a much smaller heat capacity. In a real experiment, it is necessary to take into account various imperfections that we have neglected in this chapter, including proximity effects from the potential regulator, Andreev tunneling and possible imperfections in the injector, e.g., in terms of the Dynes model [157–160].

Chapter 5

Conclusion and outlook

In this thesis we have addressed two different topics both related to nanoscale systems: quantum correlations and temperature fluctuations. We have investigated these phenomena motivated by both fundamental aspects and the prospects of future applications. The importance of fluctuations and the presence of coherences in nanoscale systems open up new possibilities that are not present in our daily world. In the case of entanglement, our results contribute to a deepened understanding of entanglement in nanoscale systems. For quantum calorimetry, the results of this thesis contributes to the development of new single-particle detectors in nanoscale systems. This would in turn open up the possibilities of investigating completely new phenomena in nanoscale systems related to heat transport.

In Paper I, we have investigated how a quantum dot system may be used to generate and detect orbitally entangled electrons on the picosecond time scale. This is achieved by utilizing cotunneling processes. Besides providing a proof-of-principle experiment of electronic orbital entanglement, the setup paves the way to single-shot correlation measurements based on single-electron detectors. This could lead to a nanoscale experiment analogous to the Bell tests performed with photons in quantum optics. We note that, to be useful for quantum computational purposes, it would be necessary to perform manipulations on the emitted entangled states, which could in principle be implemented by tuning the tunneling couplings.

In Paper II, we considered how to simplify the detection of entanglement in nanoscale systems. Using entanglement witnesses, we show that the number of zero-frequency cross-correlations needed to detect bipartite entanglement may be reduced significantly compared to what a conventional Bell tests require. All pure entangled states, except the maximally entangled, may be detected with only two measurements. Surprisingly, the maximally entangled states require three. Importantly, the three measurement axes may still be chosen

to lie in the same plane, a great advantage from an experimental point of view.

In Paper III and IV, we investigated the relation between heat transfer statistics and temperature fluctuations. In Paper III, we derived this relation for a metallic island, with high charging energy, coupled to a normal metallic lead, the so-called single electron box. In Paper IV, we proposed a nanoscale quantum calorimeter for detection of tunneling electrons. The results show that quantum calorimetry is within experimental reach, albeit very challenging. One of the main challenges here is to distinguish fluctuations induced by the environment from the fluctuations induced by the injection events of interest. One way of improving the sensitivity of the calorimeter would be to use absorbers with smaller heat capacities, for instance lower dimensional systems, such as graphene. Another way could be to go to even lower temperatures, however, this may be challenging experimentally.

In Paper V, we considered photon emissions from a microwave cavity. These results have been illustrated throughout the thesis with the help of our example system. The results illustrate some of the important difference between short-time and long-time transport physics. It also illustrates the difference between, e.g., waiting time distribution and the second-order degree of coherence. Furthermore, we have investigated heat transport in this system. Importantly, new single-photon detectors based on calorimeters could pave the way to experimentally investigate photon emissions from a single cavity.

It would be interesting to try to combine the two topics of this thesis, for instance by investigating if new calorimetric methods could be utilized to detect coherences and entanglement. That could open up completely new ways of studying entangled states, which would be of great importance for future quantum information processing.

References

[1] M. Di Ventra, *Electrical Transport in Nanoscale Systems* (Cambridge University Press, 2008).

[2] M. A. Nielsen and I. L. Chuang, *Quantum Computation and Quantum Information* (Cambridge University Press, 2010).

[3] F. Binder, L. A. Correa, C. Gogolin, J. Anders, and A. G., *Thermodynamics in the Quantum Regime – Fundamental Aspects and New Directions* (Springer International Publishing, 2018).

[4] A. Einstein, B. Podolsky, and N. Rosen, Phys. Rev. **47**, 777 (1935).

[5] J. S. Bell, Physics **1**, 195 (1964).

[6] E. Schrödinger, Proc. Camb. Phil. Soc. **31** (1935).

[7] C. H. Bennett and S. J. Wiesner, Phys. Rev. Lett. **69**, 2881 (1992).

[8] C. H. Bennett, G. Brassard, C. Crépeau, R. Jozsa, A. Peres, and W. K. Wootters, Phys. Rev. Lett. **70**, 1895 (1993).

[9] A. K. Ekert, Phys. Rev. Lett. **67**, 661 (1991).

[10] D. Gottesman and I. L. Chuang, Nature **402** (1999).

[11] N. Gisin and R. Thew, Nat. Photonics **1**, 165 (2007).

[12] M. Krenn, M. Malik, T. Scheidl, R. Ursin, and A. Zeilinger, "Quantum communication with photons," in *Optics in Our Time*, edited by M. D. Al-Amri, M. El-Gomati, and M. S. Zubairy (Springer International Publishing, Cham, 2016) pp. 455–482.

[13] H. Häffner, C. Roos, and R. Blatt, Physics Reports **469**, 155 (2008).

[14] M. H. Devoret, A. Wallraff, and J. M. Martinis, arXiv:0411174 (2004).

[15] S. D. Sarma, M. Freedman, and C. Nayak, npj Quantum Information **1**, 15001 (2015).

[16] D. Loss and D. P. DiVincenzo, Phys. Rev. A **57**, 120 (1998).

[17] J. Levy, Phys. Rev. Lett. **89**, 147902 (2002).

[18] A. Bertoni, P. Bordone, R. Brunetti, C. Jacoboni, and S. Reggiani, Phys. Rev. Lett. **84**, 5912 (2000).

[19] P. Samuelsson, E. V. Sukhorukov, and M. Büttiker, Phys. Rev. Lett. **91**, 157002 (2003).

[20] R. Ruskov and A. N. Korotkov, Phys. Rev. B **67**, 241305 (2003).

[21] W. Mao, D. V. Averin, R. Ruskov, and A. N. Korotkov, Phys. Rev. Lett. **93**, 056803 (2004).

[22] B. Trauzettel, A. N. Jordan, C. W. J. Beenakker, and M. Büttiker, Phys. Rev. B **73**, 235331 (2006).

[23] T. Fujisawa, G. Shinkai, T. Hayashi, and T. Ota, Physica E **43**, 730 (2011).

[24] P. Samuelsson, E. V. Sukhorukov, and M. Büttiker, Phys. Rev. Lett. **92**, 026805 (2004).

[25] C. W. J. Beenakker, C. Emary, M. Kindermann, and J. L. van Velsen, Phys. Rev. Lett. **91**, 147901 (2003).

[26] I. Neder, N. Ofek, Y. Chung, M. Heiblum, D. Mahalu, and V. Umansky, Nature (London) **448**, 333 (2007).

[27] T. Hayashi, T. Fujisawa, H. D. Cheong, Y. H. Jeong, and Y. Hirayama, Phys. Rev. Lett. **91**, 226804 (2003).

[28] P. Roulleau, F. Portier, P. Roche, A. Cavanna, G. Faini, U. Gennser, and D. Mailly, Phys. Rev. Lett. **100**, 126802 (2008).

[29] K. D. Petersson, J. R. Petta, H. Lu, and A. C. Gossard, Phys. Rev. Lett. **105**, 246804 (2010).

[30] J. Basset, A. Stockklauser, D.-D. Jarausch, T. Frey, C. Reichl, W. Wegscheider, A. Wallraff, K. Ensslin, and T. Ihn, Appl. Phys. Lett. **105**, 063105 (2014).

[31] L. Faoro and F. Taddei, Phys. Rev. B **75**, 165327 (2007).

[32] W. Kłobus, A. Grudka, A. Baumgartner, D. Tomaszewski, C. Schönenberger, and J. Martinek, Phys. Rev. B **89**, 125404 (2014).

[33] J. P. Baltanás and D. Frustaglia, Journal of Physics: Condensed Matter **27**, 485302 (2015).

[34] F. Brange, O. Malkoc, and P. Samuelsson, Phys. Rev. Lett. **118**, 036804 (2017).

[35] L. D. Landau and E. M. Lifshitz, *Statistical Physics* (Butterworth–Heinemann, 1980).

[36] C. Jarzynski, Phys. Rev. Lett. **78**, 2690 (1997).

[37] C. Jarzynski, Phys. Rev. E **56**, 5018 (1997).

[38] G. E. Crooks, Phys. Rev. E **60**, 2721 (1999).

[39] Z. Cui, *Nanofabrication* (Springer, 2008).

[40] H. Pothier, S. Guéron, N. O. Birge, D. Esteve, and M. H. Devoret, Phys. Rev. Lett. **79**, 3490 (1997).

[41] F. Giazotto, T. T. Heikkilä, A. Luukanen, A. M. Savin, and J. P. Pekola, Rev. Mod. Phys. **78**, 217 (2006).

[42] A. V. Feshchenko, L. Casparis, I. M. Khaymovich, D. Maradan, O.-P. Saira, M. Palma, M. Meschke, J. P. Pekola, and D. M. Zumbühl, Phys. Rev. Applied **4**, 034001 (2015).

[43] B. Karimi and J. P. Pekola, Phys. Rev. Applied **10**, 054048 (2018).

[44] C. Kilbourne Stahle, D. McCammon, and K. D. Irwin, Physics Today **52**, 32 (1999).

[45] Y. V. Nazarov and Y. M. Blanter, *Quantum Transport – Introduction to Nanoscience* (Cambridge University Press, 2009).

[46] R. Landauer, Nature **392** (1998).

[47] C. J. Isham, *Lectures On Quantum Theory: Mathematical And Structural Foundations* (Imperial College Press, 1995).

[48] W. Heisenberg, Zeitschrift für Physik **43**, 172 (1927).

[49] J. J. Sakurai, *Modern Quantum Mechanics* (Pearson, 2007).

[50] H. Bruus and K. Flensberg, *Many-Body Quantum Theory in Condensed Matter Physics* (Oxford Graduate Texts, 2004).

[51] W. Pauli, Zeitschrift für Physik **31**, 765 (1925).

[52] H.-P. Breuer, E.-M. Laine, J. Piilo, and B. Vacchini, Rev. Mod. Phys. **88**, 021002 (2016).

[53] V. Gorini, A. Kossakowski, and E. C. G. Sudarshan, Journal of Mathematical Physics **17**, 821 (1976), https://aip.scitation.org/doi/pdf/10.1063/1.522979 .

[54] G. Lindblad, Communications in Mathematical Physics **48**, 119 (1976).

[55] U. Fano, Phys. Rev. **72**, 26 (1947).

[56] Y. Blanter and Büttiker, Phys. Rep. **336**, 1 (2000).

[57] C. Emary, C. Pöltl, A. Carmele, J. Kabuss, A. Knorr, and T. Brandes, Phys. Rev. B **85**, 165417 (2012).

[58] H. E. Daniels, Ann. Math. Statist. **25**, 631 (1954).

[59] D. K. C. Macdonald, Reports on Progress in Physics **12**, 56 (1949).

[60] C. Flindt, T. Novotný, and A.-P. Jauho, Physica E: Low-dimensional Systems and Nanostructures **29**, 411 (2005), frontiers of Quantum.

[61] N. Lambert, R. Aguado, and T. Brandes, Phys. Rev. B **75**, 045340 (2007).

[62] H. J. Carmichael, S. Singh, R. Vyas, and P. R. Rice, Phys. Rev. A **39**, 1200 (1989).

[63] M. Albert, G. Haack, C. Flindt, and M. Büttiker, Phys. Rev. Lett. **108**, 186806 (2012).

[64] G. Haack, M. Albert, and C. Flindt, Phys. Rev. B **90**, 205429 (2014).

[65] B. Küng, O. Pfäffli, S. Gustavsson, T. Ihn, K. Ensslin, M. Reinwald, and W. Wegscheider, Phys. Rev. B **79**, 035314 (2009).

[66] S. Gustavsson, R. Leturcq, B. Simovič, R. Schleser, T. Ihn, P. Studerus, K. Ensslin, D. C. Driscoll, and A. C. Gossard, Phys. Rev. Lett. **96**, 076605 (2006).

[67] S. Gustavsson, R. Leturcq, B. Simovič, R. Schleser, P. Studerus, T. Ihn, K. Ensslin, D. C. Driscoll, and A. C. Gossard, Phys. Rev. B **74**, 195305 (2006).

[68] C. Flindt, C. Fricke, F. Hohls, T. Novotný, K. Netočný, T. Brandes, and R. J. Haug, Proc. Natl. Acad. Sci. **106**, 10116 (2009).

[69] Y.-F. Chen, D. Hover, S. Sendelbach, L. Maurer, S. T. Merkel, E. J. Pritchett, F. K. Wilhelm, and R. McDermott, Phys. Rev. Lett. **107**, 217401 (2011).

[70] I. Kunihiro, Z. Lin, K. Koshino, W. D. Oliver, J.-S. Tsai, T. Yamamoto, and Y. Nakamura, Nat. Commun. **7**, 12303 (2016).

[71] A. Narla, S. Shankar, M. Hatridge, Z. Leghtas, K. M. Sliwa, E. Zalys-Geller, S. O. Mundhada, W. Pfaff, L. Frunzio, R. J. Schoelkopf, and M. H. Devoret, Phys. Rev. X **6**, 031036 (2016).

[72] J.-C. Besse, S. Gasparinetti, M. C. Collodo, T. Walter, P. Kurpiers, M. Pechal, C. Eichler, and A. Wallraff, Phys. Rev. X **8**, 021003 (2018).

[73] S. Kono, K. Koshino, Y. Tabuchi, A. Noguchi, and Y. Nakamura, Nat. Phys. **14**, 546–549 (2018).

[74] S. J. Freedman and J. F. Clauser, Phys. Rev. Lett. **28**, 938 (1972).

[75] J. F. Clauser and A. Shimony, Reports on Progress in Physics **41**, 1881 (1978).

[76] A. Aspect, J. Dalibard, and G. Roger, Phys. Rev. Lett. **49**, 1804 (1982).

[77] M. Giustina, M. A. M. Versteegh, S. Wengerowsky, J. Handsteiner, A. Hochrainer, K. Phelan, F. Steinlechner, J. Kofler, J.-A. Larsson, C. Abellán, W. Amaya, V. Pruneri, M. W. Mitchell, J. Beyer, T. Gerrits, A. E. Lita, L. K. Shalm, S. W. Nam, T. Scheidl, R. Ursin, B. Wittmann, and A. Zeilinger, Phys. Rev. Lett. **115**, 250401 (2015).

[78] B. Hensen, H. Bernien, A. E. Dréau, A. Reiserer, N. Kalb, M. S. Blok, J. Ruitenberg, R. F. L. Vermeulen, R. N. Schouten, C. Abellán, W. Amaya, V. Pruneri, M. W. Mitchell, M. Markham, D. J. Twitchen, D. Elkouss, S. Wehner, T. H. Taminiau, and R. Hanson, Nature **526**, 682 (2015).

[79] L. K. Shalm, E. Meyer-Scott, B. G. Christensen, P. Bierhorst, M. A. Wayne, M. J. Stevens, T. Gerrits, S. Glancy, D. R. Hamel, M. S. Allman, K. J. Coakley, S. D. Dyer, C. Hodge, A. E. Lita, V. B. Verma, C. Lambrocco, E. Tortorici, A. L. Migdall, Y. Zhang, D. R. Kumor, W. H. Farr, F. Marsili, M. D. Shaw, J. A. Stern, C. Abellán, W. Amaya, V. Pruneri, T. Jennewein, M. W. Mitchell, P. G. Kwiat, J. C. Bienfang, R. P. Mirin, E. Knill, and S. W. Nam, Phys. Rev. Lett. **115**, 250402 (2015).

[80] D. Bohm, *Quantum Theory* (Prentice Hall, 1951).

[81] L. de Broglie, J. Phys. Radium **8**, 225 (1927).

[82] D. Bohm, Phys. Rev. **85**, 166 (1952).

[83] D. Bohm, Phys. Rev. **85**, 180 (1952).

[84] J. F. Clauser, M. A. Horne, A. Shimony, and R. A. Holt, Phys. Rev. Lett. **23**, 880 (1969).

[85] A. Aspect, Nature **398**, 189 (2007).

[86] P. R. Tapster, J. G. Rarity, and P. C. M. Owens, Phys. Rev. Lett. **73**, 1923 (1994).

[87] W. Tittel, J. Brendel, B. Gisin, T. Herzog, H. Zbinden, and N. Gisin, Phys. Rev. A **57**, 3229 (1998).

[88] G. Weihs, T. Jennewein, C. Simon, H. Weinfurter, and A. Zeilinger, Phys. Rev. Lett. **81**, 5039 (1998).

[89] T. Scheidl, R. Ursin, J. Kofler, S. Ramelow, X.-S. Ma, T. Herbst, L. Ratschbacher, A. Fedrizzi, N. K. Langford, T. Jennewein, and A. Zeilinger, Proceedings of the National Academy of Sciences **107**, 19708 (2010), https://www.pnas.org/content/107/46/19708.full.pdf .

[90] M. Giustina, A. Mech, S. Ramelow, B. Wittmann, J. Kofler, J. Beyer, A. Lita, B. Calkins, T. Gerrits, S. W. Nam, R. Ursin, and A. Zeilinger, Nature **497**, 227 (2013).

[91] J. Handsteiner, A. S. Friedman, D. Rauch, J. Gallicchio, B. Liu, H. Hosp, J. Kofler, D. Bricher, M. Fink, C. Leung, A. Mark, H. T. Nguyen, I. Sanders, F. Steinlechner, R. Ursin, S. Wengerowsky, A. H. Guth, D. I. Kaiser, T. Scheidl, and A. Zeilinger, Phys. Rev. Lett. **118**, 060401 (2017).

[92] C. H. Bennett, D. P. DiVincenzo, C. A. Fuchs, T. Mor, E. Rains, P. W. Shor, J. A. Smolin, and W. K. Wootters, Phys. Rev. A **59**, 1070 (1999).

[93] R. F. Werner, Phys. Rev. A **40**, 4277 (1989).

[94] A. Peres, Phys. Rev. Lett. 77, 1413 (1996).

[95] M. Horodecki, P. Horodecki, and R. Horodecki, Phys. Lett. A **223**, 1 (1996).

[96] D. P. DiVincenzo, Fortschritte der Physik **48** (2000).

[97] J. Fischer and D. Loss, Science **324**, 1277 (2009).

[98] P. Recher, E. V. Sukhorukov, and D. Loss, Phys. Rev. B **63**, 165314 (2001).

[99] C. Bena, S. Vishveshwara, L. Balents, and M. P. A. Fisher, Phys. Rev. Lett. **89**, 037901 (2002).

[100] Y. A. Pashkin, T. Yamamoto, O. Astafiev, Y. Nakamura, D. V. Averin, and J. S. Tsai, Nature (London) **421**, 823 (2003).

[101] M. Steffen, M. Ansmann, R. C. Bialczak, N. Katz, E. Lucero, R. McDermott, M. Neeley, E. M. Weig, A. N. Cleland, and J. M. Martinis, Science **313**, 1423 (2006).

[102] J. R. Petta, A. C. Johnson, J. M. Taylor, E. A. Laird, A. Yacoby, M. D. Lukin, C. M. Marcus, M. P. Hanson, and A. C. Gossard, Science **309**, 2180 (2005).

[103] F. H. L. Koppens, C. Buizert, K. J. Tielrooij, I. T. Vink, K. C. Nowack, T. Meunier, L. P. Kouwenhoven, and L. M. K. Vandersypen, Nature (London) **442**, 766 (2006).

[104] R. Brunner, Y.-S. Shin, T. Obata, M. Pioro-Ladrière, T. Kubo, K. Yoshida, T. Taniyama, Y. Tokura, and S. Tarucha, Phys. Rev. Lett. **107**, 146801 (2011).

[105] M. D. Shulman, O. E. Dial, S. P. Harvey, H. Bluhm, V. Umansky, and A. Yacoby, Science **336**, 202 (2012).

[106] L. Hofstetter, S. Csonka, J. Nygård, and C. Schönenberger, Nature (London) **461**, 960 (2009).

[107] L. G. Herrmann, F. Portier, P. Roche, A. L. Yeyati, T. Kontos, and C. Strunk, Phys. Rev. Lett. **104**, 026801 (2010).

[108] A. Das, Y. Ronen, M. Heiblum, D. Mahalu, A. V. Kretinin, and H. Shtrikman, Nat. Commun. **3**, 1165 (2012).

[109] J. Schindele, A. Baumgartner, and C. Schönenberger, Phys. Rev. Lett. **109**, 157002 (2012).

[110] G. Shinkai, T. Hayashi, T. Ota, and T. Fujisawa, Phys. Rev. Lett. **103**, 056802 (2009).

[111] F. Brange, O. Malkoc, and P. Samuelsson, Phys. Rev. Lett. **114**, 176803 (2015).

[112] Y. Dovzhenko, J. Stehlik, K. D. Petersson, J. R. Petta, H. Lu, and A. C. Gossard, Phys. Rev. B **84**, 161302 (2011).

[113] M. Yamamoto, S. Takada, C. Bäuerle, K. Watanabe, A. D. Wieck, and S. Tarucha, Nature Nanotech. **7**, 247 (2012).

[114] G. Cao, H.-O. Li, T. Tu, L. Wang, C. Zhou, and M. Xiao, Nat. Commun. **4**, 1 (2013).

[115] M. B. Plenio and S. Virmani, Quant. Inf. Comput. **7**, 1 (2007), arXiv:quant-ph/0504163 [quant-ph] .

[116] C. H. Bennett, H. J. Bernstein, S. Popescu, and B. Schumacher, Phys. Rev. A **53**, 2046 (1996).

[117] S. Hill and W. K. Wootters, Phys. Rev. Lett. **78**, 5022 (1997).

[118] W. K. Wootters, Phys. Rev. Lett. **80**, 2245 (1998).

[119] S. Kawabata, J. Phys. Soc. Japan **70**, 1210 (2001).

[120] N. M. Chtchelkatchev, G. Blatter, G. B. Lesovik, and T. Martin, Phys. Rev. B **66**, 161320 (2002).

[121] P. Samuelsson and M. Büttiker, Phys. Rev. B **73**, 041305 (2006).

[122] G. Burkard, D. Loss, and E. V. Sukhorukov, Phys. Rev. B **61**, R16303 (2000).

[123] M. Büttiker, Phys. Rev. B **46**, 12485 (1992).

[124] O. Malkoc, C. Bergenfeldt, and P. Samuelsson, EPL **105**, 47013 (2014).

[125] B. M. Terhal, Phys. Lett. A **271**, 319 (2000).

[126] O. Gühne, P. Hyllus, D. Bruß, A. Ekert, M. Lewenstein, C. Macchiavello, and A. Sanpera, Phys. Rev. A **66**, 062305 (2002).

[127] G. Tóth and O. Gühne, Appl. Phys. B **82**, 237 (2006).

[128] W. Laskowski, D. Richart, C. Schwemmer, T. Paterek, and H. Weinfurter, Phys. Rev. Lett. **108**, 240501 (2012).

[129] G. Tóth and O. Gühne, Phys. Rev. Lett. **94**, 060501 (2005).

[130] E. A. Yuzbashyan, W. Happer, B. L. Altshuler, and S. B. Shastry, J. Phys. A: Math. Gen. **36**, 2577 (2003).

[131] J.-M. Hou and W. Chen, arXiv:1507.02024 (2015).

[132] S. Vinjanampathy and J. Anders, Contemporary Physics **57**, 545 (2016), https://doi.org/10.1080/00107514.2016.1201896 .

[133] Y. Dubi and M. Di Ventra, Rev. Mod. Phys. **83**, 131 (2011).

[134] N. W. Ashcroft and N. D. Mermin, *Solid State Physics* (Brooks-Cole, 1976).

[135] C. L. Kane and M. P. A. Fisher, Phys. Rev. Lett. **76**, 3192 (1996).

[136] N. J. Appleyard, J. T. Nicholls, M. Pepper, W. R. Tribe, M. Y. Simmons, and D. A. Ritchie, Phys. Rev. B **62**, R16275 (2000).

[137] M.-R. Li and E. Orignac, EPL (Europhysics Letters) **60**, 432 (2002).

[138] T. Rejec, A. Ramšak, and J. H. Jefferson, Phys. Rev. B **65**, 235301 (2002).

[139] B. Kubala, J. König, and J. Pekola, Phys. Rev. Lett. **100**, 066801 (2008).

[140] P. Murphy, S. Mukerjee, and J. Moore, Phys. Rev. B **78**, 161406 (2008).

[141] A. Garg, D. Rasch, E. Shimshoni, and A. Rosch, Phys. Rev. Lett. **103**, 096402 (2009).

[142] A. Principi and G. Vignale, Phys. Rev. Lett. **115**, 056603 (2015).

[143] B. Dutta, J. T. Peltonen, D. S. Antonenko, M. Meschke, M. A. Skvortsov, B. Kubala, J. König, C. B. Winkelmann, H. Courtois, and J. P. Pekola, Phys. Rev. Lett. **119**, 077701 (2017).

[144] H. Nyquist, Phys. Rev. **32**, 110 (1928).

[145] H. B. Callen and T. A. Welton, Phys. Rev. **83**, 34 (1951).

[146] U. Mizutani, *Introduction to the Electron Theory of Metals* (Cambridge University Press, 2001).

[147] T. C. P. Chui, D. R. Swanson, M. J. Adriaans, J. A. Nissen, and J. A. Lipa, Phys. Rev. Lett. **69**, 3005 (1992).

[148] S. Gasparinetti, F. Deon, G. Biasiol, L. Sorba, F. Beltram, and F. Giazotto, Phys. Rev. B **83**, 201306 (2011).

[149] J. P. Pekola, K. P. Hirvi, J. P. Kauppinen, and M. A. Paalanen, Phys. Rev. Lett. **73**, 2903 (1994).

[150] L. Casparis, M. Meschke, D. Maradan, A. C. Clark, C. P. Scheller, K. K. Schwarzwälder, J. P. Pekola, and D. M. Zumbühl, Review of Scientific Instruments **83**, 083903 (2012), https://doi.org/10.1063/1.4744944 .

[151] P. Dubos, H. Courtois, B. Pannetier, F. K. Wilhelm, A. D. Zaikin, and G. Schön, Phys. Rev. B **63**, 064502 (2001).

[152] A. Mavalankar, S. J. Chorley, J. Griffiths, G. A. C. Jones, I. Farrer, D. A. Ritchie, and C. G. Smith, Applied Physics Letters **103**, 133116 (2013), https://doi.org/10.1063/1.4823703 .

[153] D. Maradan, L. Casparis, T.-M. Liu, D. E. F. Biesinger, C. P. Scheller, D. M. Zumbühl, J. D. Zimmerman, and A. C. Gossard, Journal of Low Temperature Physics **175**, 784 (2014).

[154] L. Spietz, K. W. Lehnert, I. Siddiqi, and R. J. Schoelkopf, Science **300**, 1929 (2003), http://science.sciencemag.org/content/300/5627/1929.full.pdf .

[155] L. Spietz, R. J. Schoelkopf, and P. Pari, Applied Physics Letters **89**, 183123 (2006), https://doi.org/10.1063/1.2382736 .

[156] D. Golubev and L. Kuzmin, Journal of Applied Physics **89**, 6464 (2001), https://doi.org/10.1063/1.1351002 .

[157] R. C. Dynes, V. Narayanamurti, and J. P. Garno, Phys. Rev. Lett. **41**, 1509 (1978).

[158] Y. Noat, V. Cherkez, C. Brun, T. Cren, C. Carbillet, F. Debontridder, K. Ilin, M. Siegel, A. Semenov, H.-W. Hübers, and D. Roditchev, Phys. Rev. B **88**, 014503 (2013).

[159] P. Szabó, T. Samuely, V. Hašková, J. Kačmarčík, M. Žemlička, M. Grajcar, J. G. Rodrigo, and P. Samuely, Phys. Rev. B **93**, 014505 (2016).

[160] F. c. v. Herman and R. Hlubina, Phys. Rev. B **97**, 014517 (2018).

[161] Frossati, G., J. Phys. Colloques **39**, C6 (1978).

[162] D. J. Cousins, S. N. Fisher, A. M. Guénault, R. P. Haley, I. E. Miller, G. R. Pickett, G. N. Plenderleith, P. Skyba, P. Y. A. Thibault, and M. G. Ward, Journal of Low Temperature Physics **114**, 547 (1999).

[163] D. R. Schmidt, C. S. Yung, and A. N. Cleland, Appl. Phys. Lett. **83**, 1002 (2003).

[164] D. R. Schmidt, C. S. Yung, and A. N. Cleland, Phys. Rev. B **69**, 140301 (2004).

[165] S. Gasparinetti, K. L. Viisanen, O.-P. Saira, T. Faivre, M. Arzeo, M. Meschke, and J. P. Pekola, Phys. Rev. Applied **3**, 014007 (2015).

[166] A. S. Vasenko, E. V. Bezuglyi, H. Courtois, and F. W. J. Hekking, Phys. Rev. B **81**, 094513 (2010).

[167] G. D. Mahan, *Many-Particle Physics* (Springer US, 2000).

[168] F. C. Wellstood, C. Urbina, and J. Clarke, Phys. Rev. B **49**, 5942 (1994).

[169] J. P. Pekola and B. Karimi, Journal of Low Temperature Physics **191**, 373 (2018).

[170] D. R. Schmidt, R. J. Schoelkopf, and A. N. Cleland, Phys. Rev. Lett. **93**, 045901 (2004).

[171] A. V. Timofeev, M. Helle, M. Meschke, M. Möttönen, and J. P. Pekola, Phys. Rev. Lett. **102**, 200801 (2009).

[172] H.-P. Breuer and F. Petruccione, *The Theory of Open Quantum Systems* (Oxford University Press, 2002).

[173] D. Lidar, arXiv:1902.00967 (2019).

[174] J. R. Schrieffer and P. A. Wolff, Phys. Rev. **149**, 491 (1966).

[175] D. V. Averin and V. Nazarov, in *Single Charge Tunneling*, NATO ASI Series, edited by H. Grabert and M. H. Devoret (Plenum, New York, 1992, New York, 1992) Chap. 6, pp. 217–249.

Part III

Appendices

Appendix A: Master equations

Here we give an example of how the Lindblad equation describing the reduced dynamics of a system (henceforth called the *principal system*) weakly coupled to an environment may be derived. The derivation follows along the lines of Refs. [172, 173]. We start by considering the Hamiltonian of the total combined system

$$\hat{H} = \hat{H}_S + \hat{H}_E + \hat{H}_{\text{int}}, \tag{1}$$

where $\hat{H}_S$ is the part of the Hamiltonian acting only on the principal system, $\hat{H}_E$ is the part of the Hamiltonian acting only on the environment and $\hat{H}_{\text{int}} = \sum_\alpha \hat{A}_\alpha \otimes \hat{B}_\alpha$ is the part of the Hamiltonian describing the interaction between the principal system and the environment. Here $\hat{A}_\alpha$ and $\hat{B}_\alpha$ are operators acting only on the principal system and the environment, respectively.

Assuming that the principal system together with its environment form a closed system (we may take this as a defining property of the environment), the time evolution of the density matrix $\hat{\sigma}(t)$ of the total combined system is obtained from the Liouville–von Neumann equation

$$\frac{d\hat{\sigma}(t)}{dt} = -\frac{i}{\hbar}\left[\hat{H}, \hat{\sigma}(t)\right], \tag{2}$$

where $[\hat{A}, \hat{B}] \equiv \hat{A}\hat{B} - \hat{B}\hat{A}$ denotes the commutator.

To derive the Lindblad equation, we first switch to the interaction picture by transforming all operators as $\hat{A}_I(t) \equiv e^{\frac{i}{\hbar}(\hat{H}_S+\hat{H}_E)t}\hat{A}(t)e^{-\frac{i}{\hbar}(\hat{H}_S+\hat{H}_E)t}$, where $A_I(t)$ is the interaction-picture version of an operator $A(t)$. The Liouville–von Neumann equation is then transformed into the Schwinger–Tomonaga equation

$$\frac{d\hat{\sigma}_I(t)}{dt} = -\frac{i}{\hbar}\left[\hat{H}_{\text{int}}(t), \hat{\sigma}_I(t)\right] = \mathcal{L}(t)\hat{\sigma}_I(t), \tag{3}$$

which forms the starting point for the derivation of the Lindblad equation.

Derivation of the Nakajima–Zwanzig equation

For completeness, we start by deriving the Nakajima–Zwanzig equation, which is an exact reformulation of the Liouville–von Neumann equation as a master equation. From this equation, we will then derive the Lindblad equation under a number of assumptions.

The idea behind the derivation of the Nakajima–Zwanzig equation is to use a projection superoperator $\mathcal{P}$ that projects out the irrelevant parts of the total density matrix and only keeps the relevant part, $\mathcal{P}\hat{\sigma}(t) = \mathrm{tr}_B\{\hat{\sigma}(t)\} \otimes \hat{\rho}_B$, where $\hat{\rho}_B$ is the stationary state (typically a Gibbs state) of the bath, $[\hat{H}_E, \hat{\rho}_B] = 0$. In the following, we will let $\mathcal{Q} = I - \mathcal{P}$ denote the complementary projection superoperator. We note that both the projection superoperators fulfill the characteristic idempotence property of projectors, $\mathcal{P}^2 = \mathcal{P}$ and $\mathcal{Q}^2 = \mathcal{Q}$.

Applying the projection superoperators on the Schwinger–Tomonaga equation, together with the identity $\mathbf{I} = \mathcal{P} + \mathcal{Q}$, we obtain

$$\frac{d}{dt}\mathcal{P}\hat{\sigma}_I(t) = \mathcal{P}\mathcal{L}(t)\mathcal{P}\hat{\sigma}_I(t) + \mathcal{P}\mathcal{L}(t)\mathcal{Q}\hat{\sigma}_I(t), \tag{4a}$$

$$\frac{d}{dt}\mathcal{Q}\hat{\sigma}_I(t) = \mathcal{Q}\mathcal{L}(t)\mathcal{P}\hat{\sigma}_I(t) + \mathcal{Q}\mathcal{L}(t)\mathcal{Q}\hat{\sigma}_I(t). \tag{4b}$$

The formal solution to the second equation is

$$\mathcal{Q}\hat{\sigma}_I(t) = \mathcal{G}(t,0)\mathcal{Q}\hat{\sigma}_I(0) + \int_0^t ds G(t,s)\mathcal{Q}\mathcal{L}(s)\mathcal{Q}\hat{\sigma}_I(s), \tag{5}$$

where $\mathcal{G}(t,0) = T_{\leftarrow}\exp\left[\int_0^t ds\mathcal{Q}\mathcal{L}(s)\right]$ is a propagator. Plugging this back into Eq. (4a), we obtain the Nakajima–Zwanzig equation

$$\frac{d}{dt}\mathcal{P}\hat{\sigma}_I(t) = \mathcal{P}\mathcal{L}(t)\mathcal{P}\hat{\sigma}_I(t) + \mathcal{P}\mathcal{L}(t)\mathcal{G}(t,0)\mathcal{Q}\hat{\sigma}_I(0) + \int_0^t ds\mathcal{P}\mathcal{L}(t)\mathcal{G}(t,s)\mathcal{Q}\mathcal{L}(s)\mathcal{P}\hat{\sigma}_I(s). \tag{6}$$

We note that

$$\begin{aligned}\mathcal{P}\mathcal{L}(t)\mathcal{P}\hat{\sigma}_I(t) &= -\frac{i}{\hbar}\mathcal{P}[\hat{H}_{\mathrm{int}}(t), \mathrm{tr}_B\{\hat{\sigma}_I(t)\} \otimes \hat{\rho}_B] \\ &= -\frac{i}{\hbar}\sum_\alpha [\hat{A}_\alpha(t), \mathrm{tr}_B\{\hat{\sigma}_I(t)\}]\mathrm{tr}\left\{\hat{B}_\alpha(t)\hat{\rho}_B\right\} \otimes \hat{\rho}_B = 0,\end{aligned} \tag{7}$$

if we assume that $\mathrm{tr}\left\{\hat{B}_\alpha(t)\hat{\rho}_B\right\} = 0$ for the steady state. We then obtain the inhomogeneous Nakajima–Zwanzig equation

$$\frac{d}{dt}\mathcal{P}\hat{\sigma}_I(t) = \mathcal{P}\mathcal{L}(t)\mathcal{G}(t,0)\mathcal{Q}\hat{\sigma}_I(0) + \int_0^t ds\mathcal{P}\mathcal{L}(t)\mathcal{G}(t,s)\mathcal{Q}\mathcal{L}(s)\mathcal{P}\hat{\sigma}_I(s). \tag{8}$$

We note that this equation holds even when initial correlations are present, i.e., it may describe processes that are more general than quantum operations. In particular, $\mathcal{Q}\hat{\sigma}_I(0) = (I-\mathcal{P})\hat{\sigma}_I(0) = \hat{\sigma}_I(0) - \mathrm{tr}_B[\hat{\sigma}_I(0)] \otimes \hat{\rho}_B$ is related to the amount of initial correlations between the principal system and its environment. Under the assumption that there are no initial correlations, $\hat{\sigma}(0) = \hat{\rho}(0) \otimes \hat{\rho}_B$, this term drops out. In a real experiment, this may be achieved by measuring the actual state of the system at the initial time. Together with the assumption that the principal system and its environment constitute a closed system, this constitutes the two assumptions for employing the quantum operation formalism. We then obtain the homogeneous Nakajima–Zwanzig equation

$$\frac{d}{dt}\mathcal{P}\hat{\sigma}_I(t) = \int_0^t ds\mathcal{K}(t,s)\mathcal{P}\hat{\sigma}_I(s), \tag{9}$$

with the memory kernel $\mathcal{K}(t,s) = \mathcal{P}\mathcal{L}(t)\mathcal{G}(t,s)\mathcal{Q}\mathcal{L}(s)$. This equation is exact, but is typically as difficult to solve as the full Liouville–von Neumann equation. For practical purposes, it is thus necessary to use a number of assumptions in order to get an equation of motion that is useful.

Born approximation

The first approximation is the Born approximation. Here we assume that the coupling is weak to the environment so that $\mathcal{G}(t,0) \approx \mathbf{I}$. Then we find from the homogenous Nakajima–Zwanzig equation

$$\frac{d}{dt}\mathcal{P}\hat{\sigma}_I(t) = \int_0^t ds\mathcal{P}\mathcal{L}(t)\mathcal{Q}\mathcal{L}(s)\mathcal{P}\hat{\sigma}_I(s) = \int_0^t ds\mathcal{P}\mathcal{L}(t)\mathcal{L}(s)\mathcal{P}\hat{\sigma}_I(s), \tag{10}$$

where we have used that $\mathcal{P}\mathcal{L}(t)\mathcal{P} = 0$. With $\hat{\rho}_I(t) = \mathrm{tr}_B\{\mathcal{P}\hat{\sigma}_I(t)\}$, we obtain after a few steps of algebra

$$\frac{d}{dt}\hat{\rho}_I(t) = -\frac{1}{\hbar^2}\int_0^t ds\ \mathrm{tr}_B\left\{[\hat{H}_{\mathrm{int}}(t),[\hat{H}_{\mathrm{int}}(s),\hat{\rho}_I(s)\otimes\hat{\rho}_B]]\right\}, \tag{11}$$

which is the so-called Born master equation. A change of variables, $\tau = t - s$, i.e., $\int_0^t ds = -\int_t^0 (-d\tau) = \int_0^t d\tau$, yields

$$\frac{d}{dt}\hat{\rho}_I(t) = -\frac{1}{\hbar^2}\int_0^t d\tau \ \mathrm{tr}_B\left\{[\hat{H}_{\mathrm{int}}(t), [\hat{H}_{\mathrm{int}}(t-\tau), \hat{\rho}_I(t-\tau)\otimes\hat{\rho}_B]]\right\}. \tag{12}$$

Using the original decomposition of the interaction Hamiltonian, $\hat{H}_{\mathrm{int}} = \sum_\alpha \hat{A}_\alpha \otimes \hat{B}_\alpha$, the Born master equation may also be written as

$$\begin{aligned}\frac{d}{dt}\hat{\rho}_I(t) &= -\frac{1}{\hbar^2}\sum_{\alpha\beta}\int_0^t d\tau \ \mathrm{tr}_B\left\{[\hat{A}_\alpha(t)\otimes\hat{B}_\alpha(t), [\hat{A}_\beta(t-\tau)\otimes\hat{B}_\beta(t-\tau), \hat{\rho}_I(t-\tau)\otimes\hat{\rho}_B]]\right\} \\ &= -\frac{1}{\hbar^2}\sum_{\alpha\beta}\int_0^t d\tau \left[\hat{A}_\alpha(t), \left[\hat{A}_\beta(t-\tau), \hat{\rho}_I(t-\tau)\right]\right]\mathcal{B}_{\alpha\beta}(\tau) + \mathrm{H.c.}\end{aligned} \tag{13}$$

Here we have introduced the bath correlation functions

$$\mathcal{B}_{\alpha\beta}(t, t-\tau) \equiv \mathrm{tr}_B\left\{\hat{B}_\alpha(t)\hat{B}_\beta(t-\tau)\hat{\rho}_B\right\} = \mathrm{tr}_B\left\{\hat{B}_\alpha(\tau)\hat{B}_\beta(0)\hat{\rho}_B\right\} \equiv \mathcal{B}_{\alpha\beta}(\tau) \tag{14}$$

where we in the second step have taken advantage of $\hat{\rho}_B$ being a steady state. We have also used that $\mathcal{B}^*_{\beta\alpha}(\tau) = \mathcal{B}_{\alpha\beta}(-\tau)$.

Markov approximation

The Born master equation still depends on the full history of the system state. To obtain a Markovian equation it is necessary to also perform the Markov approximation. This approximation is motivated if the self-correlation time τ_B of the environment is much faster than the relaxation time of the principal system, i.e., $|\mathcal{B}_{\alpha\beta}(\tau)| \sim e^{-\tau/\tau_B}$ decays much faster than any change of $\hat{\rho}(t)$. We also assume that the interaction Hamiltonian is weak, i.e., the exchange of energy and particles between the principal system and its environment takes place on a time scale much slower than $\hbar/\tau_B$. Considering only times $t \gg \tau_B$, we may then replace $\hat{\rho}_I(t-\tau)$ with $\hat{\rho}_I(t)$, yielding

$$\frac{d}{dt}\hat{\rho}_I(t) = -\frac{1}{\hbar^2}\sum_{\alpha\beta}\int_0^t d\tau \left[\hat{A}_\alpha(t), \left[\hat{A}_\beta(t-\tau), \hat{\rho}_I(t)\right]\right]\mathcal{B}_{\alpha\beta}(\tau) + \mathrm{H.c.}, \tag{15}$$

which is also known as the *Redfield equation*. Since the correlation function quickly goes to zero for long times, we may extend the upper time limit to infinity, yielding

$$\frac{d}{dt}\hat{\rho}_I(t) = -\frac{1}{\hbar^2}\sum_{\alpha\beta}\int_0^\infty d\tau \left[\hat{A}_\alpha(t), \left[\hat{A}_\beta(t-\tau), \hat{\rho}_I(t)\right]\right] \mathcal{B}_{\alpha\beta}(\tau) + \text{H.c.} \tag{16}$$

This is the so-called Markovian quantum master equation, which is time-local as desired.

Derivation of the Lindblad equation

We note that there are several different ways of deriving the Lindblad equation from the Markovian quantum master equation. Here we use one of the standard derivations where we go over to the frequency domain and perform the rotating wave approximation, also known as the secular approximation. To this end, we use the eigenbasis $|\varepsilon_\alpha\rangle$ to the system Hamiltonian and write

$$A_\alpha(t) = \sum_{a,b} e^{-i(\varepsilon_b-\varepsilon_\alpha)}|\varepsilon_\alpha\rangle\langle\varepsilon_\alpha|A_\alpha|\varepsilon_b\rangle\langle\varepsilon_b| = \sum_\omega A_\alpha(\omega)e^{-i\omega t}, \tag{17}$$

with the Bohr frequencies $\omega \equiv \varepsilon_\beta - \varepsilon_\alpha$. Importantly, we have $A_\alpha(\omega) = A_\alpha^\dagger(-\omega)$. We then get

$$\left[\hat{A}_\alpha(t), \left[\hat{A}_\beta(t-\tau), \hat{\rho}_I(t)\right]\right] = \sum_{\omega\omega'} e^{-i(\omega-\omega')t}e^{i\omega\tau}\left[\hat{A}_\alpha^\dagger(\omega'), \left[\hat{A}_\beta(\omega), \hat{\rho}_I(t)\right]\right]. \tag{18}$$

Introducing the one-sided Fourier transform of the bath correlation function

$$\Gamma_{\alpha\beta}(\omega) \equiv \int_0^\infty d\tau e^{i\omega\tau}\mathcal{B}_{\alpha\beta}(\tau), \tag{19}$$

we obtain

$$\frac{d}{dt}\hat{\rho}_I(t) = -\frac{1}{\hbar^2}\sum_{\alpha\beta}\sum_{\omega\omega'} e^{-i(\omega-\omega')t}\left[\hat{A}_\alpha^\dagger(\omega'), \left[\hat{A}_\beta(\omega), \hat{\rho}_I(t)\right]\right]\Gamma_{\alpha\beta}(\omega) + \text{H.c.} \tag{20}$$

Rotating wave approximation

To obtain the Lindblad equation, we need to perform the rotating wave approximation, where we throw away all terms for which $\omega \neq \omega'$. This approximation is motivated since

terms with $\omega \neq \omega'$ oscillate fast if $t \gg |\omega - \omega'|^{-1}$. Since $t \gg \tau_B$ under the Markov approximation, this is well motivated provided that the Bohr frequencies fulfill

$$\min_{\omega \neq \omega'} |\omega - \omega'| \gg 1/\tau_B. \tag{21}$$

Introducing the Fourier transform of the bath correlation function

$$\gamma_{\alpha\beta}(\omega) \equiv \int_{-\infty}^{\infty} d\tau e^{i\omega\tau} \mathcal{B}_{\alpha\beta}(\tau) = \Gamma_{\alpha\beta}(\omega) + \Gamma^*_{\beta\alpha}(\omega), \tag{22}$$

we obtain, after a few steps of algebra,

$$\begin{aligned} \frac{d}{dt}\hat{\rho}_I(t) &= -\frac{i}{\hbar}[\hat{H}_{LS}, \hat{\rho}_I(t)] \\ &+ \frac{1}{\hbar^2} \sum_{\alpha\beta} \sum_{\omega} \gamma_{\alpha\beta}(\omega) \left(\hat{A}_\beta(\omega) \hat{\rho}_I(t) \hat{A}^\dagger_\alpha(\omega) - \frac{1}{2} \left\{ \hat{A}^\dagger_\alpha(\omega) \hat{A}_\beta(\omega), \hat{\rho}_I(t) \right\} \right). \end{aligned} \tag{23}$$

Here $\hat{H}_{LS} = \sum_\omega \sum_{\alpha\beta} \mathrm{Im}\left[\Gamma_{\alpha\beta}(\omega)\right] A^\dagger_\alpha(\omega) A_\beta(\omega)$ is the Lamb shift Hamiltonian.

To transform back to the Schrödinger equation (note that $[\hat{H}_S, \hat{H}_{LS}] = 0$), we use that $\frac{d}{dt}\hat{\rho}_I(t) = e^{i\hat{H}_S t/\hbar} \left(\frac{d}{dt}\hat{\rho}_S(t) + \frac{i}{\hbar}[\hat{H}_S, \hat{\rho}_S(t)] \right) e^{-i\hat{H}_S t/\hbar}$. We thus get

$$\begin{aligned} \frac{d}{dt}\hat{\rho}_S(t) &= -\frac{i}{\hbar}[\hat{H}_S + \hat{H}_{LS}, \hat{\rho}_S(t)] \\ &+ \frac{1}{\hbar^2} \sum_{\alpha\beta} \sum_{\omega} \gamma_{\alpha\beta}(\omega) \left(\hat{A}_\beta(\omega) \hat{\rho}_S(t) \hat{A}^\dagger_\alpha(\omega) - \frac{1}{2} \left\{ \hat{A}^\dagger_\alpha(\omega) \hat{A}_\beta(\omega), \hat{\rho}_S(t) \right\} \right), \end{aligned} \tag{24}$$

which, after a diagonalization of the (positive) matrix with the matrix elements $\gamma_{\alpha\beta}(\omega)$, yields the Lindblad equation.

Appendix B: Schrieffer–Wolff transformation

We here briefly outline some details related to the Schrieffer–Wolff transformation. The main idea is to apply a unitary transformation to eliminate a perturbation $\hat{V}$ to first order in a Hamiltonian $\hat{H}_S = \hat{H}_0 + \hat{V}$, yielding an effective Hamiltonian

$$\hat{H}_{\text{eff}} = e^{-\hat{S}} \hat{H}_S e^{\hat{S}}. \tag{25}$$

The Baker–Campbell–Hausdorff formula yields

$$\begin{aligned} \hat{H}_{\text{eff}} &= \hat{H} + [\hat{S}, \hat{H}] + \frac{1}{2}[\hat{S}, [\hat{S}, \hat{H}]] + \ldots \\ &= \hat{H}_0 + \hat{V} + [\hat{S}, \hat{H}_0] + [\hat{S}, \hat{V}] + \frac{1}{2}[\hat{S}, [\hat{S}, \hat{H}_0]] + \frac{1}{2}[\hat{S}, [\hat{S}, \hat{V}]] + \ldots \qquad (26) \\ &= \hat{H}_0 + \frac{1}{2}[\hat{S}, \hat{V}] + \mathcal{O}(V^3) \qquad (27) \end{aligned}$$

if the generator $\hat{S}$ of the transformation fulfills the condition [174]

$$\left[\hat{S}, \hat{H}_0\right] = -\hat{V}. \tag{28}$$

In other words, it is possible to eliminate the perturbation $\hat{V}$ to first order, but it will generate new terms, of which only $\frac{1}{2}[\hat{S}, \hat{V}]$ will be important if the perturbation is weak. The main challenge with the Schrieffer–Wolff transformation is to find the generator $\hat{S}$ from the condition above.

Quantum dot system

Here we outline how to obtain the generator and the effective Hamiltonian for the quantum dot system considered in Paper I. For simplicity, we start by considering the quantum dot

system without the leads attached. In that case, we have $\hat{H}_0 = \sum_\gamma \epsilon_\gamma \hat{n}_\gamma + \sum_{\gamma\gamma'} \frac{1}{2} U_{\gamma\gamma'} \hat{n}_\gamma \hat{n}_{\gamma'}$, with single-particle dot levels ϵ_γ, the Coulomb repulsion $U_{\gamma\gamma'}$ between different dots ($\gamma \neq \gamma'$) and $\hat{n}_\gamma = \hat{d}_\gamma^\dagger \hat{d}_\gamma$ the number operator. Furthermore, $\hat{V} = \sum_{\gamma\gamma'} \frac{1}{2} (t_{\gamma\gamma'} \hat{d}_\gamma^\dagger \hat{d}_{\gamma'} + t_{\gamma\gamma'}^* \hat{d}_{\gamma'}^\dagger \hat{d}_\gamma)$ is the tunnel couplings between the dots.

To find the generator $\hat{S}$, we first introduce

$$\hat{A}_{\gamma\gamma'} = \sum_B \left(\frac{1}{\epsilon_\gamma - \epsilon_{\gamma'} + \sum_{\delta' \in B} (U_{\gamma\delta'} - U_{\gamma'\delta'})} \prod_{\delta \in B} \hat{n}_\delta \prod_{\bar{\delta} \in \bar{B}} (1 - \hat{n}_{\bar{\delta}}) \right) \tag{29}$$

for $\gamma \neq \gamma'$. We note that $\hat{A}_{\gamma\gamma'}$ contains number operators acting only on the four dots (of the in total six) which are not γ, γ'. B denotes a configuration out of these four dots and $\bar{B}$ denotes the complementary set. The sum in $\hat{A}_{\gamma\gamma'}$ runs over all 16 possible configurations in B.

Generator of the transformation

The generator may be expressed in terms of $\hat{A}_{\gamma\gamma'}$ as

$$\hat{S} = \sum_{\gamma\gamma'} \frac{1}{2} \hat{A}_{\gamma\gamma'} (t_{\gamma\gamma'} \hat{d}_\gamma^\dagger \hat{d}_{\gamma'} - t_{\gamma\gamma'}^* \hat{d}_{\gamma'}^\dagger \hat{d}_\gamma) \tag{30}$$

We note that $[\hat{A}_{\gamma\gamma'}, \hat{H}_0] = 0$ and that $\hat{A}_{\gamma\gamma'}$ is Hermitian and fulfills $\hat{A}_{\gamma\gamma'} = -\hat{A}_{\gamma'\gamma}$. Furthermore, we note that

$$\begin{aligned}
[\hat{A}_{\gamma\gamma'} \hat{d}_\gamma^\dagger \hat{d}_{\gamma'}, \hat{H}_0] &= \hat{A}_{\gamma\gamma'} [\hat{d}_\gamma^\dagger \hat{d}_{\gamma'}, \hat{H}_0] \\
&= \hat{A}_{\gamma\gamma'} \left[\epsilon_{\gamma'} - \epsilon_\gamma + \sum_{\delta'} (U_{\gamma'\delta'} - U_{\gamma\delta'}) \hat{n}_{\delta'} \right] \hat{d}_\gamma^\dagger \hat{d}_{\gamma'} \\
&= -\sum_B \left[\prod_{\delta \in B} \hat{n}_\delta \prod_{\bar{\delta} \in \bar{B}} (1 - \hat{n}_{\bar{\delta}}) \right] \hat{d}_\gamma^\dagger \hat{d}_{\gamma'} = -\hat{d}_\gamma^\dagger \hat{d}_{\gamma'}
\end{aligned} \tag{31}$$

where the sum on the second line is over all dots except γ and γ'. From this we find

$$\begin{aligned}
[\hat{S}, \hat{H}_0] &= \left[\sum_{\gamma\gamma'} \frac{1}{2} \hat{A}_{\gamma\gamma'} (t_{\gamma\gamma'} \hat{d}^\dagger_\gamma \hat{d}_{\gamma'} - t^*_{\gamma\gamma'} \hat{d}^\dagger_{\gamma'} \hat{d}_\gamma), \hat{H}_0 \right] \\
&= \sum_{\gamma\gamma'} \frac{1}{2} \left(t_{\gamma\gamma'} [\hat{A}_{\gamma\gamma'} \hat{d}^\dagger_\gamma \hat{d}_{\gamma'}, \hat{H}_0] + t^*_{\gamma\gamma'} [\hat{A}_{\gamma'\gamma} \hat{d}^\dagger_{\gamma'} \hat{d}_\gamma, \hat{H}_0] \right) \\
&= -\sum_{\gamma\gamma'} \frac{1}{2} \left(t_{\gamma\gamma'} \hat{d}^\dagger_\gamma \hat{d}_{\gamma'} + t^*_{\gamma\gamma'} \hat{d}^\dagger_{\gamma'} \hat{d}_\gamma \right) = -\hat{V}, \qquad (32)
\end{aligned}$$

i.e., $\hat{S}$ as defined in Eq. (30) is indeed a generator that fulfills the condition in Eq. (28).

Effective Hamiltonian

Having obtained the generator of the transformation, we may now compute the effective Hamiltonian to leading order in $\hat{V}$ from [174]

$$\hat{H}_{\text{eff}} = \hat{H}_0 + \frac{1}{2} [\hat{S}, \hat{V}]. \qquad (33)$$

We evaluate the commutator between $\hat{S}$ and $\hat{V}$ by first considering a single term of $\hat{S}$ and a single term of $\hat{V}$, which are of the form $\hat{A}_{\delta\delta'} (t_{\delta\delta'} \hat{d}^\dagger_\delta \hat{d}_{\delta'} - t^*_{\delta\delta'} \hat{d}^\dagger_{\delta'} \hat{d}_\delta)$ and $t_{\gamma\gamma'} \hat{d}^\dagger_\gamma \hat{d}_{\gamma'} + t^*_{\gamma\gamma'} \hat{d}^\dagger_{\gamma'} \hat{d}_\gamma$, respectively.

Depending on the relation between γ and δ as well as between γ' and δ', we may obtain four different terms in the commutator. Below we consider the four different cases one by one and take advantage of the fact that there can never be more than two electrons in the quantum dot system at the same time.

(i) $\delta = \gamma, \delta' = \gamma'$

In this case, we obtain

$$\frac{1}{2} [\hat{A}_{\gamma\gamma'} (t_{\gamma\gamma'} \hat{d}^\dagger_\gamma \hat{d}_{\gamma'} - t^*_{\gamma\gamma'} \hat{d}^\dagger_{\gamma'} \hat{d}_\gamma), t_{\gamma\gamma'} d^\dagger_\gamma \hat{d}_{\gamma'} + t^*_{\gamma\gamma'} \hat{d}^\dagger_{\gamma'} \hat{d}_\gamma] = |t_{\gamma\gamma'}|^2 \hat{A}_{\gamma\gamma'} (\hat{n}_\gamma - \hat{n}_{\gamma'}). \qquad (34)$$

Consisting of only number operators, this term may be included in the system Hamiltonian by a renormalization of the single-particle energy levels and the interaction strengths

(ii) $\delta = \gamma, \delta' \neq \gamma'$ *and (iii)* $\delta \neq \gamma, \delta' = \gamma'$

Now we obtain the commutator

$$\begin{aligned}
&\frac{1}{2} [\hat{A}_{\gamma\delta'} (t_{\gamma\delta'} \hat{d}^\dagger_\gamma \hat{d}_{\delta'} - t^*_{\gamma\delta'} \hat{d}^\dagger_{\delta'} \hat{d}_\gamma), t_{\gamma\gamma'} \hat{d}^\dagger_\gamma \hat{d}_{\gamma'} + t^*_{\gamma\gamma'} \hat{d}^\dagger_{\gamma'} \hat{d}_\gamma] \\
= \; &-\frac{1}{2} \hat{A}_{\gamma\delta'} [\hat{n}_{\gamma'} \to \hat{n}_\gamma] (t_{\gamma\delta'} t^*_{\gamma\gamma'} \hat{d}^\dagger_{\gamma'} \hat{d}_{\delta'} + t^*_{\gamma\delta'} t_{\gamma\gamma'} \hat{d}^\dagger_{\delta'} \hat{d}_{\gamma'}) \qquad (35)
\end{aligned}$$

with $\hat{A}_{\gamma\delta'}[\hat{n}_{\gamma'} \to \hat{n}_{\gamma}]$ denoting $\hat{A}_{\gamma\delta'}$, with $\hat{n}_{\gamma'}$ replaced by $\hat{n}_{\gamma}$. This part of the effective Hamiltonian describes the tunneling of a single particle, from δ' to γ and then from γ to γ', or vice versa. Similar terms are obtained for $\delta \neq \gamma$, $\delta' = \gamma'$.

These processes are, however, always outcompeted by other processes. For instance, if an electron is in one of the detector dots, it is more likely that it will leave to the connected lead since the dot–lead coupling is much stronger than the tunneling process above. Likewise, if only one entangler dot is occupied, it is more likely that the other will be occupied than the tunneling process above taking place. Lastly, if both entangler dots are occupied the dominant process will be cotunneling, the process to be discussed below.

(iv) $\delta \neq \gamma, \delta' \neq \gamma'$

In this case, we obtain

$$\begin{aligned}
& \frac{1}{2}[\hat{A}_{\delta\delta'}(t_{\delta\delta'}\hat{d}_{\delta}^{\dagger}\hat{d}_{\delta'} - t_{\delta\delta'}^{*}\hat{d}_{\delta'}^{\dagger}\hat{d}_{\delta}), t_{\gamma\gamma'}\hat{d}_{\gamma}^{\dagger}\hat{d}_{\gamma'} + t_{\gamma\gamma'}^{*}\hat{d}_{\gamma'}^{\dagger}\hat{d}_{\gamma}] \\
= \; & \frac{1}{2}\left(\frac{1}{\epsilon_{\delta} + U_{\gamma\delta} - \epsilon_{\delta'} - U_{\gamma\delta'}} - \frac{1}{\epsilon_{\delta} + U_{\gamma'\delta} - \epsilon_{\delta'} - U_{\gamma'\delta'}}\right) \\
\times \; & \Big(t_{\delta\delta'}t_{\gamma\gamma'}\hat{d}_{\delta}^{\dagger}\hat{d}_{\gamma}^{\dagger}\hat{d}_{\gamma'}\hat{d}_{\delta'} + t_{\delta\delta'}^{*}t_{\gamma\gamma'}^{*}\hat{d}_{\delta'}^{\dagger}\hat{d}_{\gamma'}^{\dagger}\hat{d}_{\gamma}\hat{d}_{\delta} \\
& + t_{\delta\delta'}^{*}t_{\gamma\gamma'}\hat{d}_{\delta'}^{\dagger}\hat{d}_{\gamma}^{\dagger}\hat{d}_{\gamma'}\hat{d}_{\delta} + t_{\delta\delta'}t_{\gamma\gamma'}^{*}\hat{d}_{\delta}^{\dagger}\hat{d}_{\gamma'}^{\dagger}\hat{d}_{\gamma}\hat{d}_{\delta'}\Big)
\end{aligned} \tag{36}$$

Importantly, these are the terms describing two-particle cotunneling processes. We note that only terms describing cotunneling between the two entangler dots and two detector dots α, β are of interest for our quantum dot system as the remaining cotunneling processes are outcompeted by single-particle tunneling processes like the ones discussed in cases (ii) and (iii).

We also note that the two-particle tunneling amplitudes $t_{\beta\alpha 21}$ describing the cotunneling processes from the entangler to the detector dots are obtained by summing up all terms in $\hat{S}$ and $\hat{V}$, yielding the important result

$$t_{\beta\alpha 21} = \frac{t_{\beta 1}t_{\alpha 2}}{\Delta E_{\beta\alpha}} - \frac{t_{\alpha 1}t_{\beta 2}}{\Delta E_{\alpha\beta}}. \tag{37}$$

Here we have introduced for brevity

$$\begin{aligned}
1/\Delta E_{\beta\alpha} \; = \; & \frac{1}{2}\left(\frac{1}{\epsilon_1 + U_{12} - \epsilon_{\beta} - U_{2\beta}} - \frac{1}{\epsilon_2 + U_{2\beta} - \epsilon_{\alpha} - U_{\alpha\beta}}\right. \\
& \left. + \frac{1}{\epsilon_2 + U_{12} - \epsilon_{\alpha} - U_{1\alpha}} - \frac{1}{\epsilon_1 + U_{1\alpha} - \epsilon_{\beta} - U_{\alpha\beta}}\right)
\end{aligned} \tag{38}$$

and

$$1/\Delta E_{\alpha\beta} = \frac{1}{2}\left(\frac{1}{\epsilon_2 + U_{12} - \epsilon_\beta - U_{1\beta}} - \frac{1}{\epsilon_1 + U_{1\beta} - \epsilon_\alpha - U_{\alpha\beta}} + \frac{1}{\epsilon_1 + U_{12} - \epsilon_\alpha - U_{2\alpha}} - \frac{1}{\epsilon_2 + U_{2\alpha} - \epsilon_\beta - U_{\alpha\beta}}\right). \tag{39}$$

If we denote the initial, final and intermediate energies, respectively, of the system during a cotunneling event by E_i, E_f and E_m, we find that $1/\Delta E_{\beta\alpha}$, $1/\Delta E_{\alpha\beta}$ may be expressed as $\frac{1}{2}\sum_m(\frac{1}{E_i - E_m} - \frac{1}{E_m - E_f})$, with m running over the two intermediate states. For two-particle resonance, we obtain $E_f \equiv \epsilon_\alpha + \epsilon_\beta + U_{\alpha\beta} = \epsilon_1 + \epsilon_2 + U_{12} \equiv E_i$, thus yielding the simplified expression $\sum_m \frac{1}{E_i - E_m}$, which is consistent with standard second-order perturbation theory [175].

With all the commutators explicitly computed, we may now summarize the expression for the effective Hamiltonian as

$$\hat{H}_{\text{eff}} = \hat{H}_0' + \sum_{\alpha\beta}\left(t_{\beta\alpha 21}\hat{d}_\beta^\dagger \hat{d}_\alpha^\dagger \hat{d}_2 \hat{d}_1 + t_{\beta\alpha 21}^* \hat{d}_1^\dagger \hat{d}_2^\dagger \hat{d}_\alpha \hat{d}_\beta\right). \tag{40}$$

Here $\hat{H}_0'$ denotes the renormalized Hamiltonian $\hat{H}_0$.

When adding the effect of the leads and the dot–lead couplings in $\hat{H}_0$, we note that this will induce additional level-broadening terms in the denominator of $\hat{A}_{\gamma\gamma'}$. These terms are proportional to the dot–lead rates Γ_α and Γ_β. Importantly, the corresponding energies of these rates are small compared to the differences between the single-particle energy levels of the dots, making the level-broadening negligible. In addition, cotunneling processes involving the leads are suppressed as the dot–lead couplings are weak compared to the differences between the single-particle energy levels of the quantum dots. Therefore also these effects may be neglected.

In this thesis, we investigate two different topics related to the physics of nanoscale systems. The first topic concerns quantum correlations, in particular how to generate and detect entangled electrons. The second topic concerns temperature fluctuations, especially how to utilize them for nanoscale calorimetry. The first part of the thesis includes an introduction to the research field and an overview of the main findings of the papers. In the second part, the five papers of the thesis are found in their entirety.

Printed by Media-Tryck, Lund 2019 NORDIC SWAN ECOLABEL 3041 0903

LUND UNIVERSITY

Departement of Physics
Faculty of Science
Lund University
ISBN 978-91-7895-046-1